Applied Catalysis A, General 602 (2020) 117729

Contents lists available at ScienceDirect

Applied Catalysis A, General

journal homepage: www.elsevier.com/locate/apcata

Low temperature synthesis of bio-fuel additives via valorisation of glycerol with benzaldehyde as well as furfural over a novel sustainable catalyst, 12-tungstosilicic acid anchored to ordered cubic nano-porous MCM-48

Anjali Patel*, Dhruvi Pithadia

Polyoxometalates and Catalysis Laboratory, Department of Chemistry, Faculty of Science, The Maharaja Sayajirao University of Baroda. Vadodara, 390002, Gujarat, India

ARTICLE INFO

Keywords:
Bio-fuel additives
Glycerol
Valorisation
Acetalization
Heterogeneous catalyst
High TON

ABSTRACT

The present article demonstrates designing of novel catalyst, 12-tungstosilicic acid (TSA) anchored to ordered nano-porous MCM-48 (nMCM-48); TSA/nMCM-48, characterization and evaluation for synthesis of bio-fuel additives via glycerol valorisation with aromatic aldehydes. The nanopores of support were confirmed by BET and TEM while the interaction between TSA and nMCM-48 was confirmed by decrease in the surface area and pore volume of the catalysts. Assessment of vital reaction parameters (% loading of active species, mole ratio of reactants, catalyst amount, temperature and time) were performed to achieve maximum conversion of glycerol. The catalyst showed noteworthy performance at 30 °C towards conversion (> 85 %) and thermodynamically stable dioxane derivative (> 60 %) with remarkable TON (5945 for benzaldehyde and 7355 for furfural). The catalyst was regenerated and used for successive four catalytic runs with almost same activity. The superiority of novel catalyst is because of its geometry and nano porosity.

1. Introduction

The never-ending demand of energy supplements has geared the sudden urge of replacing non-renewable fossil fuels by renewable ones. As a result of this, the breakthrough comes from the utilization of renewable feedstock, converting into valuable chemicals, bio-additives, biodiesel and biofuels. Hence, from last two decades, there has been an unparalleled revolution in biodiesel industries producing surplus glycerol as by-product [1,2]. Collectively, up to date, these industries are unable to exploit all the glycerol formed from biodiesel manufacturing units. Henceforth in present situation it is important to highlight the economic utilization of spare glycerol by other alternatives. In a view of upgrading glycerol at marketed level, valorisation is the best way that can be carried out via dehydration [3], hydrogenation [4], etherification [5], hydrogenolysis [6] and others [7], especially by reacting three hydroxyl groups through acetalization reaction.

Glyceryl acetals and ketals, potential biodiesel additives/blends [8,9], can be formed by condensation of glycerol with simple aldehydes & ketone using acid catalysts. Acetalization of glycerol with benzaldehyde yields isomeric products, 1,3-dioxolane (5-membered) and 1,3-dioxane (6-membered). They are important precursors to produce green platform chemicals, 1,3-propanediol and 1,3-dihydroxyacetone [10]. They have tremendous contribution as antiknock additives, excellent antioxidants and accelerators for ignition fuel, as fragrances, as food additives, in beverage, lacquer industries and pharmaceuticals [9].

According to the recent forecast data reported by International Energy Agency (Iea), in 2019, biofuel production for transport has extended 6% reaching to 96 Mtoe (161 billion litres) year-on-year and over the next five years 3% annual production growth is expected (Fig. 1) [11]. Thus, from the viewpoint of economic demands for clearing environmental sewage and adverse ecological impact along with traditional disadvantages of homogeneous catalysts, the new generation acetalization reactions via heterogeneous catalytic approach has gained tremendous attention for maximum conversion of glycerol to selective acetals/ketals.

Several solid acid catalysts such as, metal-based catalysts [12,13], montmorillonite [14], activated carbon [15], ion exchange resins [16], mesoporous silicates [17–19] and heteropoly acids [2,20–29] have been applied for the same. Amongst all, the contribution from heteropoly acids (HPAs) based catalysts, especially Keggin type, are found to be excellent from the viewpoint of their compositions and varied structural properties. Keggin type of HPAs are Bronsted acids, having metal-oxygen octahedra with general formula $[XM_{12}O_{40}]^{n-}$, where X is the heteroatom (P or Si) and M is the addenda atom (Mo, W, V etc).

* Corresponding author.
E-mail address: anjali.patel-chem@msubaroda.ac.in (A. Patel).

https://doi.org/10.1016/j.apcata.2020.117729
Received 19 April 2020; Received in revised form 30 June 2020; Accepted 2 July 2020
Available online 04 July 2020
0926-860X/ © 2020 Elsevier B.V. All rights reserved.

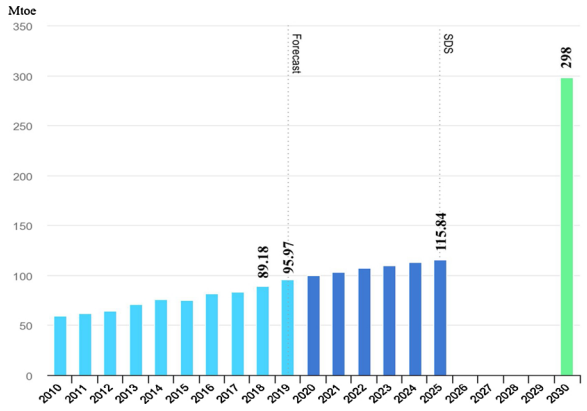

Fig. 1. Global biofuel production 2010-2025 compared to consumption in the Sustainable development Scenario [IEA (2019), Tracking Transport, IEA, Paris https://www.iea.org/reports/tracking-transport-2019].

Sufficient illustrations for acetalization of glycerol using 12-tungstophosphoric acid are available in an art [19,21,22,24,25,28]. Literature survey shows that, even though, TSA is the second most acidic in the HPAs series, only two reports are available, [23,27] for the same. It is also observed that, no reports are available for acetalization of glycerol with furfural, another important industrial reaction, using anchored TSA.

Keeping in mind the importance of TSA as well as glycerol valorisation, we came with a novel heterogeneous catalyst comprising of TSA and nMCM-48. Both, support (nMCM-48) and catalyst (TSA/nMCM-48) were characterized by physicochemical/spectral techniques and evaluated for valorisation of glycerol. Essential reaction parameters (mole ratio of glycerol: benzaldehyde/furfural, catalyst amount, reaction temperature and reaction time) were screened and optimised to obtain maximum conversion and selectivity towards desired product. The catalyst was recovered by simple centrifugation and reused up to 3 cycles. The regenerated catalyst was characterized by acidity, FT-IR and BET surface area measurements to confirm its sustainability. A comparison with the reported catalysts was also carried out and correlated with nano porosity as well as geometry.

2. Experimental

2.1. Materials

All chemicals used were of A.R. grade. 12-tungstosilicic acid, liquor ammonia, TEOS (tetraethylorthosilicate), benzaldehyde, furfural, ethanol and 2-propanol were used as received from Merck. CTAB (Cetyltrimethylammonium bromide) was purchased from Loba chemie and glycerol was acquired from Suvidhinath Laboratories (SULAB; Vadodara, Gujarat).

2.2. Synthesis of the catalyst

The synthesis of TSA anchored to nMCM-48 was carried out in two steps.

Step-I: Synthesis of nMCM-48

The synthesis of nMCM-48 was carried out, by following the reported method with some modification [30]. To 50 g of distilled water, CTAB surfactant (2.4 g, 6.6 mmol) was added and allowed to dissolve completely at 35 °C. To this solution, ethanol (50 mL, 0.87 mmol) and 25 % wt liquor ammonia (~15.4 mL, 0.225 mol) was added and stirred for 15–20 min s, following dropwise addition of TEOS (3.4 g, 16 mmol). The resulting white suspension was aged for 2 h, filtered and washed with distilled water, dried at room temperature and calcined at 550 °C for 6 h. The material obtained was designated as nMCM-48.

Step-II: Synthesis of the TSA anchored to nMCM-48

A series of catalysts containing 10–40 % of TSA anchored to nMCM-48 were synthesized by wet impregnation method. 1 g of nMCM-48 was impregnated with an aqueous solution of TSA (0.1 g/ 10 mL – 0.4 g/ 40 mL of double distilled water) and dried at 100 °C for 10 h. The obtained catalysts were designated as TSA_1/nMCM-48, TSA_2/nMCM-48, TSA_3/nMCM-48, and TSA_4/nMCM-48, respectively.

2.3. Characterization

2.3.1. Determination of total acidity, acidic strength and sites

Acidic properties of synthesized support and catalysts were determined by n-butylamine titration, potentiometric titration method and temperature programmed desorption of ammonia (NH_3-TPD).

2.3.1.1. n-butylamine titration.. For determining total acidity, n-butylamine titration method was performed. 0.25 g of support/catalyst was suspended for 24 h in 25 mL of 0.025 N n-butylamine solution in toluene. The excess base was then titrated against 0.025 N trichloroacetic acid solution in toluene using neutral red indicator to obtain total acidity of the material.

2.3.1.2. Potentiometric titration.. To a suspension of 0.25 g of the support/catalyst in 25 mL of acetonitrile, 0.1 mL of 0.05 N, n-butylamine in acetonitrile was added and stirred at 25 °C for 3 h. Then, the suspension was titrated potentiometrically against 0.05 N solution of n-butylamine in acetonitrile. Variation in electrode potential was measured with a digital pH meter.

2.3.1.3. NH_3-TPD. The temperature-programmed desorption (TPD) of NH_3 was measured on BELCAT-II (Japan) instrument. 0.05 g of dry material was loaded and allowed to pre-treat at 300 °C for 1 h in presence of pure He gas (99.9 %, 30 mL per min). Ammonia (10 % NH_3 in He gas) was adsorbed on the surface of material for 1 h and then the physisorbed ammonia was removed by flushing with pure He gas. Finally, the temperature programmed was performed from 100 to 600 °C with a ramp rate of 10 °C/min. Desorbed NH_3 was monitored by using TCD (thermal conductivity detector) of the apparatus.

2.3.2. Physicochemical techniques

Elemental analysis was carried out using JSM-7100 F EDX-SEM analyser. Thermogravimetric analysis (TGA) of synthesized support/catalyst was performed using a Mettler Toledo Star SW 7.01 instrument under nitrogen atmosphere in the temperature range of 50–800 °C with flow rate of 2 mL min^{-1} and with heating rate of 10 °C min^{-1}. For FT-IR spectra, the samples were compelled with dry KBr into discs and recorded in the range of wave numbers $4000 - 400\ cm^{-1}$ by using Shimadzu instrument (IRAffinity-1S). The BET surface area measurements were performed in a Micromeritics ASAP 2010 volumetric static adsorption instrument with N_2 adsorption at 77 K. The pore size distributions were calculated by BJH adsorption-desorption method. Scanning electron microscope (SEM) images were recorded on JSM-7100 F scanning electron microscope. Transmission electron microscopy (TEM) was performed on JEOL TEM instrument (model-JEM 2100) by applying acceleration voltage of 200 kV using carbon coated 200 mesh Cu grid. The samples were dispersed by ultrasonication and coated on grid, leaving overnight for drying in air. The X-ray powder diffraction (XRD) patterns of the support and the catalyst were measured using a D8 FOCUS X-ray Diffractometer from Bruker in the 2θ range of $0 - 80^0$ using CuK_α radiation ($\lambda = 1.54056$ Å). ^{29}Si MAS NMR was recorded using JOEL ECX 400 MHz High resolution multinuclear FT-NMR spectrometer for solids.

2.4. Catalytic evaluation

The acetalization of glycerol was carried out in 50 mL 2 neck glass reactor under nitrogen atmosphere. The reactor was charged with

glycerol (0.01 mol), benzaldehyde (0.01 mol) / furfural (0.01 mol) and catalyst. The reaction mixture was stirred vigorously at 30 °C under N_2 atmosphere, followed by diluting the contents with 2-propanol and analysed using Shimadzu 2014 GC equipped with RTX-5 capillary column (internal diameter: 0.25 mm, length: 30 m). The products were identified by GC–MS (Gas chromatography-mass spectrometry- Thermo scientific DSQ-II; Capillary column- Thermo TR-MS).

Turnover number (TON) refers to the moles of product formed per mole of catalyst. It was calculated by using the following formula:

$$\text{TON} = \frac{\text{number of moles of product}}{\text{number of moles of catalyst}}$$

Number of moles of catalyst was calculated by taking the amount of TSA incorporated.

2.5. Leaching test

Escape of any active species from the support makes the catalyst unappealing and hence it is mandatory to analyse leaching of TSA from nMCM-48. Heteropoly acids can be determined qualitatively via heteropoly blue colour, when treated with mild reducing agent like ascorbic acid. To check the leaching of any TSA from the support, suspension of 1 g of catalyst with 10 mL conductivity water was allowed to reflux for 24 h. The resulting supernatant solution was treated with 10 % ascorbic acid solution and the absence of blue colour indicates no leaching of TSA. The similar test was performed for the residue obtained after reaction completion and absence of blue colour indicates no leaching of TSA.

3. Results and discussion

3.1. Catalyst characterization

The effective TSA loading in all catalysts was calculated by the following equation.

$$\text{Loading amount}(\%) = \frac{\text{Weight of TSA}}{(\text{Weight of TSA}) + (\text{Weight of nMCM}-48)} \times 100$$

According to the given formula, for the series of catalysts, TSA_1/nMCM-48, TSA_2/nMCM-48, TSA_3/nMCM-48 and TSA_4/nMCM-48, the subscript 1, 2, 3 and 4 indicates loading of TSA, which is 9, 16.66, 23.07 and 28.5 wt%, respectively.

The values of elemental analysis by EDX (Table 1) for all catalysts were in good agreement with theoretical calculated value of tungsten (W) except for TSA_4/nMCM-48 indicating effective loading of TSA. However, it should be noted that the variation in case TSA_4/nMCM-48, may be due to insufficient loading. The EDX elemental mapping of TSA_3/nMCM-48 is shown in Fig. 2 while others are included in supplementary material (Figure S1).

It is seen from Table 2 that as the amount of TSA loading increases, total acidity also increases. This may be due to enhancement in the concentration of Bronsted acidity of TSA inside nMCM-48, which is in good agreement with results of elemental analysis. However, on increasing the amount of TSA from 30 % to 40 %, no significant change in total acidity was observed. The acidic strength and total number of acidic sites of synthesized catalysts including support were determined by potentiometric titration. The acid strength of surface sites can be assigned according to the following scale: Ei > 100 mV (very strong sites), 0 < Ei < 100 mV (strong sites), −100 < Ei < 0 mV (weak sites) and Ei < −100 mV (very weak sites) [28]. The plots of the electrode potential as a function of meq. n-butylamine per g of the material are shown in supplementary figure S2. From the data presented in Table 2, it is well distinct that as the amount of TSA loading on nMCM-48 increases from 10 to 30 %, the acidic strength increases significantly, while negligible change observed from 30 to 40 %. The increase in number of very strong and strong acidic sites is directly related to the amount of TSA which is attributed to enhanced Bronsted acid sites.

Noted that only a slight increase in the acidic strength as well as the total number of acidic sites was observed from 30% to 40% loading of TSA, which is in good agreement with the value of total acidity. This may be due to the blocking of the sites as well as insufficient impregnation, which was also observed in the EDX analysis. Hence TSA_3/nMCM-48 was considered for detailed characterization and re-coded as TSA/nMCM-48.

To confirm the types of acidic sites, the support and catalyst were further characterized by NH_3-TPD analysis (Fig. 3). The profile of support and the catalyst exhibits combined desorption peak for weak as well as moderate acid sites. Desorbed amount of ammonia can be directly related to the amount of the acid sites on the sample and also the strength of the acid sites can be determined by desorption temperature. NH_3 desorbed below 200 °C is due to weak acidic site. Around 250–400 °C, desorption occurs due to medium/moderate acidic sites and above 500 °C is due to strong acid site. It is well distinct from the Fig. 3 that for nMCM-48 negligible amount of ammonia was desorbed indicating presence of few weak and moderate acidic sites. After introduction of TSA, elevation of peak area from 100 to 300 °C was observed corresponding to the increase in weak and moderate Bronsted acid sites [31]. Thus, the overall enhancement in the acidic sites of material was obtained due to incorporation of TSA inside the pores of nMCM-48, which is in good agreement with reported one [23].

TGA for nMCM-48 and TSA/nMCM-48 are shown in supplementary

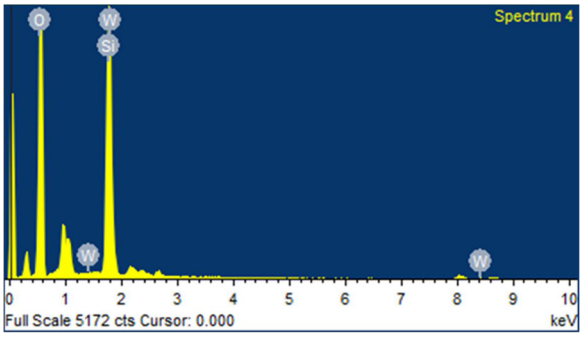

Fig. 2. EDX elemental mapping of TSA_3/nMCM-48.

Table 1
Elemental analysis of catalysts.

Material	Si (wt%)	O (wt%)	W (wt%)	
			By EDX	Theoretical
TSA_1/nMCM-48	41.34	52.19	6.48	6.96
TSA_2/nMCM-48	35.96	51.46	12.58	12.7
TSA_3/nMCM-48	23.73	58.93	17.34	17.7
TSA_4/nMCM-48	30.59	49.28	20.13	21.8

Table 2
Acidity measurements of support and catalysts.

Material	Potentiometric titration				n-butylamine titration
	Acidic strength (mV)	Types of acidic sites (meq g^{-1})		Total No. of acidic sites	Total acidity (mmol g^{-1})
		Very strong	Strong	(mmol g^{-1})	
nMCM-48	168	0.1	2.3	0.48	1.04
TSA_1/nMCM-48	646	0.3	2.3	0.52	1.28
TSA_2/nMCM-48	676	0.6	2.7	0.66	1.32
TSA_3/nMCM-48	700	1.4	3.5	0.98	1.44
TSA_4/nMCM-48	706	1.3	3.6	1.04	1.46

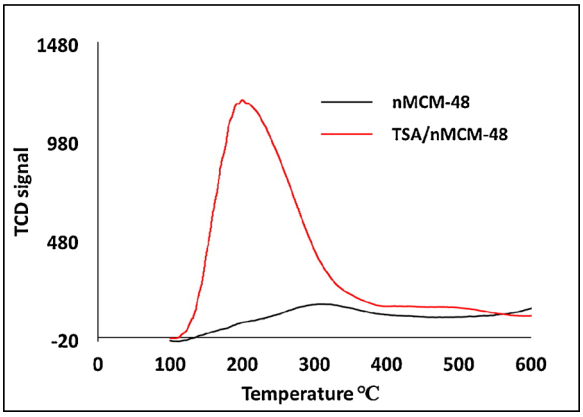

Fig. 3. NH_3-TPD profile of nMCM-48 and TSA/nMCM-48..

figure S3. From the plots it is seen that the weight loss occurs mainly in two stages. For nMCM-48, the initial weight loss of 8.9 % up to 110 °C may be due to the desorption of physically absorbed water molecules. Final weight loss of < 1 % up to 400 °C is attributed to the condensation of silanol groups present in the nMCM-48 [32]. After that, no weight loss was observed, which indicates the stability up to 550 °C. While TSA/nMCM-48, shows initial weight loss of 8.1 % up to 115 °C corresponding to adsorbed water. The second weight loss of 0.67 % up to 200 °C can be attributed to crystalline water molecules present in Keggin unit [23]. After that, no gradual weight loss up to 550 °C, shows the stability of the catalyst.

FT-IR spectrum (Fig. 4) of pure nMCM-48 shows a broad band around 1100 cm^{-1} and 1250 cm^{-1} which corresponds to Si-O-Si asymmetric stretching. It also shows bands at 578 and 462 cm^{-1}, which can be attributed to the symmetric stretching of Si-O-Si and bending vibration of Si-O respectively. Symmetric stretching vibration of Si-O-Si and bending vibration of Si-O are depicted by the bands around 578 and 462 cm^{-1} respectively. The broad band at 3448 cm^{-1} is due to the absorption of hydroxyl group from presence of large amount of H_2O. The obtained bands are in good agreement with the reported one [33]. FT-IR of TSA/nMCM-48 shows two of the characteristic bands for the Keggin unit TSA at 972 and 925 cm^{-1} corresponding to asymmetric

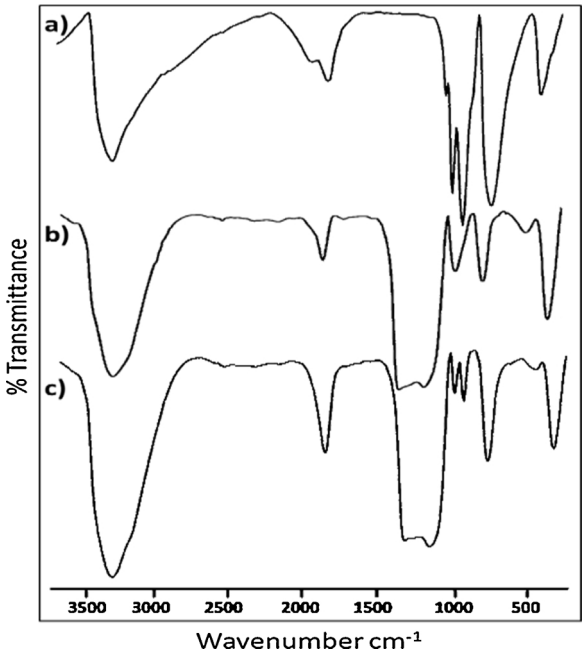

Fig. 4. FT-IR spectra of **a)** TSA **b)** nMCM-48 **c)** TSA/nMCM-48.

Table 3
Textural properties of support and catalysts.

Material	Surface area (m^2/g)	Pore volume (cm^3/g)	Pore diameter (Å)
nMCM-48	1307	0.63	20.8
TSA_1/nMCM-48	712	0.24	20.1
TSA_2/nMCM-48	637	0.25	19.2
TSA_3/nMCM-48	588	0.21	18.3
TSA_4/nMCM-48	333	0.23	17.8

*TSA_3/nMCM-48 = TSA/nMCM-48.

vibrations of W-O_d (terminal oxygen linked to a lone tungsten atom) and (Si-O_a) respectively. Presence of these fingerprint bands directs that the primary structure of TSA is completely unchanged even after impregnation on the support.

The nonappearance of vibrational bands around 880 cm^{-1}(V_{as}(W-O_b-W)) and 785 cm^{-1} (V_{as} (W-O_c-W)) of TSA may be due to superimposition with the bands of nMCM-48 [34]. Further, FT-IR spectra of TSA/nMCM-48 also shows an additional peak at 1635 cm^{-1}, may be due to the bending vibration of bridging hydroxyl groups, resulting from the hydrogen bond between terminal oxygen of TSA and hydrogen of silanol groups of nMCM-48.

Textural properties of support as well as catalysts are shown in Table 3. Relatively small pore diameter of nMCM-48 gives the first indication that the support is nano-porous in nature with high specific surface area. Significant decrease in both, surface area as well as pore volume clearly indicate the incorporation of TSA inside the porous network of nMCM-48. It is very interesting to note down a decrease in surface area and increase in the pore value for TSA_4/nMCM-48, indicating blocking of the sites because of the multilayer adsorption of TSA. Looking at the values of pore volume and pore diameter, once again, TSA_3/nMCM-48 was selected for the further study.

The N_2 adsorption-desorption isotherms of nMCM-48 and TSA/nMCM-48 (Fig. 5) shows typical nature of type IV(b), conforming the formation of mesoporous structure. According to the IUPAC technical report, capillary condensation for the pores having smaller width are completely reversible with the absence of a hysteresis loop. In the present case, the obtained completely reversible isotherms are without hysteresis loop indicating the smaller width and confirming the nanoporous structure. The observation is in good agreement with the reported one [35]. The uniformity in the size of nanopores is well distinct from the sharpness of the step and position of the inflection point which is related to the diameter of pores (20.8 Å). For nMCM-48, adsorption in the mesopores is well distinct in the range of relative pressure between 0.2 – 0.3 which disappears for TSA/nMCM-48 indicating the effective filling of mesopores by TSA [36].

SEM images (supplementary figure S4) shows spherical morphology with a uniform particle size of nMCM-48. SEM micrograph of TSA/nMCM-48 indicates the homogeneous distribution of spheres and there is no noticeable change observed in the morphology even after the introduction of TSA species, indicating its fine dispersion into three dimensional pores, further confirmed by XRD.

TEM images (Fig. 6) of nMCM-48 and TSA/nMCM-48 were recorded at various magnifications. Fig. 6a & 6b of nMCM-48 shows well-ordered pore networks with uniform particle diameter, confirming the nanoporous structure, which is in good agreement with the BET surface area analysis. Opaque spheres were observed in TSA/nMCM-48 (Fig. 6c & 6d), where the maximum pores are uniformly filled with TSA. This is further confirmed by XRD.

The Low angle powder XRD analysis (Fig. 7a) shows a typical pattern of nMCM-48 exhibiting characteristic diffraction peaks at 3.0° and 3.36° 2θ corresponding to the plane 211 and 220, respectively. In the range of 4 – 5° 2θ, numerous peaks correspond to the reflection planes 400, 321 and 420 of MCM-48 having Ia3d cubic symmetry [37]. The XRD pattern of TSA/nMCM-48 depicts the decrease in intensity of

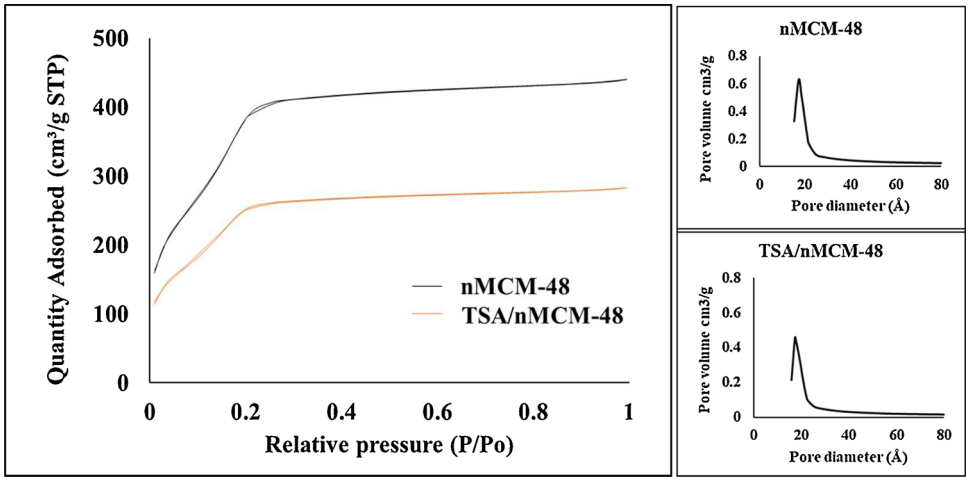

Fig. 5. Nitrogen (N_2) adsorption-desorption isotherms.

characteristic peak with slight broadening which is in good agreement with the reported one [38]. Wide angle XRD pattern (Fig. 7b) of anchored MCM-48 shows the absence of characteristic peaks of the crystalline phase of TSA, signifying very fine dispersion of it into the pores of nMCM-48 [39]. Collectively, it can be inferred from the XRD results, that the structure of nMCM-48 remains intact even after impregnation of TSA.

To identify the interactions between of nMCM-48 and TSA, solid state ^{29}Si MAS-NMR was performed. Typical broad peak for nMCM-48 was observed between -95 and -120 ppm corresponding to the three main components Q^2, Q^3 and Q^4 (Fig. 8). The notation Q^x describes the number of x siloxane linkages to a silicon atom. For instance, the Q^2 signal corresponds to the disilanol linkage Si− $(O-Si)_2$ $(-O-X)_2$, where X is H or TSA. Similarly, resonating peaks for $(O-X)-Si-(O-Si)_3$ and Si− $(O-Si)_4$ corresponds to Q^3 and Q^4 respectively. The chemical shift values for all components are mentioned in Table 4. The observed values of chemical shifts for nMCM-48 are in good agreement with the reported literature [40]. The observed minor downfield shift in the value of chemical shift for Q^2, Q^3 and Q^4 as well as broadening in the spectrum of TSA/nMCM-48 as compared to n MCM-48 may be due to the presence of TSA. Also, a slight change in the intensities of Q^2 and Q^3 peaks were observed, indicating the strong bonding of TSA to proton of silanol groups of nMCM-48. Evidently, the signal for TSA appears in the range of -81 to -90 ppm, which is depicted in the spectrum at -87.97 ppm, showcasing the unchanged Keggin structure of TSA. [41].

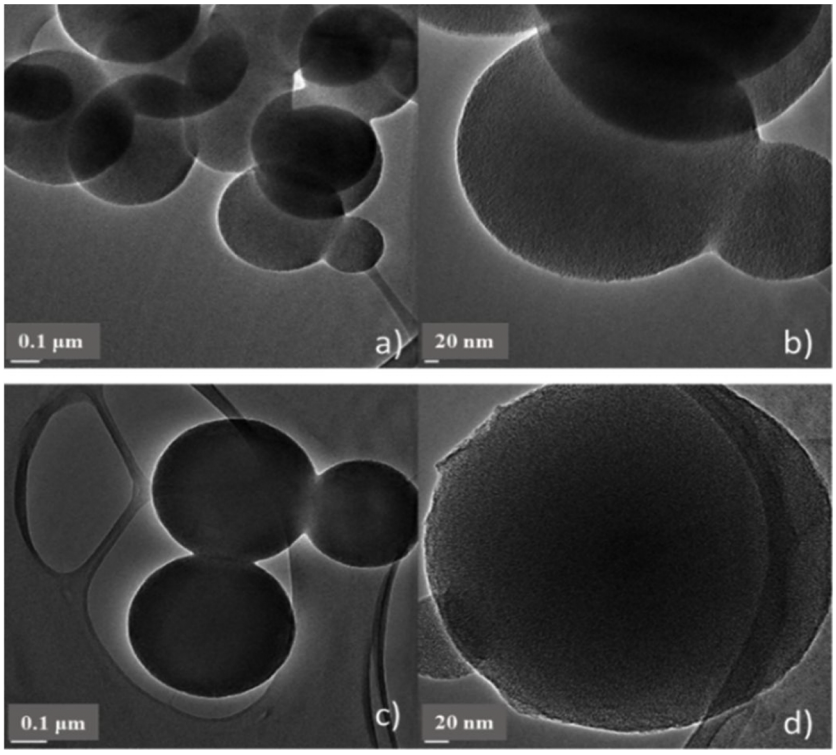

Fig. 6. TEM images of **a, b)** nMCM-48 **c, d)** TSA/nMCM-48.

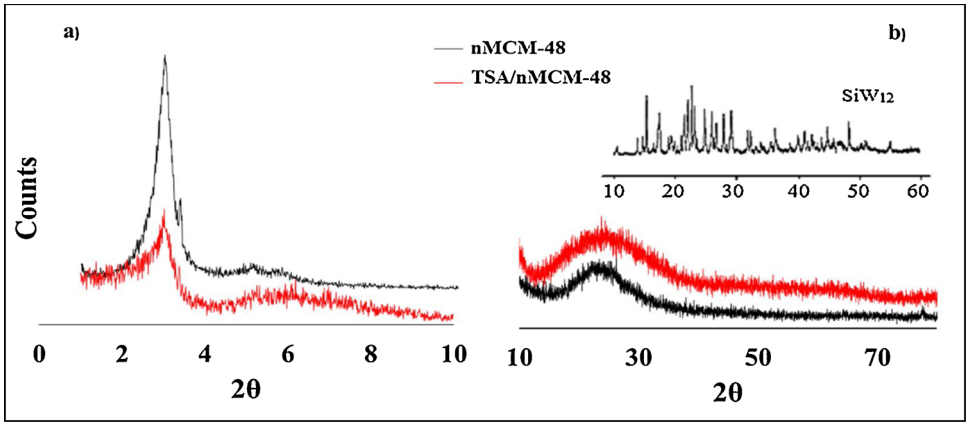

Fig. 7. a) Low angle Powder XRD patterns b) Wide angle Powder XRD patterns.

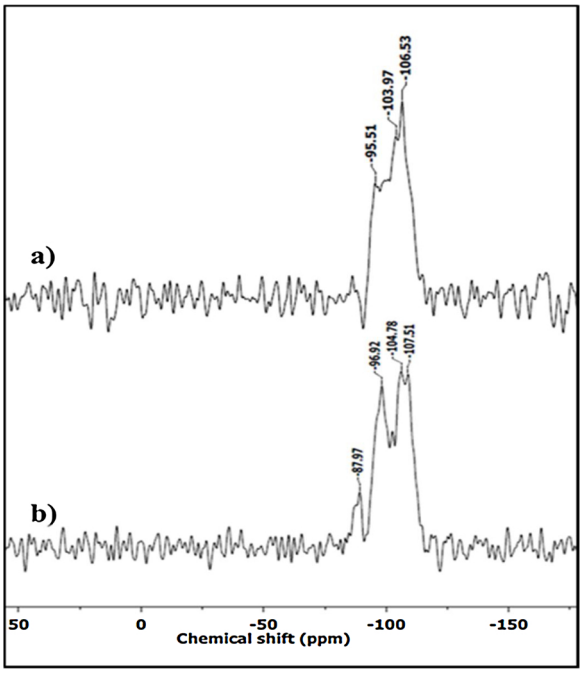

Fig. 8. ^{29}Si MAS NMR spectra of a) nMCM-48 b) TSA/nMCM-48.

Table 4
^{29}Si chemical shifts of nMCM-48 and TSA/nMCM-48.

Material	Si nuclei ppm (TSA)	Q^2 ppm	Q^3 ppm	Q^4 ppm
nMCM-48	–	−95.51	−103.97	−106.53
TSA/nMCM-48	−87.97	−96.92	−104.78	−107.51

Thus, acidity measurements show that the total acidity as well as acidic strength increases after the introduction of TSA into nMCM-48. BET and FT-IR studies indicates the inclusion of undegraded TSA into the nanopores of nMCM-48 via hydrogen bonding between terminal oxygen and hydrogen of silanol groups of nMCM-48. TEM, XRD and ^{29}Si MAS NMR confirm the meso structure with nanopores, fine dispersion of TSA inside nMCM-48 and strong interaction of silanol groups to TSA inside pores of nMCM-48, respectively.

3.2. Catalytic evaluation

3.2.1. Acetalization of glycerol with benzaldehyde

Glycerol acetalization with benzaldehyde yields two cyclic products, 1,3-dioxolane (5-membered) and 1,3 dioxane (6- membered) (Scheme 1), amongst which 1,3-dioxane is thermodynamically favoured. To study the effect of % loading of TSA, reactions were carried using 10, 20, 30 and 40 % TSA loaded nMCM-48. From Fig. 9a, it is seen that as the % of TSA increases, % conversion also increases from 67 to 98 %. However, the trend does not show a significant change in conversion from 30 to 40 % loading. Hence, considering the equivalent effect in terms of acidity measurements as well as % conversion, the catalyst with 30 % TSA loading, TSA/nMCM-48 was selected for the detailed study.

The effect of mole ratio of glycerol to benzaldehyde was studied by varying from 1:1 to 1:2 (Fig. 9b). 98 % glycerol conversion with 65 % and 35 % selectivity of 1,3-dioxane and 1,3-dioxolane respectively, was obtained with 1:1 mole ratio. By increasing the ratio to 1: 1.5 and 1: 2, there was no significant change in the conversion of glycerol and selectivity. As a result, 1:1 mole ratio was considered optimum for further catalytic evaluation. The initial feasibility of the catalyst indicates the selective formation of thermodynamically stable 1,3-dioxane (six membered acetal) and hence further parameters were optimised by focusing the selectivity for the same.

The effect of catalyst amount was studied by screening the range 10–50 mg (Fig. 9c). Initially, from 10 mg to 20 mg marginal increase in the % conversion was observed. Further increase in catalyst amount did not show any significant effect in terms of conversion as well as selectivity. The observed behaviour is may be due to the blocking of sites/saturation of the number of active sites available vs. reactant amount. Hence, 20 mg was considered to be optimum amount.

The most important parameter which governs the equilibrium of reaction is the reaction temperature. It is well-known that acetalization reaction has low equilibrium constant and is exothermic in nature [16]. Screening of reaction temperature ranging from 20 to 40 °C over TSA/MCM-48 was carried out. As depicted by the plot in Fig. 9d, there was no major rise in the % conversion and selectivity of desired thermodynamically stable product, hence, an easily accessible temperature, 30 °C was optimized for the said conversion.

From Fig. 9e it is seen that % conversion increased from 30 to 40 min, with no change in the selectivity of products. Despite increasing the reaction time from 40 to 60 min, very negligible rise of 2 % in glycerol conversion was observed which indicates the establishment of equilibrium beyond 40 min. Thus, 40 min was considered to be optimum time for reaction.

The optimised reaction conditions for the maximum conversion of glycerol (95 %) and selectivity of dioxane (65 %) are: glycerol: benzaldehyde w/w ratio 1: 1; catalyst amount 20 mg; active amount of TSA 4.6 mg; substrate: catalyst ratio (mol: mol) 6257:1; reaction temperature 30 °C; reaction time 40 min with TON 5945.

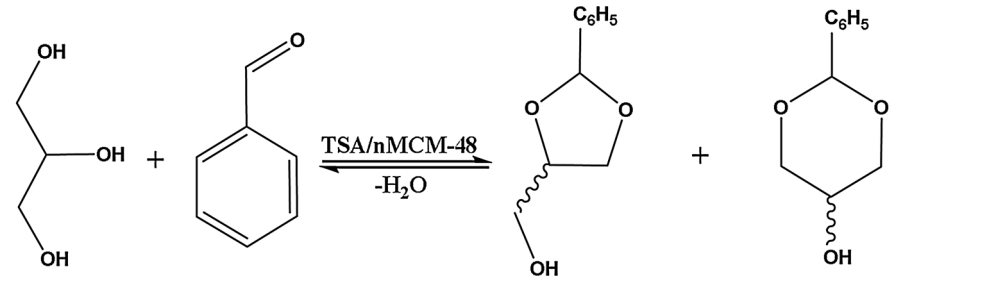

Glycerol Benzaldehyde (2-phenyl-1,3-dioxolan-4-yl) methanol (1,3-dioxolane) 2-phenyl-1,3-dioxan-5-ol (1,3-dioxane)

Scheme 1. Acetalization of glycerol with benzaldehyde.

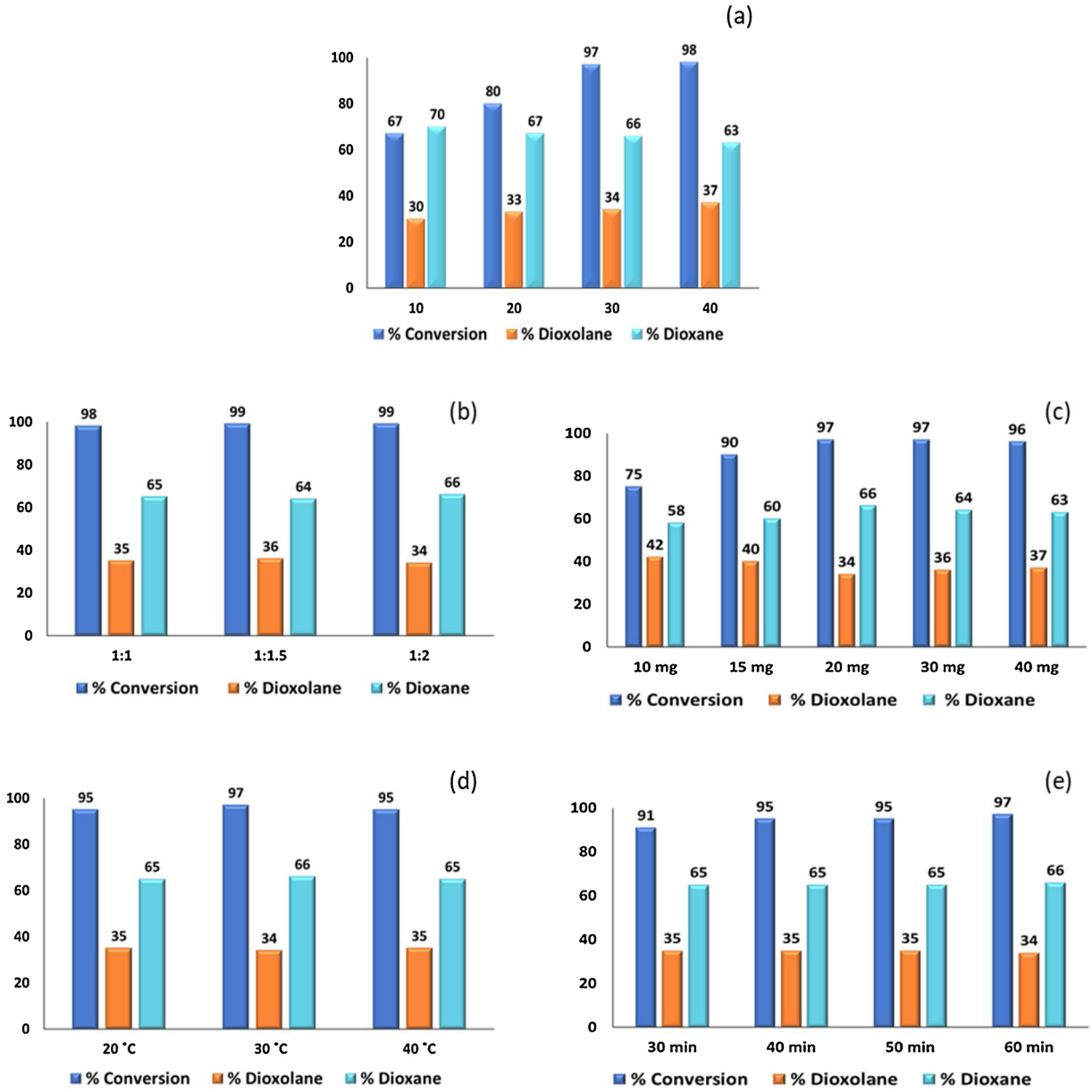

Fig. 9. (a) Effect of % loading TSA. Mole ratio: 1:1; Catalyst amount: 50 mg; Temperature: 30 °C; Time: 60 min; (b)Effect of mole ratio. Catalyst amount: 50 mg; Temperature: 30 °C; Time: 60 min; (c) Effect of catalyst amount. Mole ratio: 1:1; Temperature: 30 °C; Time: 60 min; (d) Effect of reaction temperature. Mole ratio: 1:1; Catalyst amount: 20 mg; Time: 60 min; (e) Effect of reaction time. Mole ratio: 1:1; Catalyst amount: 20 mg; Temperature: 30 °C.

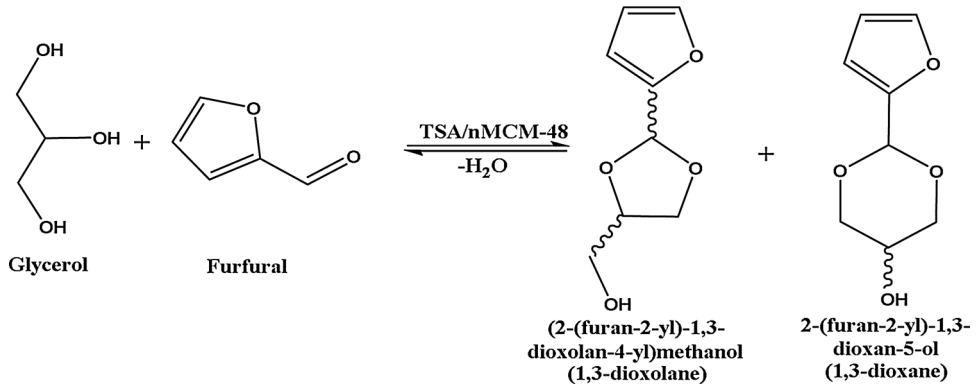

Scheme 2. Acetalization of glycerol with furfural.

3.2.2. Acetalization of glycerol with furfural

In order to evaluate efficiency and versatility of catalyst, reaction with heterocyclic aldehyde- furfural (Scheme 2) was also studied by varying the same parameters as mentioned for benzaldehyde and the obtained results are presented in Fig. 10.

The optimum conditions for glycerol acetalization with furfural for maximum conversion (89 %) and selectivity (69 %) towards dioxane are: glycerol: furfural w/w ratio 1:1; catalyst amount 15 mg; active amount of TSA 3.5 mg; substrate: catalyst ratio (mol: mol) 8223:1; reaction temperature 30 °C; time 40 min with TON 7355. Requirement of low catalyst amount (15 mg) can be due to the presence of active furan ring in furfural.

3.3. Kinetics: determination of activation energy

For determining the activation energy, both the reactions were subjected to different time intervals at 20, 30 and 40 °C, keeping the other parameters same as in optimised reaction condition and the obtained rate constants (k) are presented in Table 5. Using these data, the value of activation energy (Ea) was calculated form the slope of graph (ln k vs 1/T, K^{-1}) (Fig. 11) by Arrhenius equation.

It is reported in the literature that for the reactions following diffusion regime, the activation energy is as low as 10 − 15 kJ/mol, while for the reactions governed by truly chemical step, the activation energy is greater than 25 kJ/mol [42]. Here, in both the cases, the activation energy is exceeding 25 kJ/mole, which clearly suggests that the reactions are governed truly by chemical step.

It is interesting to note that the activation energy for the acetalization of glycerol with furfural (36 kJ/mol) is lower as compared to that with benzaldehyde (43 kJ/mol). The values of activation energy clearly indicate that the lower activation energy for furfural can be attributed to the presence of active furan ring which requires comparatively less prompt effect for the reaction to proceed in forward direction.

3.4. Control experiments

The control experiments for acetalization of glycerol with benzaldehyde and furfural were performed in their respective optimised reaction conditions. From the results demonstrated in Table 6, it was observed that the support alone is not active for the desired transformations and almost similar activity was seen for TSA and TSA/nMCM-48. This confirms that the reactivity is only due to the active keggin unit, TSA, present inside the porous framework and it can be attributed to successful anchoring of TSA. Hence, we have fruitfully synthesized a catalyst which is truly heterogeneous in nature.

3.5. Recycling studies

To reduce the overall cost of production, feasibility of heterogeneous catalyst can be determined by its recycling. For recycling studies, the catalyst was collected by centrifugation after reaction completion and simply treated with methanol to remove the substrate and product remains from the surface, followed by water wash. The catalyst was dried at 100 °C and reused for the next catalytic run. The result (Fig. 12) shows that the catalyst is stable without any leaching of TSA during the reaction.

3.6. Characterization of regenerated catalyst

In order to check sustainability, the regenerated catalyst was characterized by n-butyl amine titration, BET surface area and FT-IR analysis. Total acidity obtained by n-butyl amine titration method for regenerated catalyst (1.43 mmol g^{-1}) was in good agreement with that of fresh one (1.44 mmol g^{-1}), indicating the unaltered acidic property of catalyst. The N_2 adsorption- desorption isotherms (Supplementary figure S5a) of fresh and regenerated catalyst shows identical curves with no change in BET surface area, 588 & 580 m^2/g respectively. This also suggests that there is no alteration in the structure of catalyst after reaction. In FT-IR analysis (Supplementary figure S5b), presence of all the characteristic bands in spectra with no shifting of values, confirms that there is no leaching and change in the structure of keggin unit. However, a little bit of decrease in intensity of FT-IR bands was observed due to the regeneration process.

3.7. Effect of nature of substrates

To study the relative reactivity of benzaldehyde and furfural in presence of synthesized catalyst, reactions were carried in same experimental conditions and obtained results are presented in Table 7. It is interesting to note from the results that simple aromatic aldehyde, benzaldehyde requires more catalyst amount than heterocyclic

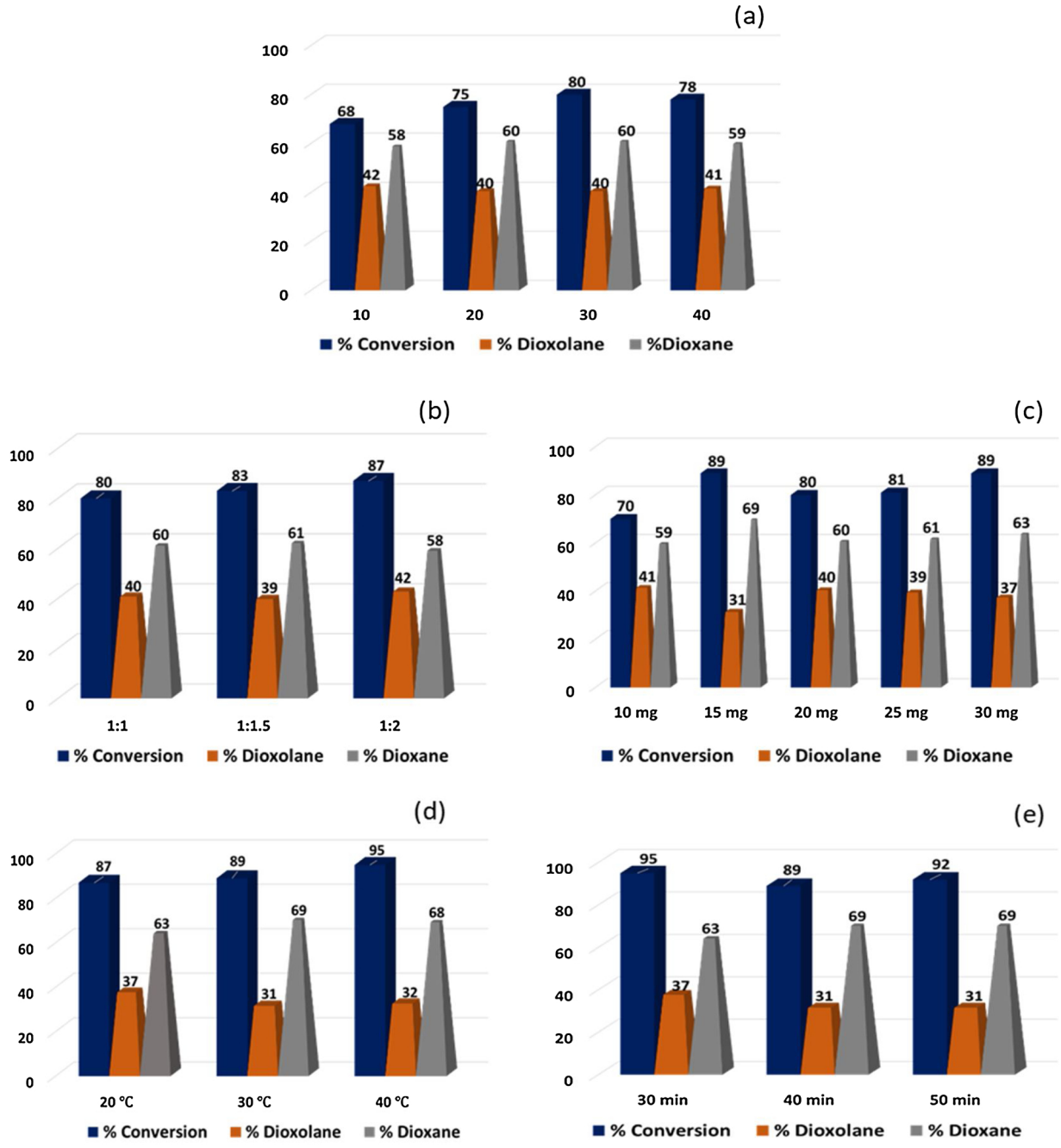

Fig. 10. (a) Effect of % loading TSA. Catalyst amount: 20 mg; Temperature: 30 °C; Time: 40 min; (b) Effect of mole ratio. Catalyst amount: 20 mg; Temperature: 30 °C; Time: 40 min; (c) Effect of catalyst amount. Mole ratio: 1:1; Temperature: 30 °C; Time: 40 min; (d) Effect of reaction temperature. Mole ratio: 1:1; Catalyst amount: 15 mg; Time: 40 min (e) Effect of reaction time. Mole ratio: 1:1; Catalyst amount: 15 mg; Temperature: 30 °C.

Table 5
Kinetic parameter (k min^{-1}) at different temperatures and activation energy (Ea).

Temperature (K)	Glycerol with Benzaldehyde		Glycerol with Furfural	
	Rate constant k (min^{-1})	Activation energy Ea (kJ/mol)	Rate constant k (min^{-1})	Activation energy Ea (kJ/mol)
293	1.512×10^{-2}	43	1.85×10^{-2}	36
303	4.032×10^{-2}		2.55×10^{-2}	
313	4.680×10^{-2}		4.73×10^{-2}	

aldehyde, furfural for maximum conversion and selectivity. This can be attributed to the presence of active furan ring in furfural which proceeds to form acetals more dominantly than benzaldehyde. This observation is in good agreement with the obtained values of activation energy, where formation of acetals of furfural shows comparatively lower activation energy than that for acetals of benzaldehyde. Also, in case of furfural increase in catalyst amount (20 mg) decreases the conversion (80 %) as well as selectivity (60 %) (Fig. 10c) which may be due to the mass density increase and less available surface sites for catalytic reaction. Hence, it can be inferred that heterocyclic aldehydes

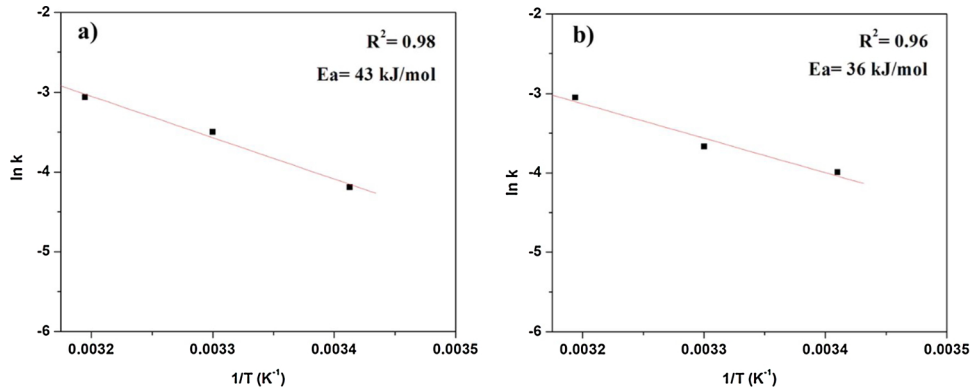

Fig. 11. Plot for determination of activation energy (ln k vs 1/T, K^{-1}) a) Glycerol acetalization with benzaldehyde b) Glycerol acetalization with furfural.

Table 6
Control experiments.

Catalysts	Glycerol with Benzaldehyde[a]		Glycerol with Furfural[b]	
	% Conversion	% selectivity of Dioxane	% Conversion	% selectivity of Dioxane
nMCM-48	1.5	49	3.1	52
TSA	97	62	91	58
TSA/nMCM-48	95	65	89	69

Reaction conditions: Mole ratio 1:1, reaction temperature, reaction time: 40 min, amount of nMCM-48 [a]15.4 mg, [b]11.5 mg, amount of TSA [a]4.6 mg, [b]3.5 mg, catalyst amount [a]20 mg, [b] 15 mg.

Table 7
Effect of nature of substrates.

Substrate	% Conversion	% selectivity of Dioxane	TON
Benzaldehyde	88	60	7272
Furfural	89	69	7355

Reaction conditions: mole ratio 1:1, reaction temperature 30 °C; reaction time 40 min; catalyst amount: 15 mg; active amount of TSA 3.5 mg.

requires a less trigger effect from the acid catalyst to readily form acetals at ambient reaction conditions.

3.8. Comparison with the reported catalysts

For the present catalyst, catalytic activities for both the reactions are compared with the reported ones, considering the conversion based on glycerol and focusing on selectivity of dioxane derivative.

As seen in Table 8, in case of benzaldehyde, the advantage of present catalyst lies in the best glycerol conversion (95 %) as well as selectivity towards dioxane compared to the reported catalysts. Similarly, for furfural, highest conversion (89 %) as well as double the dioxane selectivity (69 %) is obtained compared to the reported ones. It is interesting to note that while the reported systems have been carried out under comparatively harsher conditions, the present catalyst is highly effective and greener in terms of very less catalyst amount, lower temperature, less reaction time and solvent free condition. The superior activity of the present catalyst can be attributed to the unique acidity of TSA as well as 3D cubic geometry and nano porosity of support which enables the formation of thermodynamically stable derivative at ambient conditions.

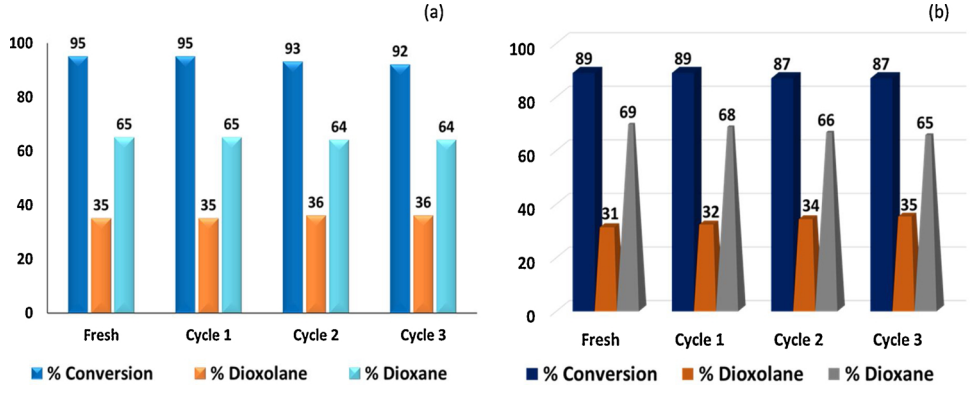

Fig. 12. (a) Reaction conditions: Mole ratio (Glycerol: Benzaldehyde) 1:1; Catalyst amount: 20 mg; Temperature: 30 °C; Time: 40 min. (b) Reaction conditions: Mole ratio (Glycerol: Furfural) 1:1; Catalyst amount: 15 mg; Temperature: 30 °C; Time: 40 min.

Table 8
Comparison with reported catalysts.

Glycerol with benzaldehyde			
Catalyst	Reaction conditions Mole ratio/cat amt /temp/time	% Conversion Glycerol	% Selectivity Dioxane
1% MoO_3/SiO_2 [43]	1.1:1/10 wt%/100 °C/480 min (solvent: toluene)	37	63
10 % MoO_3/SiO_2 [43]	1.1:1/10 wt%/100 °C/480 min (solvent: toluene)	43	62.5
20 %MoO_3/SiO_2 [43]	1.1:1/10 wt%/100 °C/480 min (solvent: toluene)	72	60
10 % MoO_3/TiO_2-ZrO_2 [44]	1:1/5 wt%/100 °C/30 min	74	51
TSA/nMCM-48 (Present work)	1:1/2.17 wt%/30 °C/40 min	95	65
Glycerol with furfural			
SnO_2 [45]	1:1/5 wt%/20 °C/30 min	51	38
WO_3/SnO_2 [45]	1:1/5 wt%/20 °C/30 min	67	37
MoO_3/SnO_2 [45]	1:1/5 wt%/20 °C/30 min	75	36
TSA/nMCM-48 (Present work)	1:1/1.63 wt%/30 °C/40 min	89	69

3.9. Reaction mechanism

The probable reaction mechanism for acid catalysed acetalization of glycerol with benzaldehyde and furfural are shown in Fig. 13 For the reaction of glycerol with benzaldehyde, we have proposed the same mechanism as reported earlier by our group [23].

Similarly, for the acetalization of glycerol with furfural, the first step is initialized by the Bronsted acidity, proton present in TSA, which activates the carbonyl carbon of aldehyde. In the second step, the primary hydroxyl group of glycerol attacks the carbonyl carbon of aldehyde and forms hemiacetal. The subsequent formation of carbocation and removal of water molecule gives the dioxane derivative.

4. Conclusion

In a nutshell, first time nanoporous MCM-48 was successfully synthesized and used as a support for anchoring 12-tungstosilic acid. XRD, N_2- sorption analysis and TEM confirms the 3D cubic geometry and nanoporosity of nMCM-48. Further, the interaction between TSA and nMCM-48 was established by BET as well as ^{29}Si MAS NMR. The synthesized catalyst was used for the synthesis of bio-fuel additives via catalytic valorisation of glycerol and the superiority of the catalyst lies in the inspiring results obtained at ambient reaction conditions. The obtained values of activation energy confirmed that both the reactions were truly governed by a chemical step. As compared to the reported

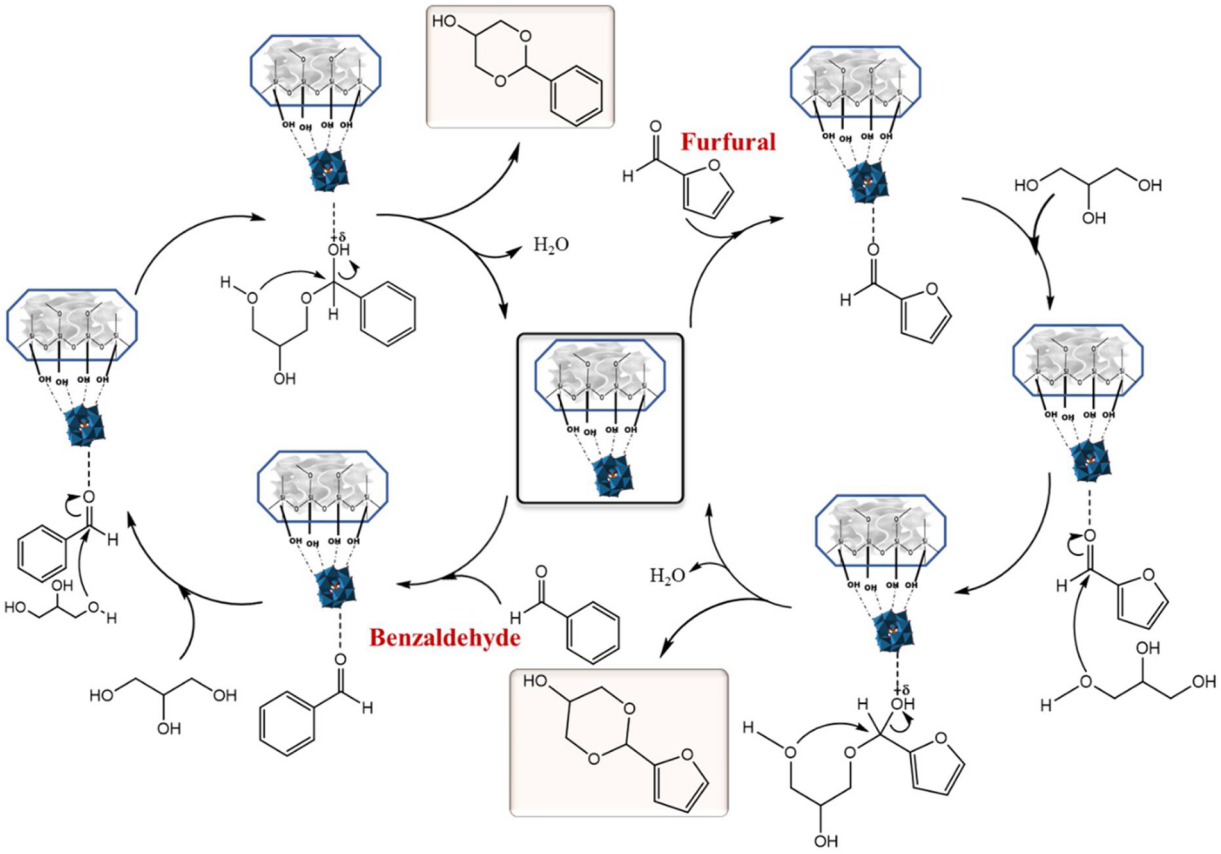

Fig. 13. Plausible reaction mechanism for acetalization of glycerol with benzaldehyde and furfural.

ones, nMCM-48 proves to be better support due to its 3D geometry and nanoporosity which is responsible for higher selectivity of thermodynamically stable dioxane obtained for both the aldehydes. The catalyst was also recycled for consecutive four catalytic cycles and showed consistent conversion rate, thereby contributing effectively in the cost reduction of process as well as making the overall procedure sustainable and environmentally benign.

CRediT authorship contribution statement

Anjali Patel: Conceptualization, Writing - review & editing, Supervision. **Dhruvi Pithadia:** Methodology, Software, Writing - original draft, Writing - review & editing.

Declaration of Competing Interest

There are no conflicts to declare.

Acknowledgements

We are thankful to Dr. N Lingaiah for NH_3-TPD analysis at CSIR-IICT, Hyderabad. We are also thankful to Department of Chemistry, The Maharaja Sayajirao University of Baroda for BET surface area analysis and Sud-chemie India Pvt. Ltd., Nandesari, Vadodara for Powder XRD analysis.

Appendix A. Supplementary data

Supplementary material related to this article can be found, in the online version, at doi:https://doi.org/10.1016/j.apcata.2020.117729.

References

[1] G. Morales, M. Paniagua, J.A. Melero, G. Vicente, C. Ochoa, Ind. Eng. Chem. Res. 50 (2011) 5898–5906.
[2] B. Mallesham, P. Sudarsanam, B.M. Reddy, Ind. Eng. Chem. Res. 53 (2014) 18775–18785.
[3] S.H. Chai, H.P. Wang, Y. Liang, B.Q. Xu, J. Catal. 250 (2007) 342–349.
[4] I. Furikado, T. Miyazawa, S. Koso, A. Shimao, K. Kunimori, K. Tomishige, Green Chem. 9 (2007) 582–588.
[5] S. Bagheri, N.M. Julkapli, W.A. Yehye, Renew. Sustain. Energy Rev. 41 (2015) 113–127.
[6] Y. Wang, J. Zhou, X. Guo, RSC Adv. 5 (2015) 74611–74628.
[7] U. Nda-Umar, I. Ramli, Y. Taufiq-Yap, E. Muhamad, Catalysts 9 (2018) 15.
[8] M.R. Nanda, Z. Yuan, W. Qin, H.S. Ghaziaskar, M.A. Poirier, C.C. Xu, Fuel 117 (2014) 470–477.
[9] A.R. Trifoi, P.Ş. Agachi, T. Pap, Renew. Sustain. Energy Rev. 62 (2016) 804–814.
[10] A.J. Showler, P.A. Darley, Chem. Rev. 67 (1967) 427–440.
[11] IEA, Tracking Transport, IEA, Paris, 2019https://www.iea.org/reports/tracking-transport-2019.
[12] I.S. Gomes, D.C. de Carvalho, A.C. Oliveira, E. Rodríguez-Castellón, S. Tehuacanero-Cuapa, P.T.C. Freire, J.M. Filho, G.D. Saraiva, F.F. de Sousa, R. Lang, Chem. Eng. J. 334 (2018) 1927–1942.
[13] V.T. Vasantha, N.J. Venkatesha, S.Z.M. Shamshuddin, J.Q. D'Souza, B.G.V. Reddy, ChemistrySelect 3 (2018) 602–608.
[14] M.R. Nanda, Z. Yuan, W. Qin, H.S. Ghaziaskar, M.A. Poirier, C.C. Xu, Appl. Energy 123 (2014) 75–81.
[15] M.S. Khayoon, B.H. Hameed, Appl. Catal. A Gen. 464–465 (2013) 191–199.
[16] A. Talebian-Kiakalaieh, N.A.S. Amin, N. Najaafi, S. Tarighi, Front. Chem. 6 (2018) 1–25.
[17] T.H. Abreu, C.I. Meyer, C. Padró, L. Martins, Microporous Mesoporous Mater. 273 (2019) 219–225.
[18] K.S. Arias, A. Garcia-Ortiz, M.J. Climent, A. Corma, S. Iborra, ACS Sustain. Chem. Eng. 6 (2018) 4239–4245.
[19] A. Talebian-Kiakalaieh, S. Tarighi, J. Ind. Eng. Chem. 79 (2019) 452–464.
[20] J.E. Castanheiro, J. Vital, I.M. Fonseca, A.M. Ramos, Catal. Today (2019), https://doi.org/10.1016/j.cattod.2019.04.048.
[21] L. Chen, B. Nohair, D. Zhao, S. Kaliaguine, ChemCatChem 10 (2018) 1918–1925.
[22] L. Chen, B. Nohair, D. Zhao, S. Kaliaguine, Appl. Catal. A Gen. 549 (2018) 207–215.
[23] N. Narkhede, A. Patel, Appl. Catal. A Gen. 515 (2016) 154–163.
[24] L. Chen, B. Nohair, S. Kaliaguine, Appl. Catal. A Gen. 509 (2016) 143–152.
[25] F. Zhang, Y. Jin, J. Shi, Y. Zhong, W. Zhu, M.S. El-Shall, Chem. Eng. J. 269 (2015) 236–244.
[26] M.J. da Silva, A.A. Julio, F.C.S. Dorigetto, RSC Adv. 5 (2015) 44499–44506.
[27] N. Narkhede, A. Patel, RSC Adv. 4 (2014) 19294–19301.
[28] P. Ferreira, I.M. Fonseca, A.M. Ramos, J. Vital, J.E. Castanheiro, Appl. Catal. B Environ. 98 (2010) 94–99.
[29] E. Gutiérrez-Acebo, F. Guerrero-Ruiz, M. Centenero, J.S. Martínez, P. Salagre, Y. Cesteros, Open Chem. 16 (2018) 386–392.
[30] D. Kumar, K. Schumacher, C. Du Fresne von Hohenesche, M. Grün, K.K. Unger, Colloids Surf. A Physicochem. Eng. Asp. 187–188 (2001) 109–116.
[31] N. You, J.H. Yim, S.J. Lee, J.H. Lee, Y.K. Park, J.K. Jeon, J. Nanosci. Nanotechnol. (2007) 3800–3804.
[32] S. Singh, A. Patel, J. Clean. Prod. 72 (2014) 46–56.
[33] Y. Zhang, S. Yang, J. Wuhan Univ. Technol. Mater. Sci. Ed. 23 (2008) 346–349.
[34] D. Bajuk-Bogdanović, I. Holclajtner-Antunović, M. Todorović, U.B. Mioč, J. Zakrzewska, J. Serbian Chem. Soc. 73 (2008) 197–209.
[35] M. Thommes, K. Kaneko, A.V. Neimark, J.P. Olivier, F. Rodriguez-Reinoso, J. Rouquerol, K.S.W. Sing, Pure Appl. Chem. 87 (2015) 1051–1069.
[36] V. Zeleňák, D. Halamová, M. Almáši, L. Žid, A. Zeleňáková, O. Kapusta, Appl. Surf. Sci. 443 (2018) 525–534.
[37] J. Xu, Z. Luan, H. He, W. Zhou, L. Kevan, Chem. Mater. 10 (1998) 3690–3698.
[38] A. Sakthivel, K. Komura, Y. Sugi, Ind. Eng. Chem. Res. 47 (2008) 2538–2544.
[39] D. Carriazo, C. Domingo, C. Martín, V. Rives, J. Solid State Chem. 181 (2008) 2046–2057.
[40] V. Dellarocca, L. Marchese, M.L. Peña, F. Rey, A. Corma, S. Coluccia, Stud. Surf. Sci. Catal. 140 (2001) 209–220.
[41] F.J. Berry, G.R. Derrick, M. Mortimer, Polyhedron 68 (2014) 17–22.
[42] G.C. Bond, Heterogeneous Catalysis: Principles and Applications, Clarendon Press, Oxford, 1974.
[43] S.B. Umbarkar, T.V. Kotbagi, A.V. Biradar, R. Pasricha, J. Chanale, M.K. Dongare, A.S. Mamede, C. Lancelot, E. Payen, J. Mol. Catal. A Chem. 310 (2009) 150–158.
[44] P. Sudarsanam, B. Mallesham, A.N. Prasad, P.S. Reddy, B.M. Reddy, Fuel Process. Technol. 106 (2013) 539–545.
[45] B. Mallesham, P. Sudarsanam, G. Raju, B.M. Reddy, Green Chem. 15 (2013) 478–489.

Environmental Science and Pollution Research
https://doi.org/10.1007/s11356-020-11340-8

RESEARCH ARTICLE

New catalyst comprising Silicotungstic acid and MCM-22 for degradation of some organic dyes

Dhruvi Pithadia[1] · Vinayak Hegde[2] · Varsha P. Brahmkhatri[2] · Anjali Patel[1]

Received: 21 June 2020 / Accepted: 20 October 2020
© Springer-Verlag GmbH Germany, part of Springer Nature 2020

Abstract

A heterogeneous catalyst comprising Keggin type polyoxometalate, silicotungstic acid (SiW_{12}), and MCM-22 was synthesized using wet impregnation method and characterized by acidity measurement, BET, FT-IR, XRD, and SEM. Their catalytic activity was evaluated for the degradation of cationic organic dyes like methylene blue (MB), crystal violet (CV), and an azo dye Chryosidine Y (CY) in an aqueous solution. The experimental parameters such as catalyst amount, initial dye concentration, and contact time were studied for the degradation of dyes, and it was found that the cationic dyes like methylene blue and crystal violet show better activity as compared to azo dye Chryosidine Y. This may be attributed to better electrostatic interaction of these cationic dyes with the residual negative surface charge of the catalyst, due to presence of SiW_{12} ion as it is rich in surface oxygens and surface hydroxyl groups. The control experimental results showed that the presence of SiW_{12} at the surface of MCM-22 promoted the degradation reactions, and presence of multiple W–O bonds in polyoxometalate also played a key role in this reaction. The catalyst exhibits recycling ability without any significant loss in activity up to four cycles.

Keywords Silicotungstic acid · MCM-22 · Heterogeneous catalyst · Dye degradation · Multiple dyes

Introduction

Dyes are primarily used in paints, textiles, printing inks, paper, and plastics that are majorly associated with textile industry (Yaseen and Scholz 2019; Berradi et al. 2019). The natural dyes were replaced by chemical dyes that can bind to the fabric for longer time and retain colour throughout washing and exposure. The chemical dyes are generally soluble and organic in nature. They are classified as reactive, direct, basic, and acidic dyes (Benkhaya et al. 2020). They exhibit high solubility in water making it difficult to remove them by conventional methods. One of its properties is the ability to impart colour to a given substrate, because of the presence of chromophoric groups in its molecular structure (Gürses et al. 2016). However, the property of fixing the colour to the material is related to the polar auxotrophic groups that can bind to polar groups of textile fibres. Exposure to dye-bearing wastewater exhibits severe harmful effect causing an environmental pollution, and it is also associated with health hazards as the degradation products of dyes are carcinogenic in nature (Tkaczyk et al. 2020; Lellis et al. 2019). Due to the adverse effects of dye effluents on environment and health, legislation on the limits of colour discharge by industrial activities has become increasingly strict by the authorities, and treatment of dye water is mandatory before submerging it with natural water bodies (Asolekar et al. 2014).

There are mainly three ways to remove the dyes from polluted water bodies: physical, chemical, and biological methods (Hayat et al. 2015). Many techniques under these categories like reverse osmosis (Wang et al. 2018), electrochemical coagulation (Aragaw 2020), nanofiltration (Khumalo et al. 2019), adsorption (Kumari et al. 2020), oxidation (Dadashi Firouzjaei et al. 2020), electrocatalysis (Singh et al. 2013), and degradation by enzymes and microorganisms (Vikrant et al. 2018) have been explored for the removal of

Dhruvi Pithadia and Vinayak Hegde contributed equally to this work.

Responsible Editor: Santiago V. Luis

✉ Varsha P. Brahmkhatri
b.varsha@jainuniversity.ac.in

✉ Anjali Patel
anjali.patel-chem@msubaroda.ac.in

[1] Polyoxometalates and Catalysis Laboratory, Department of Chemistry, Faculty of Science, The Maharaja Sayajirao University of Baroda, Vadodara, Gujarat 390002, India

[2] Centre for Nano and Material Sciences, Jain University, Jain Global Campus, Bengaluru, Karnataka 562112, India

Published online: 24 October 2020

Table 1 Textural properties and acidity measurement of support and catalysts

Material	Total acidity (mmol g^{-1})	BET surface area (m^2/g)
MCM-22	0.86	267
$(SiW_{12})_1$/MCM-22	0.99	-
$(SiW_{12})_2$/MCM-22	1.11	-
$(SiW_{12})_3$/MCM-22	1.22	234
$(SiW_{12})_4$/MCM-22	1.3	230

dye from wastewater (Han et al. 2016). For the treatment of dye wastewater, it is important to remove dyes and their degradation by oxidation or by catalytic processes.

Polyoxometalate (POM)-based heterogeneous catalysts (Narkhede et al. 2015; Patel and Pathan 2015) are gaining interest in environmental remediation processes including water treatment (Sivakumar et al. 2012; Herrmann et al. 2017). The reports suggest that POM-based materials are coming up as emerging catalyst for dye degradation studies for environmental remediation of dye contaminated water. For example, in an earlier report on resin-supported POMs, parent ($PW_{12}O_{40}^{3-}$) and its lacunary derivative ($PW_{11}O_{39}^{7-}$) were found to catalyse the degradation and partial mineralization of cationic dye pollutants in the presence of H_2O_2 using visible light irradiation (Lei and Chen 2005). In another report, the La^{3+} and Ce^{3+} loaded $H_3PW_{12}O_{40}$ catalysts were explored for photodegradation of methyl orange and rhodamin B under UV and visible light irradiation (Li et al. 2014). With further alterations, an immobilized phosphotungstic acid with zeolite (SBA-15)-modified BiOBr composites was investigated for photocatalytic degradation of methyl orange (Wang et al. 2017). Another catalyst comprising of $H_3PMo_2W_{10}O_{40}$ and $H_3PMo_4W_8O_{40}$@ethylene diamin functionalized magnetic graphene was reported for removal of methylene blue dye (Fakhri et al. 2017). Recently, substituted Keggin type polyoxometalate/hydrotalcites with Mn and Fe were reported for degradation of multiple dyes (Wu et al. 2020). Along with such modifications, report on the utilization of two inorganic-organic hybrid materials based on octamolybdate for wet air oxidation of Bismarck brown (BB), Azure II, Direct blue 71 (DB 71), methyl violet (MV), and methylene blue (MB) showed efficient catalytic degradation activity under mild conditions (Najafi et al. 2015). A new hybrid material comprising POM and metal organic framework (MOFs) $\{[(Cu_4Cl)(CPT)_4]\cdot(HSiW_{12}O_{40})\cdot 31H_2O$ was fabricated and tested for rhodamine B degradation studies (Chen et al. 2018). Another composite catalyst based on POM ($K_6P_2W_{18}O_{62}$ polyoxometalate) encapsulated into mesoporous UiO-66 metal organic framework was reported for degradation of cationic dyes rhodamine B (RhB) and malachite green (MG) and one anionic dye orange G (Zeng et al. 2018). Apart from Keggin type, report on a study of a Dawson heteropoly acid, chemically anchored to the amine-functionalized nanosilica and its photocatalytic degradation efficiency, was explored for an aqueous solution of malachite green (Bamoharram et al. 2014). Also, a nano-POM composite consisting of saturated Dawson anions ($\alpha_2P_2W_{17}CoO_{61}$) was reported for degradation of azo dyes (Grabsi et al. 2019). Likewise, another type of an organic-inorganic hybrid Lindqvist-type polyoxometalate (POM) anions, $\{W_6O_{19}\}^{2-}$, and cucurbituril based photocatalyst was also found to be active for degradation of rhodamine B (Cao et al. 2017).

Above literature survey shows that no reports are available for the utilization of modified zeolites, especially MCM-22, via Keggin type POM, i.e. SiW_{12}, for the degradation of cationic dyes. In present study, for first time, we are reporting the synthesis of a new catalyst, comprising MCM-22 and SiW_{12} for the dye degradation study. The synthesized catalyst was characterized by various physicochemical techniques, and catalytic degradation study was carried out for cationic dyes like methylene blue (MB), crystal violet (CV), and an azo dye

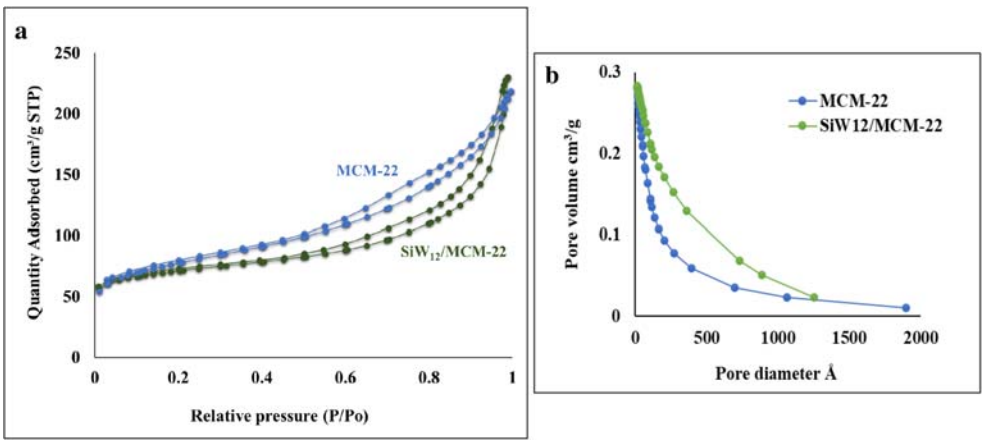

Fig. 1 (**a**) N_2 adsorption-desorption isotherms and (**b**) BJH pore size distribution

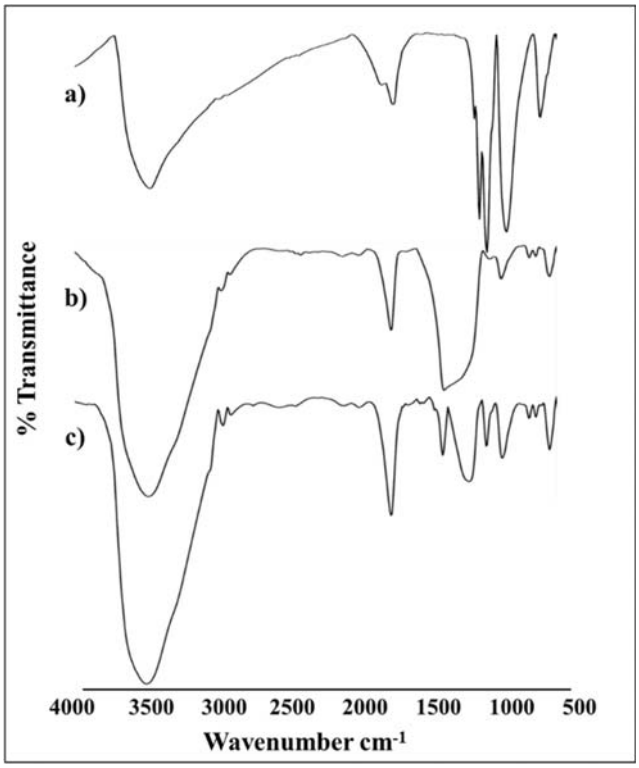

Fig. 2 FT-IR spectra of (**a**) SiW_{12}, (**b**) MCM-22, and (**c**) SiW_{12}/MCM-22

Chryosidine Y (CY). We have investigated various reaction parameters like dye concentration, catalyst amount, and reaction time for the same, and the results demonstrated that the present catalyst could be used for the removal of various dyes from water. The catalyst was recycled up to four cycles of reaction, which indicates the reusability and stability of the catalysts.

Materials and methods

Materials

All chemicals used were of A.R. grade. Silicotungstic acid was used as received from Merck. MCM-22 was acquired commercially from BEE CHEMS (Kanpur, UP). All the three dyes, methylene blue, crystal violet, and an azo dye Chryosidine Y, were received from Nice Chemicals Pvt. Ltd (Bangalore).

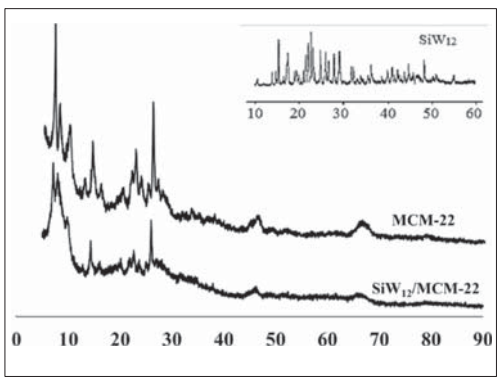

Fig. 3 Powder XRD of support and catalyst

Synthesis of the catalyst (SiW_{12} anchored to MCM-22)

A series of catalysts comprising 10–40% of SiW_{12} anchored to MCM-22 was synthesized by wet impregnation method. Impregnation was carried out by adding 1 g of MCM-22 into aqueous solution of SiW_{12} (0.1 g/10 mL–0.4 g/ 40 ml of distilled water), and the resulting suspension was dried at 100 °C for 10 h. The obtained catalysts were designated as $(SiW_{12})_1$/MCM-22, $(SiW_{12})_2$/MCM-22, $(SiW_{12})_3$/MCM-22, and $(SiW_{12})_4$/MCM-22, respectively.

Characterization

Determination of total acidity by n-butylamine titration method

Total acidity of support and catalyst were determined by performing n-butylamine titration. In 25 ml 0.025 N n-butylamine solution (in toluene), 0.25 g of support/catalyst was suspended and allowed to neutralize for 24 h. Total acidity of support/catalyst was obtained by titrating remaining base against 0.025 N trichloroacetic acid solution in toluene using neutral red indicator.

Physicochemical techniques

BET surface area measurements were carried out in a Micromeritics ASAP 2010 volumetric static adsorption instrument using N_2 adsorption at 77 K and by BJH adsorption-desorption method, and the pore size distributions were calculated. FT-IR analysis was carried out by compelling the solid samples into discs with dry KBr and recorded in the range of 4000–400 cm^{-1} (wave numbers) using Shimadzu instrument (IRAffinity-1S). For X-ray powder diffraction (XRD) patterns, samples were analysed in the 2θ range of 5–90° (CuKα radiation λ = 1.54056 Å) using Philips X′ pert MPD system. Scanning electron microscope (SEM) images were recorded with JSM-7100F scanning electron microscope.

Catalytic activity test

The performance of SiW_{12}/MCM-22 was tested for the degradation of multiple dyes like MB, CV, and CY at room temperature, 28 °C. At regular time intervals, 2 ml of the mixture was taken out from the reaction mixture and filtrated by using a 0.22-μm syringe filter in order to

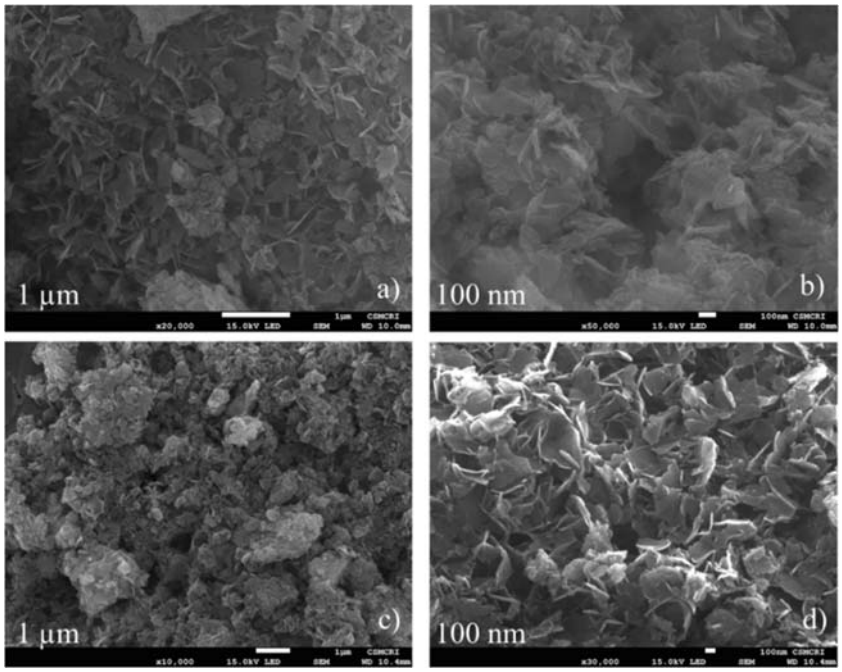

Fig. 4 SEM images of (**a**, **b**) MCM-22 and (**c**, **d**) SiW_{12}/MCM-22

completely remove catalyst particles. The dye concentration in the solution was measured by UV-visible spectrophotometer (ShimadzuUV-1800) at the maximum adsorption wavelength of dye. For recyclability experiments, the catalyst was centrifuged, washed with water, and dried at 60 °C. The following equation was used to calculate dye degradation efficiency.

$$\text{Degradation efficiency}\ (\%) = (C_0 - C)/C_0 \times 100\%$$

where C_0 was the initial dye concentration and C was the dye at certain concentration time t during the reaction.

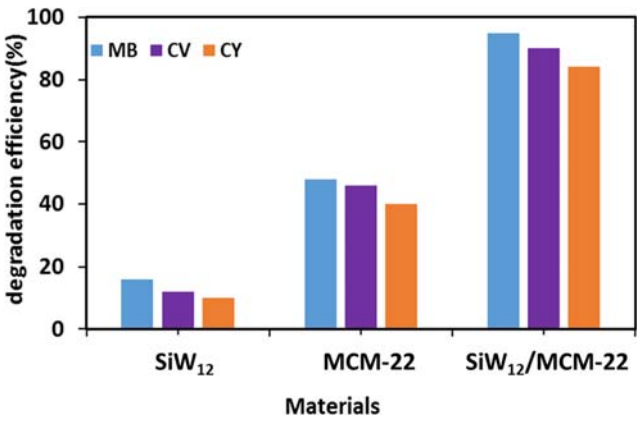

Fig. 5 Control experiments, degradation efficiency of MCM-22, SiW_{12}, and catalyst SiW_{12}/MCM-22. Reaction conditions: dye concentration, 100 ppm; amount of materials taken MCM-22 = 20 mg/mL, SiW_{12}, 1 mg/ml; reaction time, 60 min

Results and discussion

Characterization of catalyst

Textural properties of support and catalyst are shown in Table 1. BET surface area of SiW_{12}/MCM-22 is lower as compared to that of MCM-22, which is the first indication of the incorporation of SiW_{12} species inside the zeolitic pores of MCM-22. From the values of total acidity of support as well as catalysts (Table 1) obtained by n-butylamine titration, it is observed that as the amount of SiW_{12} increases, acidity increases due to the increase in Bronsted acidic sites. Substantial increase in total acidity is observed from 10 to 30% loading of SiW_{12}; however, further increase to 40% does not show any significant effect in acidic sites. This was also supported strongly from the surface area analysis that even though increasing the amount of SiW_{12} to 40%, the surface area almost remains the same as that of 30%. Hence, from the combine view point of surface area as well as acidity, 30% loading of SiW_{12} was considered to be appropriate for detailed characterization and catalytic evaluation, and $(SiW_{12})_3$/MCM-22 is recoded as SiW_{12}/MCM-22.

The N_2 adsorption-desorption isotherms and pore size distribution curve for MCM-22 and SiW_{12}/MCM-22 are shown in Fig. 1 a and b, respectively. The obtained isotherms (Fig. 1a) are of type IV with H4 hysteresis loop, exhibiting a regular trend of zeolites with the presence of micro as well as mesopores in the framework, which is also supported by the pore size distribution curve (Fig. 1b) (Thommes et al. 2015). The adsorption starting at very low P/Po value and extending up to higher relative pressure forms a virtually horizontal

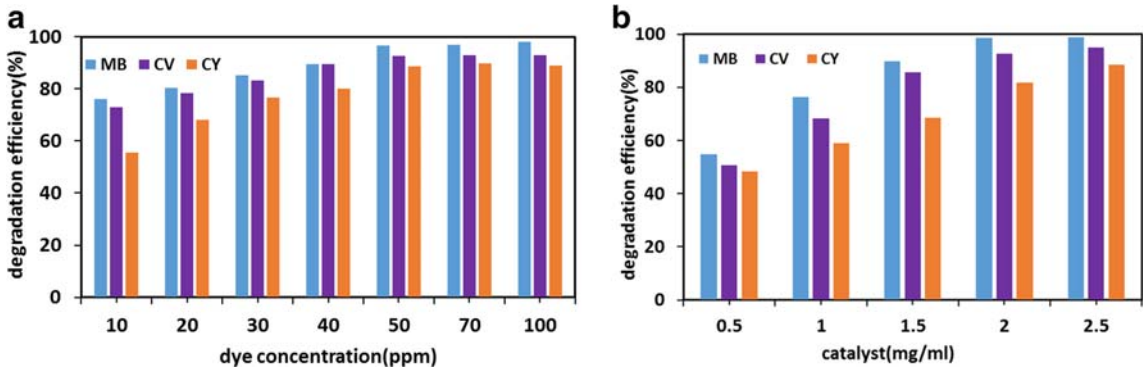

Fig. 6 (**a**) Effect of dye concentration (ppm); the concentration of MB, CV, and CY was varied from 10 to 100 ppm. (**b**) Effect of catalyst amount; the amount of catalyst SiW_{12}/MCM-22 was varied from 0.5 to 2.5 mg/mL; dye concentration, 100 ppm; reaction time, 60 min

plateau which is in good agreement with characteristic zeolitic nature of materials (Delitala et al. 2009). The isotherm curve obtained for SiW_{12}/MCM-22 is identical to that of MCM-22; however, comparative narrow hysteresis loop was observed which suggest the effective filling of SiW_{12} into the pores of MCM-22. This is also confirmed by the lower BET surface area of catalyst as compared to support.

FT-IR spectra of SiW_{12}, MCM-22, and SiW_{12}/MCM-22 are shown in Fig. 2. FT-IR of MCM-22 shows characteristic bands at 3441 cm^{-1}, 1635 cm^{-1}, 1226 cm^{-1}, 817 cm^{-1}, and 455 cm^{-1}. Band at 3441 is due to the O–H stretching of hydroxyl group of loosely bound water molecules. At 817 cm^{-1} and 1226 cm^{-1}, the bands are attributed to the symmetric and asymmetric stretching of T–O–T bond, respectively, where T = Si or Al. Stretching vibration corresponding to T–O, where the metal ion is bonded to four oxygen atoms, is observed at 455 cm^{-1} (Lonare et al. 2018). FT-IR of SiW_{12}/MCM-22 shows an additional band at 925 cm^{-1}, one of the characteristic bands for Keggin unit of SiW_{12} corresponding to asymmetric vibration of ($Si–O_a$). However, the other bands are not distinct due to their superimposition with that of support. Presence of this fingerprint band suggests that the primary of Keggin unit is intact even after impregnation on the support.

The XRD patterns of MCM-22 and SiW_{12}/MCM-22 (Fig. 3) show well-resolved characteristic peaks of MWW zeolitic structure in the range of 2θ 5–30° (Xing et al. 2015), suggesting that the crystalline framework of support remains unchanged even after the impregnation of SiW_{12}. However, less intense peaks are observed for catalyst which can be attributed to the inclusion of SiW_{12} inside MCM-22. Also, absence of the crystalline peaks of SiW_{12} indicates fine dispersion of active species into the support.

SEM images of MCM-22 and SiW_{12}/MCM-22 are shown in Fig. 4. From the images, morphology of MCM-22 appears to have very thin platelets which are interpenetrating each other and forms a lamellar particle. It is noteworthy that even after impregnation of SiW_{12}, there is no alteration as well as aggregation observed in the lamellar structure of MCM-22, indicating the stable morphology of the catalyst.

Table 2 Recycling results

Cycles	% Dye removal efficiency		
	MB	CV	CY
1	99	92	81
2	98	92	81
3	97	91	80
4	96	91	79

Catalytic degradation of dyes (MB, CV, and CY)

In the process of catalytic degradation of organic dyes by POMs, the dye chromophore can be damaged and broken down into smaller fragments or molecules that are less hazardous or non-polluting minor products (Ginimuge and Jyothi 2010). In the present work, the cationic dyes like MB, CV, and an azo dye CY were chosen as representative dyes to evaluate the degradation capability of the catalyst. The control experiments were first conducted to check the activity of original constituents of the catalysts, that is, only SiW_{12} and MCM-22. It is evident from Fig. 5 that the SiW_{12} as such shows the degradation efficiency nearly 16, 12, and 10% for MB, CV, and CY dyes, whereas MCM-22 shows much higher degradation efficiency 48, 46, and 40% for MB, CV, and CY dyes, respectively. The higher degradation efficiency of MCM-22 can be attributed to its high surface area (Table 1) as compared to bare SiW_{12}. The SiW_{12} exhibits surface area as low as < 10 $m^2\ g^{-1}$ with very good solubility in aqueous solvents (Hayashi and Moffat 1982) that makes it difficult to separate from reaction mixture, whereas the catalyst SiW_{12}/MCM-22 exhibits much better degradation efficiency. The large surface area of catalyst as shown in Table 1 enhances the accessibility of catalytic active sites that eventually explains the better dye degradation efficiency of the catalyst. The large surface area and pore diameter of the catalyst enable the greater adsorption of the dye molecules on to the catalyst and accessibility to

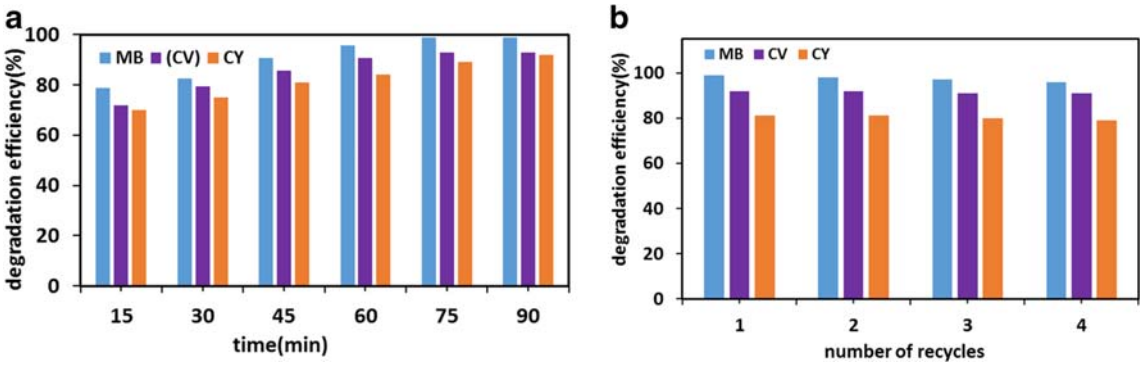

Fig. 7 (**a**) Effect of reaction time (minutes) and (**b**) recyclability of the catalysts

active cites and eventually desorption of degradation products. This explains the better performance of SiW_{12}/MCM-22 as compared to bare SiW_{12} and MCM-22 in dye degradation.

The concentration of all the dyes MB, CV, and CY, were varied from 10 to 100 ppm as depicted in Fig. 6a. Degradation efficiency increases for all the dyes with increase in concentration and then reaches saturation level which may be due to maximum surface coverage of the catalyst by these dyes. Hence all the experiments were carried out in 100 ppm dye concentration. The amount of catalyst was varied from 0.5 to 2.5 mg/ml (Fig. 6b). As the amount of catalyst increases, the degradation efficiency increases as expected. The maximum degradation efficiency as achieved at 2.5 mg/ml catalyst for multiple dyes.

The degradation efficacy of the catalyst was monitored at different time points from 15 to 90 min, and the maximum efficacy was achieved in 60 min itself (Fig. 7a). The trend was similar for all the dyes. Hence, the optimized conditions for multiple dye degradation are as follows: dye concentration, 100 ppm; amount of catalyst, 2 mg/ml; and reaction time 60 min. The catalyst was recycled for all the dye samples, and there was no significant decrease in degradation efficiency up to four cycles (Fig. 7b, Table 2). The recycling results depicts that there is no significant loss in dye removal efficiency up to four cycles with different dyes MB, CV, and CY. These results also indicate that the stability and activity of the catalyst were not perturbed with subsequent recycles. For cationic dyes MB and CV, catalyst shows better activity throughout all the experiments, but for an azo dye CY, the efficacy observed was slightly lower, as CY has residual negative charge at pH 7, and at this pH in water medium, all the experiments were carried out. This is further explained in the mechanism of the dye degradation in the following section.

Mechanism of dye degradation

The proposed oxidative degradation mechanism for multiple dyes MB, CV, and CY with MCM-22-supported POM, SiW_{12}, is schematically depicted in Fig. 8. Due to very high negative charge on $[SiW_{12}O_{40}]^{4-}$ anions, the adsorption mechanism of dye molecules might be predominantly attributed to an electrostatic interaction between the cationic MB and CV dyes with the negatively charged surface of SiW_{12}/MCM-22. Additionally, MCM-22 possesses quite large number of hydroxyl groups on the surface which also facilitates the adsorption of more dye molecules through hydrogen bonding. Once the dye molecules are adsorbed on the surface of the catalyst follows the catalytic degradation of dye molecules into smaller fragments due oxidation where in W in SiW_{12} has a role to play. The CY being a slightly negatively charged

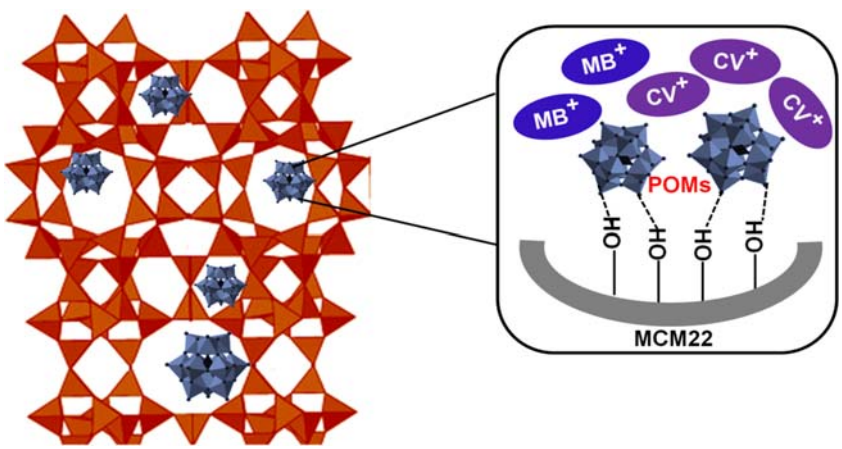

Fig. 8 Proposed mechanism of dye degradation over SiW_{12}/MCM-22 catalyst, electrostatic interaction with negatively charged surface of catalyst with cationic dyes followed by catalytic degradation of dyes by SiW_{12}

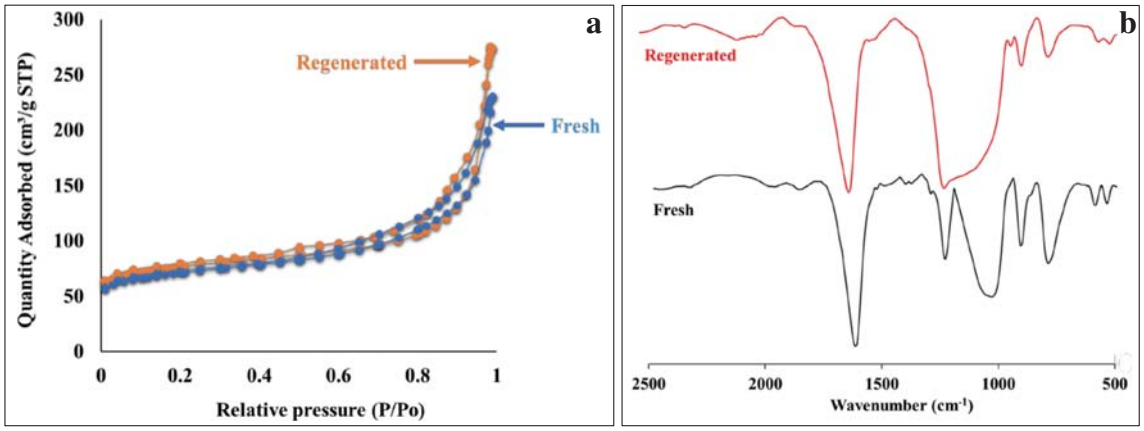

Fig. 9 (**a**) N_2 adsorption-desorption isotherms of fresh and regenerated catalyst and (**b**) FT-IR spectra of fresh and regenerated catalyst

dye molecule might experience slow adsorption on catalyst surface. Specifically, the degradation of MB is well documented in literature (Rauf et al. 2010; He et al. 2018). The oxidation of MB is initiated by demethylation resulting in degradation products of mono-demethylation, di-demethylation, tri-demethylation, and complete demethylation of nitrogen followed by ring opening. The similar results were also reported previously (Rauf et al. 2010, He et al. 2018).

Characterization of regenerated catalyst

To check sustainability of the synthesized catalyst, characterization for regenerated catalyst was performed by carrying out BET surface area and FT-IR analysis. The BET surface area of fresh and regenerated catalyst is 234 and 244 m^2/g, respectively, with parallel N_2 sorption isotherms curves (Fig. 9a), indicating no difference in the structure and nature of catalyst after the reaction. Also, the FT-IR spectra (Fig. 9b) of regenerated catalyst show the presence of all the characteristic bands with no shifting of values. This further confirms that there is no leaching as well as structural change of Keggin unit in the regenerated catalyst. Nevertheless, observed increase in the surface area as well as broadening of the band in FT-IR of regenerated catalyst may be attributed to the adsorption phenomenon that we explained in the mechanism section.

Conclusion

A catalyst, SiW_{12} anchored to MCM-22 was synthesized and characterized by various techniques like BET, FT-IR, XRD, and SEM. The lower BET surface area and pore volume of catalyst SiW_{12}/MCM-22, as compared to that of MCM-22, indicate the incorporation of active species SiW_{12}, inside the zeolitic pores of MCM-22. The uniform dispersion of SiW_{12} on MCM-22 was confirmed by XRD and also the lamellar morphology of MCM-22, and the catalyst was retained as observed in SEM. The catalyst was reported for degradation of cationic and azo dyes. The catalytic dye degradation of various organic dyes like MB and CV and CY was carried out. The comparison between the degradation efficiency of two dyes studies revealed that the catalytic oxidation in the aqueous solutions of cationic dyes like methylene blue (MB) and crystal violet (CV) could be carried out under the same operating conditions. The maximum degradation efficiency was found to be 95% and 90% for MB and CV, respectively, in 60 min, whereas the azo dye Chryosidine Y (CY) exhibits lower degradation efficiency in similar conditions that can be improved at higher time scale. The Chryosidine Y (CY) shows degradation efficiency of 84%. The catalyst was recycled for four cycles, and no significant decrease in activity was observed. Thus, the present material can be a promising catalyst for the management of toxic organic dyes and other pollutants in the coloured wastewater effluents.

Acknowledgement DP is thankful to Department of Chemistry, The Maharaja Sayajirao University of Baroda for all the facilities. AP and DP are thankful to the Department of Chemistry, The Maharaja Sayajirao University of Baroda, Vadodara, for BET measurements. VH and VB are thankful to Jain University, India, for providing facilities.

Authors' contributions Conceptualization: Anjali Patel and Varsha BrahmakhatriMethodology: Dhruvi Pithadia and Vinayak HegdeFormal analysis and investigation: Dhruvi Pithadia and Vinayak HegdeWriting - original draft preparation: Varsha Brahmakhatri, Dhruvi Pithadia, and Vinayak HegdeWriting - review and editing: Anjali PatelSupervision: Anjali Patel and Varsha Brahmakhatri

Data availability Not applicable.

Compliance with ethical standards

Competing interests The authors declare that they have no competing interests.

Ethical approval Not applicable.

Consent to participate Not applicable.

Consent to publish Not applicable.

References

Aragaw TA (2020) Recovery of iron hydroxides from electro-coagulated sludge for adsorption removals of dye wastewater: Adsorption capacity and adsorbent characteristics. Surfaces and Interfaces 18: 100439. https://doi.org/10.1016/j.surfin.2020.100439

Asolekar SR, Kalbar PP, Chaturvedi MKM, Maillacheruvu KY (2014) Rejuvenation of rivers and lakes in India: balancing societal priorities with technological possibilities. Elsevier Ltd.

Bamoharram FF, Niknezhad SH, Baharara J, Ayati A, Ebrahimi M, Heravi MM (2014) Amine-functionalized nanosilica-supported Dawson heteropolyacid: an eco-friendly and reusable photocatalyst for photodegradation of malachite green. J Nanostructure Chem 4. https://doi.org/10.1007/s40097-014-0088-z

Benkhaya S, M'rabet S, El Harfi A (2020) A review on classifications, recent synthesis and applications of textile dyes. Inorg Chem Commun 115:107891. https://doi.org/10.1016/j.inoche.2020.107891

Berradi M, Hsissou R, Khudhair M, Assouag M, Cherkaoui O, el Bachiri A, el Harfi A (2019) Textile finishing dyes and their impact on aquatic environs. Heliyon 5:e02711. https://doi.org/10.1016/j.heliyon.2019.e02711

Cao HL, Cai FY, Huang HB, Karadeniz B, Lü J (2017) Polyoxometalate-cucurbituril molecular solid as photocatalyst for dye degradation under visible light. Inorg Chem Commun 84:164–167. https://doi.org/10.1016/j.inoche.2017.08.021

Chen DM, Liu XH, Zhang NN, Liu CS, du M (2018) Immobilization of polyoxometalate in a cage-based metal–organic framework towards enhanced stability and highly effective dye degradation. Polyhedron 152:108–113. https://doi.org/10.1016/j.poly.2018.05.059

Dadashi Firouzjaei M, Akbari Afkhami F, Rabbani Esfahani M, Turner CH, Nejati S (2020) Experimental and molecular dynamics study on dye removal from water by a graphene oxide-copper-metal organic framework nanocomposite. J Water Process Eng 34:101180. https://doi.org/10.1016/j.jwpe.2020.101180

Delitala C, Alba MD, Becerro AI, Delpiano D, Meloni D, Musu E, Ferino I (2009) Synthesis of MCM-22 zeolites of different Si/Al ratio and their structural, morphological and textural characterisation. Microporous Mesoporous Mater 118:1–10. https://doi.org/10.1016/j.micromeso.2008.07.047

Fakhri H, Mahjoub AR, Aghayan H (2017) Effective removal of methylene blue and cerium by a novel pair set of heteropoly acids based functionalized graphene oxide: adsorption and photocatalytic study. Chem Eng Res Des 120:303–315. https://doi.org/10.1016/j.cherd.2017.02.030

Ginimuge PR, Jyothi SD (2010) Methylene blue: revisited. J Anaesthesiol Clin Pharmacol 4:517–520

Grabsi M, Zabat N, Khellaf N, Ismail F (2019) Synthesis of an environmental nano-polyoxometalate (α2P2W17CoO61)8− as catalyst for dyes degradation: a comparative study oxidation of indigoid and azo dyes. Environ Nanotechnology, Monit Manag 12:100269. https://doi.org/10.1016/j.enmm.2019.100269

Gürses A, Açıkyıldız M, Güneş K, Gürses MS (2016) "Dyes and pigments: their structure and properties" in SpringerBriefs in Green Chemistry for Sustainability. 13–29. https://doi.org/10.1007/978-3-319-33892-7

Han Y, Li H, Liu M, Sang Y, Liang C, Chen J (2016) Purification treatment of dyes wastewater with a novel micro-electrolysis reactor. Sep Purif Technol 170:241–247. https://doi.org/10.1016/j.seppur.2016.06.058

Hayashi H, Moffat JB (1982) The properties of heteropoly acids and the conversion of methanol to hydrocarbons. J Catal 77:473–484. https://doi.org/10.1016/0021-9517(82)90187-7

Hayat H, Mahmood Q, Pervez A, Bhatti ZA, Baig SA (2015) Comparative decolorization of dyes in textile wastewater using biological and chemical treatment. Sep Purif Technol 154:149–153. https://doi.org/10.1016/j.seppur.2015.09.025

He Y, Bin JD, Chen J et al (2018) Synthesis of MnO2 nanosheets on montmorillonite for oxidative degradation and adsorption of methylene blue. J Colloid Interface Sci 510:207–220. https://doi.org/10.1016/j.jcis.2017.09.066

Herrmann S, De Matteis L, de la Fuente JM et al (2017) Removal of multiple contaminants from water by polyoxometalate supported ionic liquid phases (POM-SILPs). Angew Chemie - Int Ed 56: 1667–1670. https://doi.org/10.1002/anie.201611072

Khumalo NP, Vilakati GD, Mhlanga SD, Kuvarega AT, Mamba BB, Li J, Dlamini DS (2019) Dual-functional ultrafiltration nano-enabled PSf/PVA membrane for the removal of Congo red dye. J Water Process Eng 31:100878. https://doi.org/10.1016/j.jwpe.2019.100878

Kumari S, Khan AA, Chowdhury A, Bhakta AK, Mekhalif Z, Hussain S (2020) Efficient and highly selective adsorption of cationic dyes and removal of ciprofloxacin antibiotic by surface modified nickel sulfide nanomaterials: Kinetics, isotherm and adsorption mechanism. Colloids Surfaces A Physicochem Eng Asp 586:124264. https://doi.org/10.1016/j.colsurfa.2019.124264

Lei P, Chen C (2005) Degradation of dye pollutants by immobilized polyoxometalate with H_2O_2 under visible-light irradiation. 39: 8466–8474. https://doi.org/10.1021/es050321g

Lellis B, Fávaro-Polonio CZ, Pamphile JA, Polonio JC (2019) Effects of textile dyes on health and the environment and bioremediation potential of living organisms. Biotechnol Res Innov 3:275–290. https://doi.org/10.1016/j.biori.2019.09.001

Li T, Li Q, Yan J, Li F (2014) Photocatalytic degradation of organic dyes by La3+/Ce 3+-H3PW12O40 under different light irradiation. Dalt Trans 43:9061–9069. https://doi.org/10.1039/c4dt00402g

Lonare MC, Gaikwad SN, Lonare C, et al (2018) Zeolite coated gold nano particles - a versatile nano catalyst. 5:192–214. ISSN NO: 2394-8442

Najafi M, Abbasi A, Masteri-Farahani M, Janczak J (2015) Two novel octamolybdate nanoclusters as catalysts for dye degradation by air under room conditions. Dalt Trans 44:6089–6097. https://doi.org/10.1039/c4dt03377a

Narkhede N, Singh S, Patel A (2015) Recent progress on supported polyoxometalates for biodiesel synthesis via esterification and transesterification. Green Chem 17:89–107. https://doi.org/10.1039/c4gc01743a

Patel A, Pathan S (2015) Springer briefs in molecular science polyoxomolybdates as green catalysts for aerobic oxidation

Rauf MA, Meetani MA, Khaleel A, Ahmed A (2010) Photocatalytic degradation of methylene blue using a mixed catalyst and product analysis by LC/MS. Chem Eng J 157:373–378. https://doi.org/10.1016/j.cej.2009.11.017

Singh S, Srivastava VC, Mall ID (2013) Mechanism of dye degradation during electrochemical treatment. J Phys Chem C 117:15229–15240. https://doi.org/10.1021/jp405289f

Sivakumar R, Thomas J, Yoon M (2012) Polyoxometalate-based molecular/nano composites: advances in environmental remediation by photocatalysis and biomimetic approaches to solar energy conversion. J Photochem Photobiol C Photochem Rev 13:277–298. https://doi.org/10.1016/j.jphotochemrev.2012.08.001

Thommes M, Kaneko K, Neimark AV, Olivier JP, Rodriguez-Reinoso F, Rouquerol J, Sing KSW (2015) Physisorption of gases, with special reference to the evaluation of surface area and pore size distribution (IUPAC Technical Report). Pure Appl Chem 87:1051–1069. https://doi.org/10.1515/pac-2014-1117

Tkaczyk A, Mitrowska K, Posyniak A (2020) Synthetic organic dyes as contaminants of the aquatic environment and their implications for ecosystems: a review. Sci Total Environ 717:137222. https://doi.org/10.1016/j.scitotenv.2020.137222

Vikrant K, Giri BS, Raza N, Roy K, Kim KH, Rai BN, Singh RS (2018) Recent advancements in bioremediation of dye: current status and challenges. Bioresour Technol 253:355–367. https://doi.org/10.1016/j.biortech.2018.01.029

Wang Q, Niu T, Jiao D, Bai Y, Zhong J, Li J, She H, Huang H (2017) Preparation of visible-light-driven BiOBr composites with heteropolyacids ($H_3PW_{12}O_{40}$) encapsulated by a zeolite for the photo-degradation of methyl orange. New J Chem 41:4322–4328. https://doi.org/10.1039/C7NJ00543A

Wang J, Zhang T, Mei Y, Pan B (2018) Treatment of reverse-osmosis concentrate of printing and dyeing wastewater by electro-oxidation process with controlled oxidation-reduction potential (ORP). Chemosphere 201:621–626. https://doi.org/10.1016/j.chemosphere.2018.03.051

Wu X, Luo B, Chen M, Chen F (2020) Tunable surface charge of Fe, Mn substituted polyoxometalates/hydrotalcites for efficient removal of multiple dyes. Appl Surf Sci 509:145344. https://doi.org/10.1016/j.apsusc.2020.145344

Xing E, Shi Y, Xie W, Zhang F, Mu X, Shu X (2015) Synthesis, characterization and application of MCM-22 zeolites via a conventional HMI route and temperature-controlled phase transfer hydrothermal synthesis. RSC Advances 5:8514–8522. https://doi.org/10.1039/C4RA11434E

Yaseen DA, Scholz M (2019) Textile dye wastewater characteristics and constituents of synthetic effluents: a critical review. Springer, Berlin Heidelberg

Zeng L, Xiao L, Long Y, Shi X (2018) Trichloroacetic acid-modulated synthesis of polyoxometalate@UiO-66 for selective adsorption of cationic dyes. J Colloid Interface Sci 516:274–283. https://doi.org/10.1016/j.jcis.2018.01.070

Publisher's note Springer Nature remains neutral with regard to jurisdictional claims in published maps and institutional affiliations.

Biomass and Bioenergy 151 (2021) 106178

Contents lists available at ScienceDirect

Biomass and Bioenergy

journal homepage: www.elsevier.com/locate/biombioe

Conversion of bioplatform molecule, succinic acid to value-added products via esterification over 12-tungstosilicic acid anchored to MCM-22

Dhruvi Pithadia, Anjali Patel *

Polyoxometalates and Catalysis Laboratory, Department of Chemistry, Faculty of Science.,The Maharaja Sayajirao University of Baroda. Vadodara, 390002, Gujarat, India

ARTICLE INFO

Keywords:
Bioplatform molecule
Succinic acid
Diesterification
Heterogeneous catalyst
Anchored 12-tungstosilicic acid

ABSTRACT

The model bioplatform molecule succinic acid, via esterification with n-butanol, leads to succinate esters, promising fuel additives and value-added products. In the present article, the potential application of heterogeneous catalyst comprising silicotungstic acid (SiW_{12}) and MCM-22 (SiW_{12}-MCM-22) was exploited for esterification of succinic acid with n-butanol. Performance of the catalyst was examined by carrying out a detailed optimization study, focusing on the synthesis of diester (one of the excellent fuel additives) and kinetic experiments at different reaction time and temperatures. The experimental results exhibit synergistic effect of SiW_{12} and MCM-22, yielding 97% conversion of acid with 59% selectivity of diester, TON of 1214 and activation energy of 68 $kJmol^{-1}$. Experiments to demonstrates the effectiveness of High Gravity approach were also performed. The green metrics, atom economy (86.47%) (for desired diester) with E-factor (0.69) were calculated. The catalyst was recovered and used for consecutive three catalytic cycles, exhibiting remarkable regenerative activity to synthesize esters and contribute new routes for industrial scale.

1. Introduction

The biorefinery concept is attracting a worldwide mass of scientists and holding its roots in an amazing capability of biomass (a promising alternative source to depleting non-renewable fossils) conversion. However, the transformation of large biomass feedstock to simpler molecules is a challenging and developing domain. In this direction, valorizing biomass can become a commencing objective for converting biobased feedstock including bioplatform molecules to valuable chemicals, commodity materials, and biofuels [1–3].

The US Department Of Energy (USDOE) directed the first original report on the selection of top twelve bio-derived building blocks such as succinic acid, lactic acid, fumaric acid, itaconic acid, levulinic acid, and polyols like sorbitol, glycerol and, xylitol were mentioned [4]. Lately, in 2010 Bozell and Petersen [5] anticipated a revised list of platform chemicals comprising several above molecules, furans and bioethanol.

In these premises, a dicarboxylic acid, succinic acid, has secured its place in both the original USDOE and Bozell's list of platform chemicals. It has proven to be one of the potential bioplatform and an essential starting material for producing valuable commodity chemicals and a successful replacement of maleic anhydride. Several transformations are available to produce value-added chemicals from succinic acid via esterification, hydrogenation, reductive amination, etc. However, the succinate esters are of particular interest due to their vast flora of industrial applications.

The esters of succinic acid, monobutyl succinate and dibutyl succinate, finds several synthetic industrial applications such as plasticizers, perfumery, scent in cosmetics and food products, diluents in paints and coatings, drug intermediate and dyes. Moreover, they possess high oxygen content. Therefore, they can be useful as a green solvent [1] and fuel components, especially dibutyl succinate, which works well as a promising fuel additive due to its lower water miscibility [6,7].

A literature survey shows that in a decade, several fertile attempts are reported for the synthesis of dibutyl succinate using heterogeneous catalysts such as modified ionic liquids [8] and resins [9], immobilized enzymes [10], and heteropoly acid (HPAs) based catalysts [11–14]. Amongst all, looking to the industrial aspects, heteropoly acids (HPAs) are emerging as the new class of potential acid catalysts due to their strong Brønsted acid character. Keggin HPAs are a class of complex inorganic compounds defined by transition metal-oxygen clusters having general formula $[X_xM_mO_y]^{q-}$, where X is the heteroatom from a main group element (i.e. P, Si, Ge, As), and M is the addenda atom, a d-block

* Corresponding author.
E-mail address: anjali.patel-chem@msubaroda.ac.in (A. Patel).

https://doi.org/10.1016/j.biombioe.2021.106178
Received 20 February 2021; Received in revised form 23 June 2021; Accepted 4 July 2021
0961-9534/© 2021 Elsevier Ltd. All rights reserved.

element in high oxidation state, typically $V^{IV, V}$, Mo^{VI} or W^{VI} [15–18].

In 2012, Leng et al. reported the synthesis of a new SO_3H-functionalized HPA-based acidic polymeric hybrid (Poly(VMPS)-PW) and its catalytic performance for the esterification of alcohols with carboxylic acid [11]. During 2011 to 2013, our group reported the synthesis of dibutyl succinate using 12-tungstophosphoric and 12-tungstosilicic acid anchored to MCM-41 [12–14]. A literature survey shows that since last 8 years, no report is available in art for the esterification of succinic acid over supported HPAs and hence, we thought to support 12-tungstosilicic acid on MCM-22 as an extension of the reported work and study its catalytic performance for succinic acid esterification.

The concept of hierarchical zeolites such as Mobil Composite Material- 22 (MCM-22) has attracted attention due to its unique pore structure and acidic nature. It possesses a three-dimensional crystalline structure, with hexagonal morphology having two independent pore systems. One of these systems consists of two-dimensional sinusoidal channels defined by 10-membered rings, whose internal diameter is 4.0 × 5.9 Å, and the other channel system is formed by stacking supercages of 7.1 × 7.1 × 18.2 Å, accessible through 10 member rings. It has a secondary porosity level with a combination of improved pore size and inherent acidity, which have levelled up remarkably the conversion and catalytic rate in many industries [19].

Recently we have reported a novel catalyst comprising silicotungstic acid (SiW_{12}) and a hierarchical zeolite, MCM-22 (SiW_{12}-MCM-22), for the catalytic degradation of organic dyes. It consists of preliminary characterization of the catalyst, mainly focusing on the chemical degradation of dyes [20]. Inspired by the exciting results, we thought to study in-depth characterization and versatility of the catalyst by extending its application for other organic transformation, esterification of succinic acid with n-butanol.

Herein, detailed characterization of the synthesized catalyst was carried out by various physiochemical techniques (elemental analysis, Acidity measurements, BET surface area, FT-IR, Powder XRD, TGA, TEM and ^{29}Si MAS NMR). In the present work, first time we report the catalytic evaluation for the esterification of bioplatform molecule succinic acid with n-butanol to yield diester. The optimization was carried out by varying reaction parameters such as % loading of active species, mole ratio of reactants, catalyst amount, reaction temperature and time. For understanding the process efficiency at high gravity, catalytic runs using different concentrations of succinic acid were carried out. In addition, kinetic experiments were performed for the evaluation of the activation energy of the reaction. The catalyst was regenerated and characterized by potentiometric titration, BET measurements, FT-IR, and used repetitively for three cycles. Furthermore, screening of different alcohols and acid substrates were performed to confirm the versatile reactivity of the catalyst.

2. Experimental

2.1. Materials

All chemicals used were of A.R. grade. 12-tungstosilicic acid (extra pure), succinic acid (99.5%), fumaric acid (99.5%), citric acid (>99%), n-butanol (>98%), Isobutanol (>99%), 1-pentanol (>99%), 1-hexanol (>99%), 1-octanol (>99%) and methanol (>99%) were used as received from Merck. Maleic acid (98%) was acquired from Avra Synthesis Pvt. Ltd. Zeolite MCM-22 was obtained commercially from BEE CHEMS (Kanpur, UP).

2.2. Synthesis of the catalyst (12-tungstosilicic acid (SiW_{12}) anchored to MCM-22)

Catalysts comprising SiW_{12} (10–40%) anchored to MCM-22 were synthesized by wet impregnation method. To the aqueous solution of SiW_{12} (0.1 g in10 mL – 0.4 g in 40 mL of distilled water), 1g of MCM-22 was added and the resulting suspension was dried at 100 °C for 10 h. The obtained catalysts were designated as $(SiW_{12})_1$-MCM-22, $(SiW_{12})_2$-MCM-22, $(SiW_{12})_3$-MCM-22, and $(SiW_{12})_4$-MCM-22, respectively.

2.3. Characterization

2.3.1. Acidic properties

Potentiometric titration method was used to identify the acidic strength and sites of all four synthesized catalysts and the support.

Potentiometric titration. In this method, a suspension of 0.25 g of catalyst or support was prepared in 25 ml of acetonitrile (ACN), stirred for about 12–15 min and initial electrode potential was measured (which indicates its acidic strength). To this suspension, 0.05 N n-butylamine solution in ACN (0.1 ml) was added and allowed to stir for 3 h at 25 °C. Then, potentiometrically, it was titrated against the same solution of n-butylamine and the variation in electrode potential was noted with a digital pH meter.

2.3.2. Physicochemical techniques

Preliminary characterizations with a detailed explanation of Brunauer–Emmett–Teller (BET) surface area, Fourier Transform Infrared Spectroscopy (FT-IR), Powder X-ray Diffraction (XRD) and Scanning Electron Microscopy (SEM) can be found in our recent publication [20]. In the present paper, data of surface area analysis (Table 1) and FT-IR (Table 3) are once again mentioned for the reader's convenience. In addition to this, we have characterized the catalyst for acidity, Thermogravimetric analysis (TGA), solid state ^{29}Si Magic Angle Spinning Nuclear Magnetic Resonance (MAS-NMR) and Transmission electron microscopy (TEM). Energy Dispersive X -ray (EDX) mapping of solid catalyst was performed on JSM-7100F EDX-SEM analyser. The N_2 sorption isotherms and BET surface area measurements were recorded on Micromeritics ASAP 2010 volumetric static adsorption instrument with N_2 adsorption at 77 K. The FT-IR spectra were recorded using Shimadzu IRAffinity-1S instrument in the range of wave numbers 4000–400 cm^{-1}. For thermal characterization, TGA was carried out over Mettler Toledo Star SW 7.01 instrument at 25–600 °C under an inert (nitrogen) atmosphere with a flow rate of 2 mL min^{-1} and ramp rate of 10 °C min^{-1}. The interaction of support and SiW_{12} were detected by performing solid state ^{29}Si MAS NMR on JOEL ECX 400 MHz High resolution multinuclear FT-NMR spectrometer. For TEM, the samples were coated on Cu grid and scanned on JEOL TEM instrument (model-JEM 2100) by applying an acceleration voltage of 200 kV using carbon coated 200 mesh.

2.4. Catalytic esterification procedure

In a general esterification reaction of succinic acid, 10 mmol (1.18 g) of dicarboxylic acid was introduced in a 50 mL batch reactor (with air condenser and guard tube) along with the required amount of catalyst and alcohol. The reaction mixture was allowed to stir vigorously at appropriate temperature and time. After the reaction, the contents were diluted with 10 ml of methanol and analysed using GC-FID (Shimadzu 2014) equipped with RTX-5 capillary column, with an internal diameter of 0.25 mm and length: 30 m. The products were also identified using GC-MS (Gas chromatography-mass spectrometry- Thermo scientific DSQ-II) with a capillary column- Thermo TR-MS.

The Turnover number (TON) is denoted by the number of moles of product formed per mole of catalyst. The following equation calculates it,

Moles of catalyst refers to the active amount of SiW_{12}.

2.5. Leaching and hot filtration test

The leaching of SiW_{12} from the support was checked by following the same procedure reported earlier [21]. Qualitative determination of heteropoly acids can be done by treating it with a mild reducing agent such as ascorbic acid, giving heteropoly blue colouration. 1 g of SiW_{12}

loaded MCM-22 was suspended and kept in 10 ml water for 24 h. The supernatant solution was then decanted and treated with ascorbic acid solution and no blue colouration was observed which indicates absence of leaching of SiW_{12} from the hold of MCM-22.

The leaching of SiW_{12} was also checked in the residue obtained after the reaction by hot filtration test. After the completion of reaction (at 90 °C), the reaction mass was filtered hot and the obtained filtrate was treated with the solution of ascorbic acid. The absence of blue colour indicates no leaching of SiW_{12} from MCM-22.

2.6. Recycling of catalyst

After the first cycle, the reaction mixture was diluted with methanol and the catalyst was separated by centrifugation method. The collected catalyst was then washed with 5 ml of fresh methanol, followed by water, and dried in an oven at 100 °C till the complete evaporation of the solvent and employed for the next cycle.

3. Results and discussion

3.1. Detailed characterization

BET surface area of support and catalysts are mentioned in Table 1. As observed, when the amount of SiW_{12} increases from 10 to 30%, the surface area decreases, which is the first indication of the incorporation

Table 1
Acidity measurements of synthesized materials and textural properties.

Material	Potentiometric titration				BET surface area (m^2/g)
	Acidic strength (mV)	Types of acidic sites (mEq g^{-1})		Total No. of acidic sites (mEq g^{-1})	
		Very strong	Strong		
[1]MCM-22	132	0.2	1.4	1.4	267
$(SiW_{12})_1$-MCM-22	258	0.6	1.1	1.7	259
$(SiW_{12})_2$-MCM-22	382	1.4	1.0	2.4	243
[2]$(SiW_{12})_3$-MCM-22	456	2.2	1.5	3.7	234
$(SiW_{12})_4$-MCM-22	482	2.1	1.8	3.9	230

Pore diameter 1 = 94 Å, 2 = 60.83 Å; Pore volume 1 = 0.63 cm^3g^{-1}, 2 = 0.35 cm^3g^{-1}

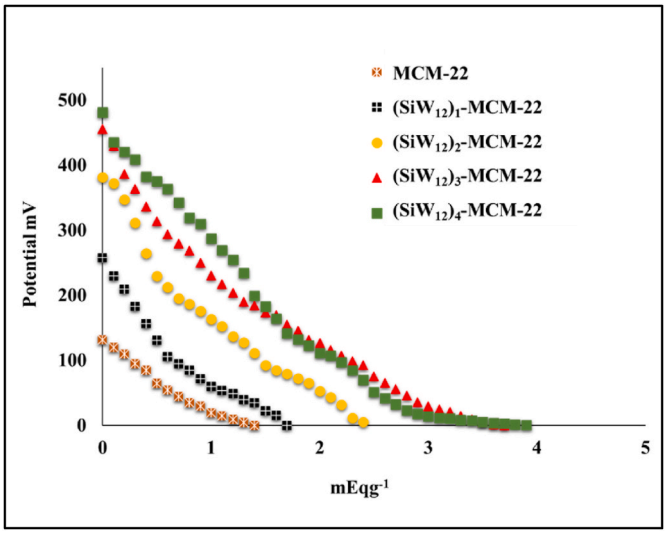

Fig. 1. Potentiometric titration curves of support and catalysts.

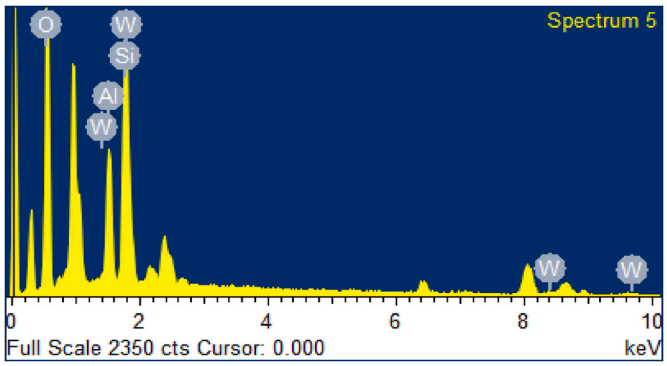

Fig. 2. EDX mapping of SiW_{12}-MCM-22.

Table 2
Elemental analysis of SiW_{12}-MCM-22.

Material	Si (wt%)	O (wt%)	Al(wt%)	W (wt%)	
				By EDX	Theoretical
SiW_{12}-MCM-22	19.43	53.86	9.38	17.33	17.7

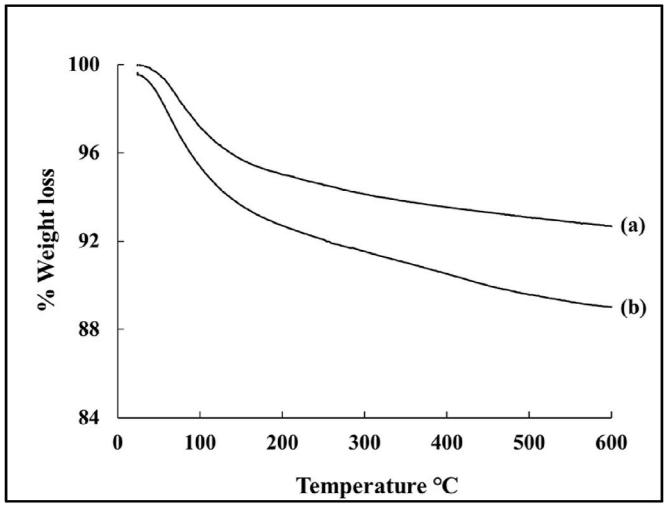

Fig. 3. TGA plots of (a) MCM-22 and (b) SiW_{12}-MCM-22.

of SiW_{12} species inside the zeolitic pores of MCM-22. But, when the concentration increases from 30 to 40%, the surface area remains almost constant. Therefore, 30% loading of SiW_{12} was considered to be appropriate.

Table 1 shows the results obtained from the potentiometric titration and the change in the electrode potential as a function of mEq per g of nbutylamine is shown in Fig. 1. The acidic sites were assigned according to the following scale: Ei > 100 mV (very strong sites), 0 < Ei < 100 mV (strong sites), −100 < Ei < 0 mV (weak sites) and Ei < −100 mV (very weak sites) [22]. The initial electrode potential, also known as acidic strength of MCM-22, increases with the inclusion of active acidic species i.e., SiW_{12}. Additionally, the acidic sites of the catalysts were found to increase from 10% to 30%, which directs the enriched distribution of SiW_{12} into the pores of the support. Conversely, when the amount of SiW_{12} increased to 40%, the acidic strength and the sites remain almost the same. This observation was well supported by no significant change in the BET surface area. Henceforth, we choose 30% to be the appropriate loading amount and further characterization of $(SiW_{12})_3$-MCM-22 was performed and renamed it as SiW_{12}-MCM-22.

For detecting the effective loading of SiW_{12} onto MCM-22, elemental

Table 3
Infrared absorption bands.

Support/ catalyst	FT-IR Wavenumbers (cm^{-1})						
	ν_s OH	ν_{as} T-O-T (T = Si or Al)	ν_{as} Si-O_a	Ns W=O	ν_{as} W–O–W	ν_s T-O-T (T = Si or Al)	ν_s T-O (T = Si or Al)
SiW_{12}	3402	-	926	980	878, 779	-	-
MCM-22	3441	1226	-	-	-	817	455
SiW_{12}-MCM-22	3456	1249	925	-	-	810	455

analysis was carried out by performing the EDX mapping (Fig. 2). The obtained result in terms of wt % of tungsten (W) (Table 2) for SiW_{12}-MCM-22 was in good agreement with the theoretically calculated value. Hence, it can be confirmed that the desired amount of SiW_{12} has been successfully impregnated onto the support.

The TGA profile for support and catalyst are presented in Fig. 3. For MCM-22, weight loss occurs mainly in two steps. The first weight loss of approximately 4.7% was observed up to 135 °C due to the loss of physically adsorbed water molecules while the second weight loss occurs above 200 °C of 2.5% which may be due to the decomposition of the template, which was not completely removed [23]. For SiW_{12}-MCM-22, comparatively, the rise in the weight loss (7.3%) up to 144 °C was observed for the removal of adsorbed water molecules. At 200–310 °C, a gradual weight of 2.1% was seen for the crystalline water molecules present in Keggin unit. Thus, further weight for catalyst was not observed which indicates its stability up to 500 °C.

The FT-IR bands of support and catalyst are mentioned in Table 3. MCM-22 shows characteristic bands at 3441 cm^{-1}, 1226 cm^{-1}, 817 cm^{-1}, and 455 cm^{-1}. The Band at 3441 corresponds to the O–H stretching of hydroxyl group. Asymmetric and symmetric stretching bands corresponding to T–O–T (T = Si or Al) bond appear at 817 cm^{-1} and 1226 cm^{-1}, respectively. At 455 cm^{-1}, stretching vibration corresponding to T–O is observed [24]. In the FT-IR of SiW_{12}/MCM-22, an additional band at 925 cm^{-1} is observed, one of the characteristic bands for the Keggin unit of SiW_{12} corresponding to the asymmetric vibration of (Si–Oa). However, the other characteristic bands of keggin unit are not observed due to their superimposition with that of support. The presence of this fingerprint band suggests that the primary of the Keggin unit is intact even after impregnation on the support.

The ^{29}Si MAS NMR for MCM-22 (Supplementary Fig. S1A) shows a distinct peak at −99.34 ppm corresponding to the Si associated with one Al unit and a range of small peaks from −102 to −118 ppm due to the other Si (which are not surrounded by Al atoms) present in MCM-22. In the NMR spectra of SiW_{12}-MCM-22 (Supplementary Fig. S1B), the first peak shifts slightly to −98 ppm. Interestingly, the rise in the intensities of the bunch of peaks (−100.84 to −113.6 ppm) indicates an increase of Si in the framework. These extra sites come from SiW_{12}, suggesting the firm interaction of it with the support framework.

TEM images of MCM-22 (Fig. 4A and B) exhibit the uniform aggregates formed by the growth of flaky crystals. Through close proximity, a little bit of indistinct pore networks are observed [23]. After impregnation of SiW_{12}, the transparent networks of pores appear to be opaque, indicating uniform filling inside the channels of MCM-22 (Fig. 4C and D). This observation was also supported by the XRD patterns given in our previous article [20], where the crystalline peaks of heteropoly acid are absent, indicating its fine dispersion.

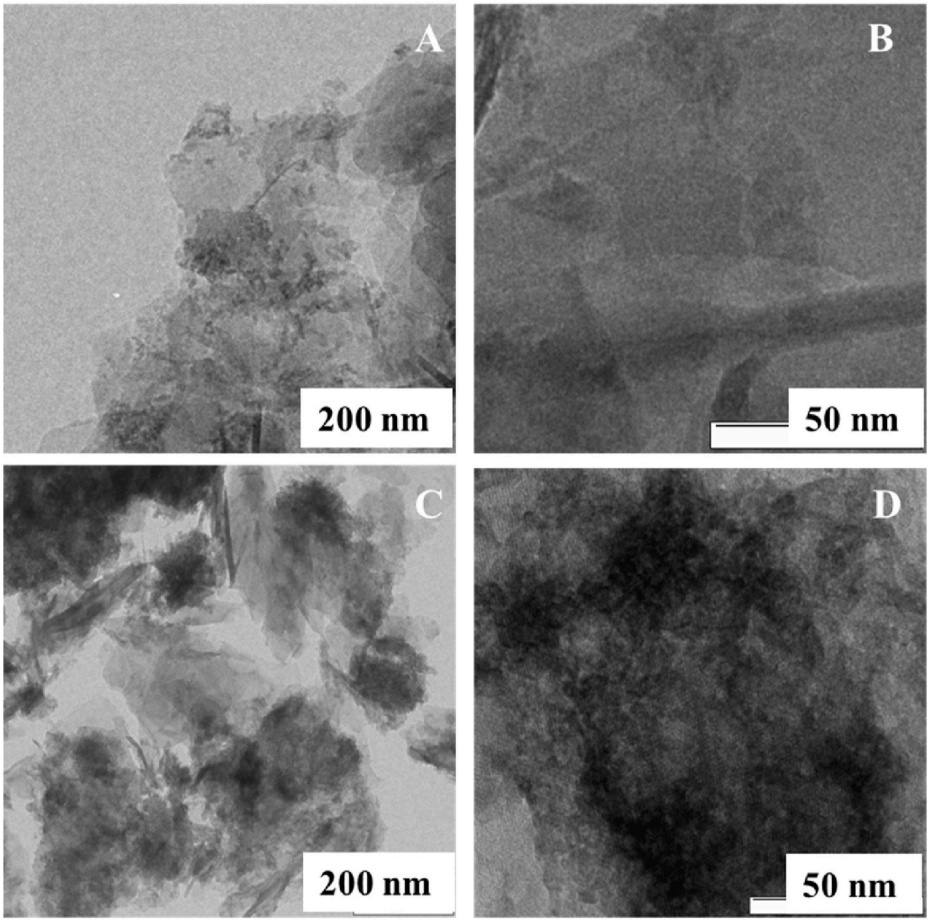

Fig. 4. TEM images of MCM-22 A, B & SiW_{12}-MCM-22C, D.

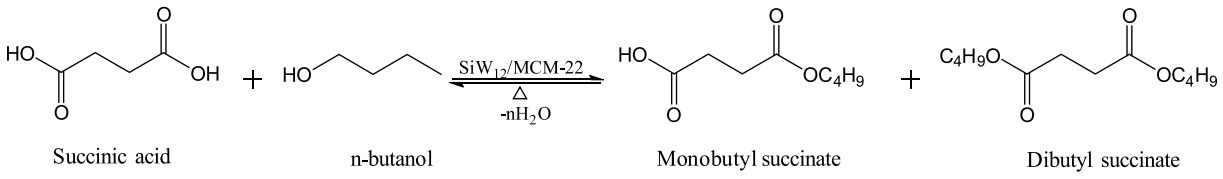

Scheme 1. Esterification of succinic acid with n-butanol.

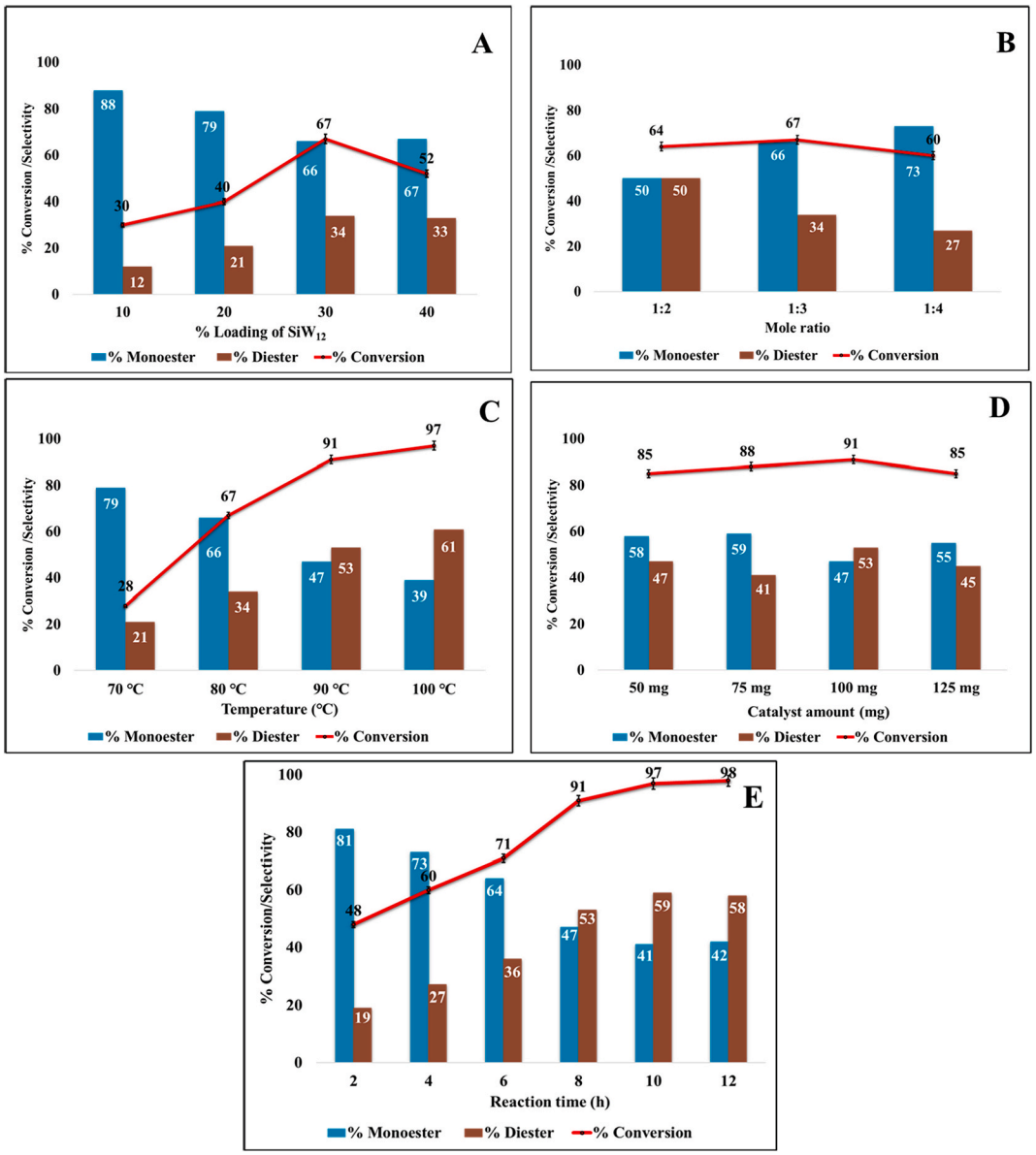

Fig. 5. (A) Influence of % loading of SiW_{12}. Mole ratio: 1:3; Catalyst amount: 100 mg; Temperature: 80 °C; Time: 8 h; (B) Influence of mole ratio. Catalyst amount: 100 mg; Temperature: 80 °C; Time: 8 h; (C) Influence of reaction temperature. Mole ratio: 1:3; Catalyst amount: 100 mg; Time: 8 h; (D) Influence of catalyst amount. Mole ratio: 1:3; Temperature: 90 °C; Time: 8 h; (E) Influence of reaction time. Mole ratio: 1:3; Catalyst amount: 100 mg; Temperature: 90 °C.

3.2. Optimization of esterification conditions for succinic acid in n-butanol

Esterification of succinic acid with n-butanol generates monobutyl succinate (monoester) and dibutyl succinate (Diester) (Scheme 1).

Effect of loading amount of SiW_{12}, mole ratio of reactants, temperature, catalyst amount and time were screened thoroughly to investigate the catalytic performance of synthesized catalyst and achieve the appropriate reaction conditions for selective synthesis of dibutyl succinate.

Fig. 5A shows the influence of % loading of SiW_{12}. It was observed that the reaction progresses well with the increase in the amount of SiW_{12} from 10 to 30%. It can be attributed directly to the increase in the Brønsted acid sites of the catalyst. But, the conversion of succinic acid in case of 40% SiW_{12} decreases. It may be due to the blocking of active sites of support, which does not allow reactant molecules to access active catalytic sites. A similar effect was also observed in acidity measurements. Thus, 30% loading was optimized for the study of other reaction

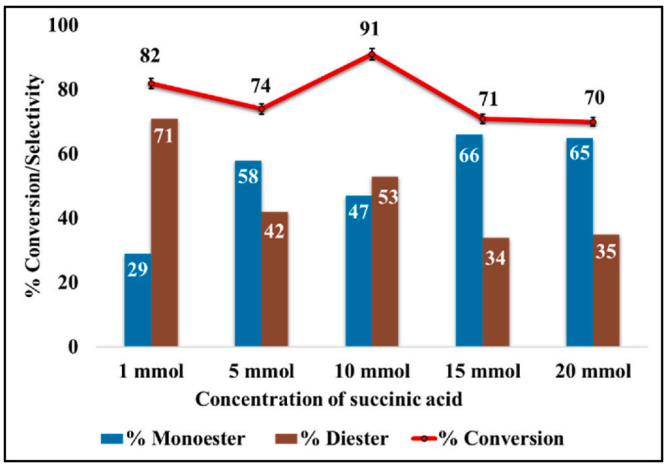

Fig. 6. Different concentration of succinic acid Conditions: Mole ratio: 1:3; Catalyst amount: 100 mg; Temperature: 90 °C; Time: 8 h.

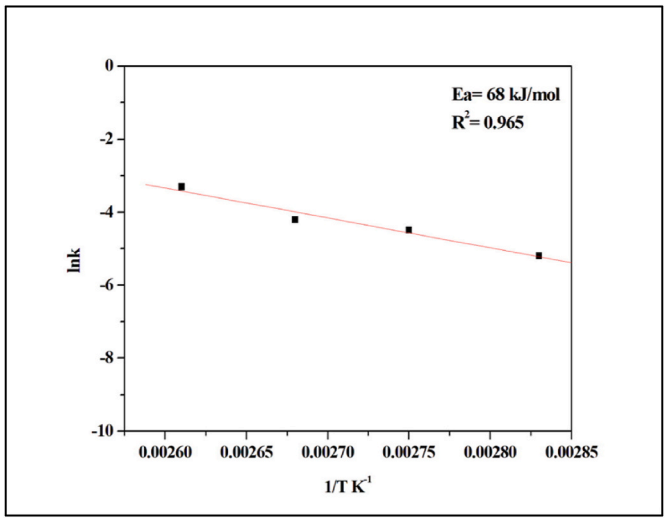

Fig. 7. Plot of lnk vs $\frac{1}{T}$.

parameters.

Slight excess of alcohol is required for an esterification reaction to proceed in a forward direction. Hence, the mole ratio of acid to alcohol from 1:2 to 1:4 was screened (Fig. 5B). As the mole ratio increases from 1:2 to 1:3, the conversion of succinic acid also rises from 63 to 67% with 66% monoester selectivity and 34% diester. However, with a further rise in alcohol concentration, the conversion rate decreases to 60%. For the initial feasibility of catalytic activity, focus was driven more on the conversion rate of acid. Thus, a 1:3 ratio of acid to alcohol was selected for the optimization study.

The reaction temperature is the key parameter that has a significant effect on an esterification process. Esterification of succinic acid was carried out at four different temperatures (70 to 100 °C) (Fig. 5C) to understand the trend of product formation. Expectedly, a dramatic increase in the formation of esters from 28 to 91% was observed with a rise in temperature up to 90 °C. At the same time, the selectivity of diester boosts to 53%. Conversely, when the reaction was allowed to proceed at 100 °C, a minimal increase in the conversion and selectivity was obtained. Therefore, 90 °C was found to be the optimum temperature.

To study the effect of catalyst amount, reactions were carried out in the range of 50 to 125 mg and the results are presented in Fig. 5D. The reaction tends to proceed forward when the catalyst amount was raised to 100 mg. The more the available catalytic sites, the more the conversion of acid to ester and the better the selectivity of diester was obtained. But, when 125 mg of catalyst was used, a decline in the conversion and selectivity was observed. This drop may be attributed to the increase in mass density due to the solvent-free reaction pathway. Accordingly, 100 mg of catalyst concentration can be assessed as a required amount. Similar experiments were carried out for 6 h (where the reactants are not depleted) to understand the impact of changing catalyst amount at lower conversion [25]. The results are shown in Supplementary Information Fig. S2. As seen, initially the reaction gives appreciable activity for 50 mg (57% conversion) to 100 mg (71% conversion). Above that (125 mg), the conversion rate decreases to 66%. Hence, a similar trend was observed, and 100 mg catalyst amount was found to be optimum.

Another most essential reaction parameter which controls the reaction rate is the reaction time. For evaluation of required time, the reaction was carried out at different time intervals from 2 h to 12 h (Fig. 5E). With progression in reaction time (2 to 10 h), conversion and selectivity increase from 48 to 97% and 19 to 59%, respectively. But, when the reaction prolonged to 12 h, no change in both the conversion and selectivity was observed. Hence, 10 h was optimized as the required reaction time.

For maximum conversion of succinic acid (97%) and selectivity of diester (59%), the optimized reaction conditions are: mole ratio of acid to alcohol = 1:3; reaction temperature = 90 °C; catalyst amount = 100 mg, substrate: catalyst ratio (mol: mol) 1251:1 and reaction time = 10 h. At these conditions, the TON was found to be 1214 and the specific activity of the catalyst was found to be 148 h^{-1} at 6 h.

The green chemistry metrics were also calculated (supplementary information) for atom economy (for the desired diester) and E-factor. They were found to be 86.47% and 0.69, respectively, indicating a greener and cleaner reaction.

3.3. Study on high gravity approach

Effect of concentration of succinic acid was studied as an important parameter in the perspective of the High Gravity Approach for industrial implementation [26]. The reactions were carried out by taking 1 mmol to 20 mmol succinic acid and the results are shown in Fig. 6. Initially, at a lower concentration of succinic acid, a huge amount of acid sites is available and the reaction proceeds to give 82% conversion with 71% diester. Further increasing the concentration to 10 mmol, the process showed excellent activity towards conversion with 91% product formation, indicating the ability of the catalyst to deliver activity at a larger scale. However, on further increase, keeping the same amount of catalyst, a decrease in the conversion rate was observed. At High Gravity conditions, above 10 mmol, the problem of inappropriate stirring of the reaction mass was observed due to slurry formation [27] and at lower concentration (5 mmol) the process does not seem to be economically viable. Thus, a higher conversion rate at 10 mmol highlights the effectiveness of the High Gravity Approach using this process and addresses the technological challenges for the production of biofuel additive at high gravity.

3.4. Kinetics: determination of activation energy (E_a)

For any catalytic reaction to happen, the activation energy determines how decent and fast is the interaction between the catalyst and reactants. The activation energy for succinic acid esterification using the synthesized catalyst was obtained by performing the reactions at a temperature range of 80 °C to 110 °C for different time intervals by keeping the other reaction parameters similar to the optimized condition. For each temperature, the rate constant was calculated (Supplementary Fig. S3) and the graph of ln k vs $\frac{1}{T}$ (kelvin^{-1}) was plotted (Fig. 7). Using the Arrhenius equation, the activation energy was calculated from the slope of the graph and found to be 68 kJmol^{-1} (Table 4).

Table 4
Rate constants (k $M^{-1}min^{-1}$) at different temperatures and activation energy (Ea).

Temperature (K)	Rate constant k ($M^{-1}min^{-1}$)	Activation energy E_a (kJ/mol)
353	5.52×10^{-3}	68
363	1.12×10^{-2}	
373	1.49×10^{-2}	
383	3.70×10^{-2}	

Table 5
Control experiments.

Catalysts	% Conversion	% Selectivity		TON[a]
		Monoester	Diester	
[1]MCM-22	64	64	36	-
[2]SiW_{12}	100	02	98	1251
[3]SiW_{12}/MCM-22	97	41	59	1214

Reaction conditions: mole ratio 1:3, reaction temperature 90 °C, reaction time: 10 h,
Catalyst amount 1 = 77 mg, 2 = 23 mg (Active amount of SiW_{12}), 3 = 100 mg.
[a] Calculated using active amount of SiW_{12}.

Also, it is well-known that if the activation energy is lower i.e., 10–15 $kJmol^{-1}$, then the reaction is said to be diffusion-limited. On the other hand, if the activation energy for any reaction exceeds 25 $kJmol^{-1}$, the reaction is governed by a truly chemical step [28]. Therefore, the obtained activation energy of 68 $kJmol^{-1}$ for the present reaction confirms that the catalytic process truly follows a chemical step.

3.5. Control experiments and effect of support

The results of control experiments carried out using MCM-22 and SiW_{12} are depicted in Table 5. With MCM-22, the reaction proceeds to give 64% conversion with 36% selectivity of diester, while SiW_{12} gives complete conversion with 98% of diester. The obtained conversion of 97% with SiW_{12}-MCM-22 confirms that we have successfully synthesized a truly heterogeneous catalyst. At the same time higher selectivity of diester (59%) also demonstrates the synergic effect of MCM-22 and SiW_{12}. This observation can be very well correlated with the acidity obtained by the potentiometric titration method. In SiW_{12}-MCM-22, a tremendous increase in the very strong acidic sites from 0.2 to 2.2 $mEqg^{-1}$ and total acidic sites from 1.4 to 3.7 $mEqg^{-1}$ was observed. It may be because of the increase in the Brønsted acidity due to the presence of SiW_{12}, suggesting that the Brønsted acidity plays an important role in higher conversion and diester selectivity. Furthermore, it should be noted that the existence of weak Lewis acidic sites (Al sites) in the support also plays an essential role in governing the selectivity of monoester. The Lewis acid sites present in the support MCM-22 can catalyse the monoesterification reaction (monoester formation) and only, to some extent diesterification (It is observed in Fig. 5A). However, for esterification of second carboxylic acid group (diester formation), more of the strong acid sites are required which are obtained from the Brønsted acidity present in SiW_{12}. Hence, the overall observation from the control experiments confirms that we have efficiently synthesized heterogeneous catalyst and it synergistically works well for the esterification reaction.

3.6. Recycling studies

For the development of an efficient process, recycling of the catalyst becomes inevitable. The sustainability and credibility of the heterogeneous catalyst were tested by reusing it for three successive cycles (Table 6). From the results tabulated, it was observed that, for all the cycles, the catalyst showed consistent activity with no change in the rate of conversion and selectivity of the desired ester till cycle 2. In contrast, negligible change of 2% was observed in cycle 3. It also confirms that no leaching of the active keggin unit occurs during the reaction and the catalyst is stable.

Table 6
Recycling experiments.

Cycles	% Conversion	% Selectivity of diester
Fresh	97	59
Cycle 1	97	58
Cycle 2	95	58
Cycle 3	93	54

Reaction conditions: mole ratio 1:3, reaction temperature 90 °C, catalyst amount 100 mg, reaction time: 10 h.

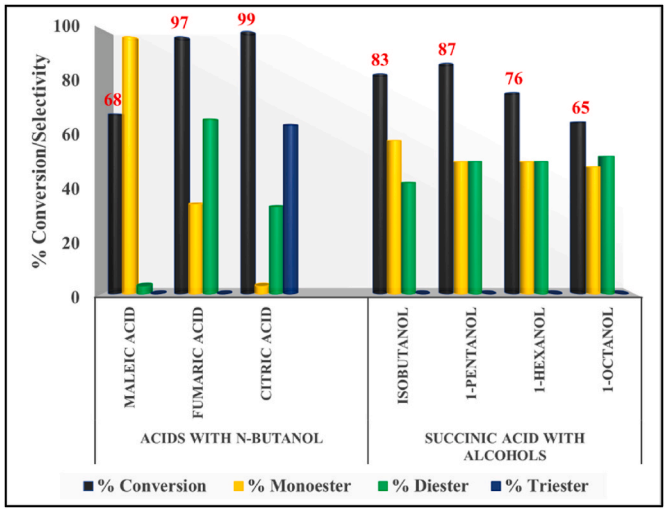

Fig. 8. Reactivity of different acids and alcohols. Reaction conditions. Mole ratio: 1:3; Catalyst amount: 100 mg; Temperature: 90 °C; Time: 10 h.

3.7. Characterization of recycled catalyst

The recycled catalyst was characterized by BET surface area and FT-IR analysis to check the stability and intact structure. The N_2 sorption isotherms (Supplementary Fig. S4A) for both fresh and regenerated catalyst demonstrates identical isotherms along with almost alike surface area, 234 and 244 m^2g^{-1} respectively. This observation leads to the confirmation of the intact structure of the catalyst. Furthermore, in FT-IR analysis (Supplementary Fig. S4B), the presence of all the characteristic bands of keggin unit and that of the support indicates the stability and firm interaction of SiW_{12} with MCM-22. However, a slight drop in the intensity of bands was observed, which may be due to the regeneration step. Both the characterization in combined terms suggest no leaching of the active species from the support, also confirmed previously in the recycling study.

3.8. Relative reactivity of different acids and alcohols

To understand the versatile employability of the catalyst, organic acids with multiple functional groups and some branched as well as long chain alcohols were evaluated for their esterification reaction.

Screening of few organic acids, maleic acid, fumaric acid and citric acid, were carried in the optimized conditions and the results are presented in Fig. 8. The catalyst showed excellent activity in the formation of respective esters and inevitably signifies the versatile catalytic approach with any acid from simple to complex ones. Interestingly, different behaviour of maleic acid with respect to other acids (fumaric acid, succinic acid and citric acid) with n-butanol was observed, which

Table 7
Comparison with reported catalysts.

Entry	Catalyst	Concentration of succinic acid	Reaction conditions mole ratio/amount (g)/temp (°C)/time (h)	Solvent	% Conv	Reference
1	CALB-CheapTubes™ MWCNTs nanobiocatalysts.	1 mmol	1:4/0.15/45/3	Cyclohexane	95	[8]
2	Mg–Cl-D002	500 mmol	1:3/5.1/120/1	Cyclohexane	91.6[a]	[7]
3	Poly(VMPS)-PW	30 mmol	1:4/0.20/130/3	-	96.4	[9]
4	SiW_{12}-MCM-22	10 mmol	1:3/0.1/90/10	-	97	Present work

[a] Yield of dibutyl succinate.

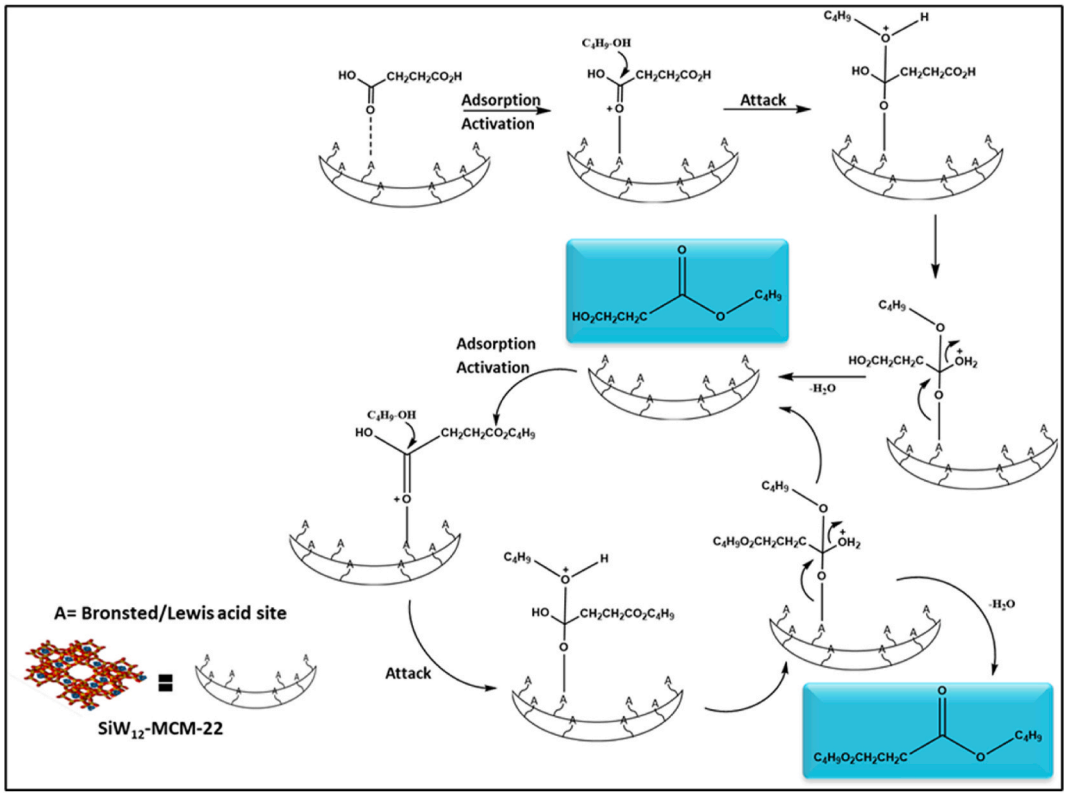

Fig. 9. Probable mechanism for esterification of succinic acid with n-butanol.

may be due to the cis geometry of the double bond that may lead to the steric hindrance during the reaction and restricts the approach of the second molecule of n-butanol (diesterification reaction). Hence, we obtain higher selectivity of monoester. Also, when the reactions were employed for different alcohols, appreciable conversion and expected trends in the results were observed. From simple four carbon chain primary alcohol to eight carbon chain, the conversion slightly decreases. Furthermore, when the branched chain butyl alcohol (isobutyl alcohol) was used, conversion decreases to 83%.

Notably, one thing is certain that steric hindrance plays a vital role in esterification [29]. As we go on indulging long chain or branched alcohols, a little bit of low reactivity was observed compared to their respective simpler alcohols. Nevertheless, the progress in each substrate yields the products, which is the best point to explain the well exploitation of synthesized catalyst.

3.9. Comparison with reported catalysts

The catalytic activity for the present catalyst is compared with the reported heterogeneous catalysts (Table 7). All the catalysts show appreciable conversion compared to the present catalyst. However, in entry 1& 2, the use of solvent is reported [7,8]. While in entry 2 & 3 [7, 9] the reactions are performed at comparatively higher temperatures (>100 °C). Also, it should be noted that in all processes (Entry 1, 2 & 3), a higher catalyst amount is required for the reaction. Therefore, it is important to note that the reported catalysts show activity at comparatively harsher conditions. In contrast, the present catalyst proves to works effectively (97% conversion) at a lower temperature (90 °C), using low catalyst amount and without solvent. Thus, the process is greener and sustainable from the viewpoint of environmental and economic challenges.

3.10. Probable mechanism

The probable mechanism of esterification reaction between succinic acid and n-butanol is shown in Fig. 9. Here we assume that both Brønsted as well as the Lewis acidity contributes towards the catalytic activity. However, Brønsted acidity is responsible for diester formation. We also assume that formation of both the esters, mono and diester, follows the same reaction mechanism depending on the competitive adsorption of alcohol and the acidity of the catalyst. At first, the carboxylic acid gets adsorbed and activated by the Brønsted or Lewis acid sites present in zeolite, it forms a protonated intermediate (electrophile). The alcohol acts as a nucleophile and attacks the activated carbonyl

carbon, forming a tetrahedral intermediate. On losing a water molecule, the intermediate forms monobutyl succinate (monoester) followed by its desorption. The monoester undergoes the same path to give dibutyl succinate (diester) [9]. With the availability of more Brønsted acidic sites in the case of SiW_{12}-MCM-22, more carboxylic acid groups can be activated and hence the conversion and diester formation is higher. While in case of support (MCM-22), due to the availability of relatively fewer acid sites (weak Lewis acid sites) and higher surface area, there may be competitive adsorption of alcohol and it may restrict the acid adsorption [30]. Thus, single esterification predominates giving less conversion and yielding higher % of monoester.

4. Conclusion

Successful synthesis and detailed characterization of SiW_{12} modified MCM-22 was carried out. The acidity measurement by potentiometric titration proves the acidic nature of the catalyst, while the BET surface area analysis and FT-IR depict that SiW_{12} is well impregnated onto the MCM-22 support. The interaction of SiW_{12} with the MCM-22 was established by ^{29}Si MAS NMR analysis. TEM and Powder XRD analysis confirm the intact morphology and well dispersion of SiW_{12}. The catalyst showed appreciable catalytic activity in the esterification of bio-platform, succinic acid and n-butanol with >95% conversion and higher selectivity of diester with a good statistic of TON 1214. The activation energy (68 kJmol$^{-1)}$ suggests that a true chemical step governs the reaction. Control experiments showed up that the addition of Brønsted acidic sites of SiW_{12} to MCM-22, bring out almost complete conversion of acid and stimulates diester formation, while the presence of fewer acid sites in alone MCM-22 has a major role to play in the selectivity of monoester. The catalyst also gives appreciable activity with the range of alcohols and acids, proving its highly versatile nature. Furthermore, the greenness of the reaction was determined by green metrics (atom economy = 86.47% and E-factor = 0.69). The catalyst was regenerated and reused for the subsequent three cycles and characterized, indicating its excellent stability and intact structure. The superior activity of the present catalyst lies in the fact that excellent activity is achieved at mild conditions and the process is relatively green and sustainable as compared to that of the reported ones. The method also establishes the High Gravity approach. Selectively either of the two esters can be prepared by tuning the acidic sites (by increasing or decreasing acid sites) of the catalyst, i.e., selecting the appropriate amount of Brønsted acidity (SiW_{12}) to be introduced into the support and the reaction parameters.

CRediT authorship contribution statement

Dhruvi Pithadia: Methodology, Validation, Formal analysis, Investigation, Writing – original draft. **Anjali Patel:** Conceptualization, Validation, Writing – review & editing, Visualization, Supervision.

Declaration of competing interest

There are no conflicts to declare.

Acknowledgement

We are thankful to the Department of Chemistry, The Maharaja Sayajirao University of Baroda, for BET surface area analysis.

Appendix A. Supplementary data

Supplementary data to this article can be found online at https://doi.org/10.1016/j.biombioe.2021.106178.

Funding

This research did not receive any specific grant from funding agencies in the public, commercial, or not-for-profit sectors.

References

[1] J.C. Serrano-Ruiz, R. Luque, A. Sepúlveda-Escribano, Transformations of biomass-derived platform molecules: from high added-value chemicals to fuels via aqueous-phase processing, Chem. Soc. Rev. 40 (2011) 5266–5281, https://doi.org/10.1039/c1cs15131b.
[2] A.M. Raspolli Galletti, C. Antonetti, S. Fulignati, D. Licursi, Direct alcoholysis of carbohydrate precursors and real cellulosic biomasses to alkyl levulinates: a critical review, Catalysts 10 (2020) 1–2, https://doi.org/10.3390/catal10101221.
[3] C. Antonetti, D. Licursi, S. Fulignati, G. Valentini, A.M.R. Galletti, New frontiers in the catalytic synthesis of levulinic acid: from sugars to raw and waste biomass as starting feedstock, Catalysts 6 (2016) 1–29, https://doi.org/10.3390/catal6120196.
[4] T. Werpy, G. Petersen, Top Value Added Chemicals from Biomass: Volume I – Results of Screening for Potential Candidates from Sugars and Synthesis Gas, 2004, https://doi.org/10.2172/15008859. United States.
[5] J.J. Bozell, G.R. Petersen, Technology development for the production of biobased products from biorefinery carbohydrates—the US Department of Energy's "Top 10" revisited, Green Chem. 12 (2010) 539–554, https://doi.org/10.1039/B922014C.
[6] R.W. Jenkins, M. Munro, S. Nash, C.J. Chuck, Potential renewable oxygenated biofuels for the aviation and road transport sectors, Fuel 103 (2013) 593–599.
[7] A.L. Lown, L. Peereboom, S.A. Mueller, J.E. Anderson, D.J. Miller, C.T. Lira, Cold flow properties for blends of biofuels with diesel and jet fuels, Fuel 117 (2014) 544–551, https://doi.org/10.1016/j.fuel.2013.09.067.
[8] R. Fareghi-Alamdari, M.N. Niri, H. Hazarkhani, A novel hydrogen-bonded silica-supported acidic ionic liquid: an efficient, recyclable and selective heterogeneous catalyst for the synthesis of diesters, J. Chem. Sci. 130 (2018) 48, https://doi.org/10.1007/s12039-018-1454-z.
[9] C. Jing, L. Jinhua, D. Zhongxie, W. Yuehua, L. Zhen, J. Min, R. Xiaoqian, LEWIS ACID SITES OF Mg2+-MODIFIED POLYSTYRENE SULFONIC ACID RESIN CATALYSYS FOR SYNTHESIS OF DIBUTYL SUCCINATE, Química Nova . 41 (2018) 613–618.
[10] A. Szelwicka, S. Boncel, S. Jurczyk, A. Chrobok, Exceptionally active and reusable nanobiocatalyst comprising lipase non-covalently immobilized on multi-wall carbon nanotubes for the synthesis of diester plasticizers, Appl. Catal. Gen. 574 (2019) 41–47, https://doi.org/10.1016/j.apcata.2019.01.030.
[11] Y. Leng, P. Jiang, J. Wang, A novel Brønsted acidic heteropolyanion-based polymeric hybrid catalyst for esterification, Catal. Commun. 25 (2012) 41–44, https://doi.org/10.1016/j.catcom.2012.04.014.
[12] V. Brahmkhatri, A. Patel, Synthesis and characterization of 12-tungstosilicic acid anchored to MCM-41 as well as its use as environmentally Benign catalyst for synthesis of succinate and malonate diesters, Ind. Eng. Chem. Res. 50 (2011) 13693–13702, https://doi.org/10.1021/ie201447y.
[13] V. Brahmkhatri, A. Patel, An efficient green catalyst comprising 12-tungstophosphoric acid and MCM-41: synthesis characterization and diesterification of succinic acid, a potential bio-platform molecule, Green Chem. Lett. Rev. 5 (2012) 161–171, https://doi.org/10.1080/17518253.2011.607471.
[14] V. Brahmkhatri, A. Patel, Esterification of bioplatform molecules over 12-tungstophosphoric acid anchored to MCM-41, J. Porous Mater. 20 (2013) 209–217, https://doi.org/10.1007/s10934-012-9590-1.
[15] I. Kozhevnikov, Catalysts for Fine Chemical Synthesis, Catalysis by Polyoxometalates, Wiley, 2002. https://books.google.co.in/books?id=jaTXrZyGSuAC.
[16] I. v Kozhevnikov, Catalysis by heteropoly acids and multicomponent polyoxometalates in liquid-phase reactions, Chem. Rev. 98 (1998) 171–198, https://doi.org/10.1021/cr960400y.
[17] M. Misono, Characterization of acidic properties of heteropoly compounds in relation to heterogeneous Catalysis, in: B. Imelik, C. Naccache, G. Coudurier, Y. ben Taarit, C. Vedrine (Eds.), Catalysis by Acids and Bases, Elsevier, 1985, pp. 147–156, https://doi.org/10.1016/S0167-2991(09)60164-6.
[18] T. Okuhara, N. Mizuno, M. Misono, in: D.D. Eley, W.O. Haag, B.B.T. A, C. Gates (Eds.), Catalytic Chemistry of Heteropoly Compounds, Academic Press, 1996, pp. 113–252, https://doi.org/10.1016/S0360-0564(08)60041-3.
[19] B. Zhang, Z. Wang, P. Ji, Y. Liu, H. Sun, W. Yang, P. Wu, Efficient liquid-phase ethylation of benzene with ethylene over mesoporous MCM-22 catalyst, Microporous Mesoporous Mater. 179 (2013) 63–68, https://doi.org/10.1016/j.micromeso.2013.05.004.
[20] D. Pithadia, V. Hegde, V.P. Brahmkhatri, A. Patel, New catalyst comprising Silicotungstic acid and MCM-22 for degradation of some organic dyes, Environ. Sci. Pollut. Control Ser. (2020), https://doi.org/10.1007/s11356-020-11340-8.
[21] A. Patel, D. Pithadia, Low temperature synthesis of bio-fuel additives via valorisation of glycerol with benzaldehyde as well as furfural over a novel sustainable catalyst, 12-tungstosilicic acid anchored to ordered cubic nano-porous MCM-48, Appl. Catal. Gen. 602 (2020) 117729, https://doi.org/10.1016/j.apcata.2020.117729.
[22] P. Ferreira, I.M. Fonseca, A.M. Ramos, J. Vital, J.E. Castanheiro, Valorisation of glycerol by condensation with acetone over silica-included heteropolyacids, Appl. Catal. B Environ. 98 (2010) 94–99, https://doi.org/10.1016/j.apcatb.2010.05.018.
[23] Y. Cheng, X.Y. Su, M. Lu, Preparation and characterization of MCM-22 zeolite by varying-temperature hydrothermal synthesis, Adv. Mater. Res. 197–198 (2011) 1587–1590. https://doi.org/10.4028/www.scientific.net/AMR.197-198.1587.
[24] M.C. Lonare, S.N. Gaikwad, C. Lonare, R.G. Pala, S. Siva, P. Kapse, Zeolite Coated Gold Nano Particles - A Versatile Nano Catalyst, vol. 5 (n.d.) 192–214.

[25] F. Schüth, M.D. Ward, J.M. Buriak, Common pitfalls of Catalysis manuscripts submitted to chemistry of materials, Chem. Mater. 30 (2018) 3599–3600, https://doi.org/10.1021/acs.chemmater.8b01831.
[26] C. Antonetti, S. Gori, D. Licursi, G. Pasini, S. Frigo, M. López, J.C. Parajó, A.M. R. Galletti, One-pot alcoholysis of the lignocellulosic eucalyptus nitens biomass to n-butyl levulinate, a valuable additive for diesel motor fuel, Catalysts 10 (2020) 1–22, https://doi.org/10.3390/catal10050509.
[27] C. Xiros, M. Janssen, R. Byström, B.T. Børresen, D. Cannella, H. Jørgensen, R. Koppram, C. Larsson, L. Olsson, A.M. Tillman, S. Wännström, Toward a sustainable biorefinery using high-gravity technology, Biofuels, Bioproducts and Biorefining 11 (2017) 15–27, https://doi.org/10.1002/bbb.1722.
[28] G.C. (Geoffrey C. Bond, Heterogeneous Catalysis : Principles and Applications/G.C. Bond, Clarendon Press, Oxford [Oxfordshire] ; New York, 1987.
[29] T.-C. Huang, J. Wan, L.-H. Tsai, Kinetic studies on the esterification of acid and alcohol in the presence of dowex 50W and of sulfuric acid, J. Chin. Chem. Soc. 14 (1967) 72–86, https://doi.org/10.1002/jccs.196700010.
[30] S.R. Kirumakki, N. Nagaraju, K.V.R. Chary, Esterification of alcohols with acetic acid over zeolites Hβ, HY and HZSM5, Appl. Catal. Gen. 299 (2006) 185–192, https://doi.org/10.1016/j.apcata.2005.10.033.

Renewable Energy 187 (2022) 933–943

Contents lists available at ScienceDirect

Renewable Energy

journal homepage: www.elsevier.com/locate/renene

12-Tungstophosphoric acid anchored to MCM-22, as a novel sustainable catalyst for the synthesis of potential biodiesel blend, levulinate ester

Dhruvi Pithadia , Anjali Patel *, Vijay Hatiya

Polyoxometalates and Catalysis Laboratory, Department of Chemistry, Faculty of Science, The Maharaja Sayajirao University of Baroda, Vadodara, 390002, Gujarat, India

ARTICLE INFO

Article history:
Received 31 August 2021
Received in revised form
20 January 2022
Accepted 25 January 2022
Available online 3 February 2022

Keywords:
12-Tungstophosphoric acid
Zeotype MCM-22
Esterification
Levulinate esters
Biodiesel blend

ABSTRACT

The present article demonstrates a synthesis of a green, novel and sustainable heterogeneous catalyst comprising 12-tungstophosphoric acid and zeolitic support- MCM-22. Detailed characterization of the catalyst was carried out using various physicochemical techniques and its catalytic activity was explored for the production of butyl levulinate, a potential fuel blend candidate. The comparison with other phosphotungstate based catalysts showcases the outstanding activity of the present catalyst towards esterification of levulinic acid at 90 °C with 68% conversion, 99% ester selectivity and TOF of 212 h^{-1}. Furthermore, it exhibits excellent reusability for multiple catalytic runs (six runs) and illustrates feasibility for the synthesis of varied levulinate esters (65–78% conversion) having a range of carbon chain lengths (C3–C8).

© 2022 Elsevier Ltd. All rights reserved.

1. Introduction

In this era of high energy demand, catalytic processes for upgrading renewable biomass feedstock have gained tremendous attention. This emerging research across the globe is driven by the rising shortage of fossil fuels, concerns regarding global warming and the upsurge in oil charges. Henceforth this challenging task can be addressed by replacing the non-renewable fossils with renewable biomass and inventing excellent sustainable technologies for the production of valuable chemicals, fuels and energy from non-edible feedstock and judiciously selected bio-platforms, thus thereby building a base for future bio-based refineries [1].

Presently, the transportation sector consumes approximately one-third of the total energy produced globally and the demand for transportation fuels is satiated by oil reserves. Hence, depleting reserves has led to alternative sources, mainly, utilization of hydrocarbon fuels that can be derived from biomass. In this direction, lignocellulosic biomass holds the immense potential of generating bio-based petroleum products via a down streaming process of its three polymeric components: cellulose, hemicellulose and lignin [2]. The fractions obtained from these components can be converted to biofuels via some important intermediates, for instance, furfural, 5-HMF, levulinic acid and ɣ-valerolactone [3,4].

Looking to the future demand of renewable energy production, levulinic acid, an important intermediate and originally bio-derived molecule was selected as a model bioplatform that leads to ample valuable products. It holds an immense potential to generate biofuels, additives and value-added products such as alkyl levulinates, lactones, ɣ-valerolactone, ketals, pyrrolidines, succinic acid, etc. [5,6].

In this context, alkyl levulinates are of particular interest due to their specific physicochemical property and find role in several applications including fuel additives, pharmaceutical agents, resin precursors, fragrance and flavouring agents. Particularly, they are more suitable as fuel blends in terms of having excellent lubricity, balanced flow property, low toxicity and constant flashpoint [7–10]. It is worthy to note that butyl levulinate has been proved to be more encouraging as a fuel additive compared to widely applicable ethyl levulinate due to its lower miscibility in water and it is persistent with diesel even at the diesel cloud point [11].

Hence, several catalytic systems, such as organic-inorganic hybrid catalysts [12], modified silica [9,13,14], mesoporous

* Corresponding author.
E-mail addresses: dhruvi.pithadia@gmail.com (D. Pithadia), anjali.patel-chem@msubaroda.ac.in (A. Patel), vijayhatiya@gmail.com (V. Hatiya).

https://doi.org/10.1016/j.renene.2022.01.106
0960-1481/© 2022 Elsevier Ltd. All rights reserved.

materials [15–17], enzymes [18,19], titania nanotubes [20,21], carbonaceous solid acid [22], graphene oxide [23], zeolites [24,25], modified clays [26], metal-organic frameworks [11], ion-exchange resins [27] as well as supported/modified heteropolyacids (HPAs) [28–32] have been reported for the synthesis of butyl levulinate. In 2016, Zheng et al. reported the use of 12-tungstosilicic acid immobilized on MCM-41 for butyl levulinate synthesis and obtained approximately 87% conversion at 70 °C in 10 h [28]. In the same year, Zhou et al. described ammonium and silver co-doped 12-tungstophosphoric acid for the synthesis of butyl levulinate and obtained 99 and 92% ester respectively at 120 °C in 2 h [29]. Another catalyst, 12-tungstophosphoric acid supported on silicalite-1 zeolite was reported by Cheralathan et al. in 2017, and they achieved 93% butyl levulinate at 100 °C in 5 h [30]. Gong et al. (in 2018) described the synthesis of butyl levulinate (96.5%), by using an organic salt of 12-tungstosilicic acid and quinaldic acid, at reflux temperature for 5 h [31]. Lately, in 2019, Pizzio et al. reported nano core-shell magnetic composite based on 12-tungstophosphoric acid and obtained 100% yield of butyl levulinate at 80 °C in 5 h [32].

A literature survey shows, (i) few reports are available on the esterification of levulinic acid to butyl levulinate over supported/modified HPAs and (ii) Zeotype support, MCM-22, has not at all been used for the synthesis of biofuel additives. So, it was thought to make use of MCM-22 as support for anchoring HPA, 12-tungstophosphoric acid, and to explore its catalytic activity towards the synthesis of levulinate esters.

In the present article, first time, we are reporting the synthesis of a novel catalyst, 12-tungstophosphoric acid (PW_{12}) anchored to MCM-22 by the incipient wet impregnation method. Detailed characterization of the catalyst was carried out by various physicochemical techniques and complete optimization study for a model reaction, esterification of the most important bio-platform molecule, levulinic acid, with 1-butanol was carried out by varying different reaction parameters. The catalyst was recovered, reused for consecutive multiple catalytic cycles and a probable reaction mechanism has been proposed. Furthermore, its versatility for esterification of other bio-derived acids and alcohols with different chain lengths (C3–C8) has also been explored. The catalytic efficiency has finally been compared with the other reported catalysts to show the superiority of the present catalyst.

2. Experimental

2.1. Materials and solvents

MCM-22 was procured ready-made from BEE CHEMS (Kanpur, UP). 12-tungstophosphoric acid (extra pure), levulinic acid (>98%), succinic acid (99.5%), fumaric acid (99.5%), 1-butanol (>98%), 2-propanol (>99%), isobutanol (>99%), 1-pentanol (>99%), 1-hexanol (>99%), 1-octanol (>99%) and dichloromethane (>99%) were used as received from Merck. Maleic acid (98%) was received from Avra Synthesis Pvt. Ltd. (Telangana, India).

2.2. Catalyst synthesis: 12-tungstophosphoric acid (PW_{12}) anchored to MCM-22

Synthesis of a series of catalysts comprising 10–40% of PW_{12} was carried out by the incipient wet impregnation method. 1 g of MCM-22 was suspended in an aqueous solution of PW_{12} (0.1 g/10 mL to 0.4/40 mL in double distilled water). The solvent was evaporated and dried at 100 °C for 10 h and the obtained catalysts were designated as $(PW_{12})_1$/MCM-22, $(PW_{12})_2$/MCM-22, $(PW_{12})_3$/MCM-22 and $(PW_{12})_4$/MCM-22, respectively.

2.3. Characterizations

2.3.1. Acidity measurements

a. **Potentiometric titration.** The acidity of support, as well as catalysts, were measured in terms of acidic strength and sites by performing potentiometric titrations as reported in the literature [33]. Suspension of 0.25 g of support/catalyst in 25 mL acetonitrile (ACN) was prepared. In this suspension, 0.1 mL of 0.05 N n-butylamine solution in ACN was added and allowed to stir for 3 h at 25 °C. After that, the suspension was titrated against the same n-butylamine solution and the difference in the values of potential was measured by the digital pH meter. The acid strength of surface sites was designated according to the given scale: Ei > 100 mV (very strong sites), 0 < Ei < 100 mV (strong sites), −100 < Ei < 0 mV (weak sites) and Ei < −100 mV (very weak sites).
b. **Pyridine adsorption FT-IR.** The types of the acidic sites were determined by performing pyridine adsorbed FT-IR of the support and catalyst. An excess amount of pyridine in dichloromethane was allowed to adsorb on the support/catalyst for 1 h and the solvent was evaporated at 50 °C. The spectra were recorded on a Shimadzu instrument (IRAffinity-1S) using self-supported pellets of 10 mg sample.

2.3.2. Physicochemical techniques

The BET (Brunauer–Emmett–Teller) surface area measurements were performed on Micromeritics ASAP 2010 (USA) volumetric static adsorption instrument with N_2 adsorption at 77 K and the calculations of pore size distributions were done using the BJH adsorption-desorption method. Elemental analysis was performed using JSM-7100F (Model) EDX-SEM analyser (JAPAN). Thermogravimetric analysis (TGA) was performed under nitrogen atmosphere with a flow rate of 2 mL min^{-1} at 25–600 °C (ramp rate of 10 °C min^{-1}) using Mettler Toledo Star SW 7.01 (Model) (SWITZERLAND). The Fourier Transform Infrared (FT-IR) spectra were recorded with KBr disc on Shimadzu instrument (IRAffinity-1S) (JAPAN), in the range 4000–400 cm^{-1}. The ^{29}Si Magic angle spinning- Nuclear magnetic resonance (MAS-NMR) spectra were recorded on JOEL ECX 400 MHz (Model) (JAPAN) High resolution multinuclear FT-NMR spectrometer. X-ray powder diffraction (XRD) patterns for the samples were analysed in the 2θ range 5 - 90° (CuKα radiation λ = 1.54056 Å) using Philips PW-1830 instrument (Model). The Scanning electron microscope (SEM) images were recorded on Model- JSM-7100F scanning electron microscope. Transmission electron microscopy (TEM) was done by coating the samples on the Cu grid and scanned on a JEOL TEM instrument (model-JEM 2100) (JAPAN) with an acceleration voltage of 200 kV using carbon-coated 200 mesh.

2.4. Catalytic activity: esterification of levulinic acid with 1-butanol

In a typical reaction procedure, levulinic acid (10 mmol), 1-butanol (20 mmol) and the required amount of catalyst were charged in a 50 mL batch reactor equipped with an air condenser and guard tube. The reaction was allowed to proceed at the desired temperature and after completion, the contents of the reaction mixture were gradually cooled at room temperature and diluted using 7–10 mL dichloromethane. The diluted contents were analysed using gas chromatography, Shimadzu 2014 GC equipped with RTX-5 capillary column (internal diameter: 0.25 mm, length: 30 m). The schematic representation for the catalytic methodology is presented in Fig. 1.

The products were identified using GC–MS (Gas chromatography-mass spectrometry Thermo scientific DSQ-II;

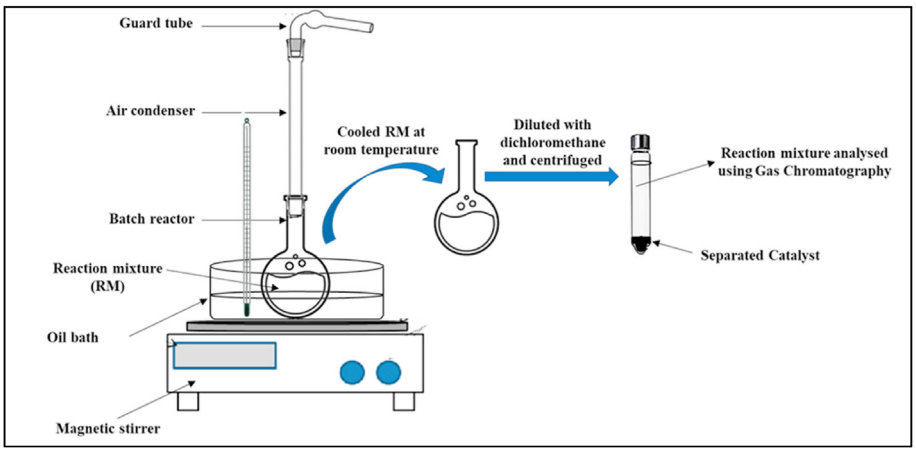

Fig. 1. Schematic representation for the catalytic methodology.

Capillary column- Thermo TR-MS). Development of a new catalytic process was performed by varying different reaction parameters such as % loading of PW_{12}, mole ratio of reactants, catalyst amount, reaction temperature and time. An overall schematic representation is shown in Fig. 2.

3. Results & discussion

3.1. Catalyst characterization

The BET surface area measurements of support, as well as catalysts, are presented in Table 1. As the loading of PW_{12} increases, the surface area compared to MCM-22 decreases, the first indication of interaction as well as successful encapsulation of PW_{12} inside MCM-22. It is also supported by the drastic reduction in the pore diameter and volume, with an increase in PW_{12} loading. However, it is interesting to note down that when the % loading increased from 30 to 40%, nearly the same surface area for $(PW_{12})_4$/MCM-22 was observed. This may be due to the blocking of sites or surface saturation of support after 30% loading. Considering the maximum incorporation of PW_{12}, 30% loading was optimized, and further supported by acidity measurements.

The nitrogen adsorption-desorption isotherms of MCM-22 and PW_{12}/MCM-22 are depicted in Fig. 3. MCM-22 exhibits type IV isotherm with H4 hysteresis loop, a typical isotherm of zeolites, showcasing meso and microporous framework [34]. The catalyst, PW_{12}/MCM-22 shows an identical isotherm, confirming the intact structure of support. A decline in the quantity of adsorption and a narrow hysteresis loop indicates the effective filling of PW_{12} inside the porous framework of MCM-22.

The acidic properties of support and catalysts were determined by the potentiometric titration method [33]. The measured electrode potential as a function of mEqui. n-butylamine per g of the support/catalysts are depicted in electronic supplementary information S1 and the acidic strength, as well as sites, are tabulated in Table 2. MCM-22 shows the acidic strength of 132 mV with the total acidic sites of 1.4 mEqui g^{-1}. The acidic strength and sites tremendously increase with the loading from 10 to 30%, due to the enhancement of Bronsted acidity present in PW_{12}. However, a negligible difference is observed for 30 and 40% loaded catalysts which may be attributed to the blocking of the sites. Thus, 30% loading is optimized, for simplicity, it is redesignated as PW_{12}/MCM-22 and detailed characterizations were carried out for the same.

To support the above observations, pyridine adsorbed FT-IR of support and catalyst was carried out (Fig. 4). Both the spectra show the appearance of bands at 1543 and at 1635 cm^{-1} which corresponds to the pyridinium ions (PyrH+) formed by Bronsted acid sites (B). The Lewis sites (L) coordinated by (PyrL), appears at 1443 and 1600 cm^{-1}. Also, a distinct band at 1489 cm^{-1} was observed for the combined B + L sites coordinated by Pyridine [35]. Interestingly, for the catalyst, the intensity of bands corresponding to PyrH + increases significantly and thus imparting an impression of an increase in the Bronsted acid sites. A similar increase was also found for the combined band of B + L sites at 1489 cm^{-1}. It is interesting to note down that as PW_{12} contains Bronsted acid sites, incorporation of it into the support increases the Bronsted acid sites and hence relatively there will be decrease in the Lewis acid sites.

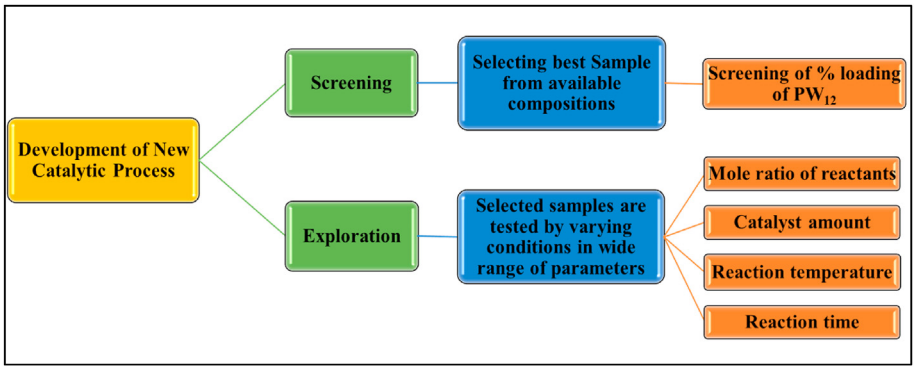

Fig. 2. Schematic representation of development of new catalytic process.

Table 1
Textural properties of support and catalysts.

Support/Catalysts	BET Surface area (m^2/g)	Pore diameter (Å)	Pore volume (cm^3/g)
MCM-22	344	102.4	0.79
$(PW_{12})_1$/MCM-22	321	59.5	0.3
$(PW_{12})_2$/MCM-22	286	54.9	0.29
$(PW_{12})_3$/MCM-22	258	53.1	0.25
$(PW_{12})_4$/MCM-22	256	52	0.27

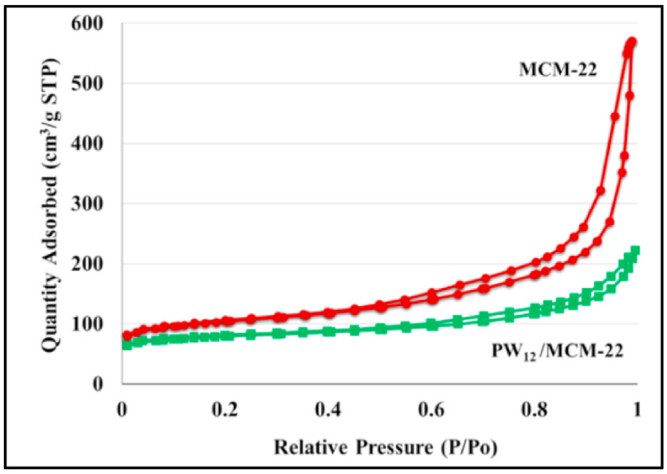

Fig. 3. Nitrogen sorption isotherms of MCM-22 and PW_{12}/MCM-22.

Thus, this study confirms the increase in the Bronsted acidity by the introduction of PW_{12} into MCM-22.

Elemental analysis shows the presence of all expected elements (Supplementary Information Fig. S2). The values for P and W (Table 3), obtained for the catalyst are in good accord with that of the theoretical ones, indicating effective loading of PW_{12}.

The TGA curves of MCM-22 and PW_{12}/MCM-22 are shown in the electronic supplementary information, Fig. S3. MCM-22 loses weight with an increase in temperature in two stages. In the first stage, up to 130–135 °C, weight loss of approximately 4.7% was observed which corresponds to the loss of physically adsorbed water molecules. Above 200 °C, a weight loss of 2.5% was obtained which may be attributed to the remaining template decomposition [36]. For PW_{12}/MCM-22, a relatively greater amount of initial weight loss (8.1%) up to 178 °C was observed due to the adsorbed water present in both the support and keggin unit (PW_{12}). Additionally, a gradual weight loss in the range of 205–307 °C was seen corresponding to the crystalline water of PW_{12}. With no further loss, the support, as well as the catalyst, are stable at higher temperatures (550–600 °C).

FT-IR spectra of MCM-22 (Fig. 5b) shows typical bands at 3441 cm^{-1}, 1226 cm^{-1}, 817 cm^{-1} and 455 cm^{-1}, corresponding to the O–H stretching asymmetric and symmetric stretching of T-O-T

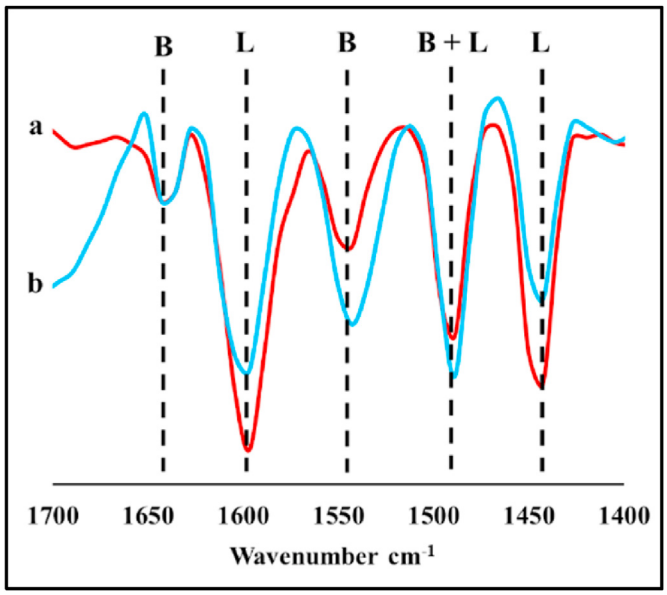

Fig. 4. Pyridine adsorbed FT-IR of (a) MCM-22 and (b) PW_{12}/MCM-22.

bond where T = Si or Al and stretching vibration of T-O bond, respectively [37]. The FT-IR spectra of catalyst (PW_{12}/MCM-22) (Fig. 5c) show an additional band at 925 cm^{-1}, one of the characteristic bands for the Keggin unit of PW_{12} corresponding to asymmetric vibration of Si-Oa. However, the other bands are not distinct due to the superimposition with that of support. The presence of this fingerprint band suggests that the primary structure of Keggin unit is intact even after impregnation on the support.

To confirm the interactions between PW_{12} and MCM-22, ^{29}Si MAS NMR of support and catalysts were performed. As depicted in Fig. 6a, the NMR spectra of MCM-22 displays characteristic peaks at −99.34 and a bunch of peaks from −102 to −118 ppm corresponding to the Si (1Al) and Si (0Al) respectively. In the case of PW_{12}/MCM-22 (Fig. 6b), the first peak corresponding to Si (1Al) shifts to −107.63 ppm due to changes in the surrounding environment of Si atoms. Interestingly, there is a significant increase in the intensities as well as shifting of a group of peaks (−108 to −121 ppm) relative to MCM-22, which corresponds to Si (0 Al) and this exciting change can be attributed to the strong interactions of PW_{12} with that of the MCM-22 framework.

XRD patterns of support and catalyst are depicted in Fig. 7. Both MCM-22 and PW_{12}/MCM-22 shows all the characteristic peaks of zeolitic structure in the range of 2θ 5-30° [38]. After loading PW_{12}, all the crystalline peaks of the support remain altered, suggesting its intact framework. Nevertheless, a little decrease in the intensity of the peaks can be spotted for the catalyst which may be due to the presence of PW_{12} inside MCM-22. Furthermore, it is also important to note that the distinct crystalline peaks for PW_{12} are not observed indicating a well distribution of it into the porous framework [39] which is further confirmed by SEM and TEM.

Table 2
Acidic properties of support/catalysts by potentiometric titration method.

Support/Catalysts	Acidic strength (mV)	Types of acidic sites (mEqui g^{-1})			Total No. of acidic sites (mEqui g^{-1})
		Very strong	Strong	Weak	
MCM-22	132	0.2	1.2	–	1.4
$(PW_{12})_1$/MCM-22	210	0.2	0.5	2.1	2.7
$(PW_{12})_2$/MCM-22	260	0.6	1.1	2.4	4.1
$(PW_{12})_3$/MCM-22	473	1.2	1.6	2.3	5.1
$(PW_{12})_4$/MCM-22	480	1.7	1.0	2.6	5.3

Table 3
Elemental analysis of Support and Catalyst.

Support/Catalyst	Si (wt%)	Al (wt%)	O (wt%)	P (wt%)		W (wt%)	
				By EDX	Theoretical	By EDX	Theoretical
MCM-22	31.35	19.38	49.27	–	–	–	–
PW_{12}/MCM-22	17.15	10.98	53.96	0.24	0.25	17.68	17.56

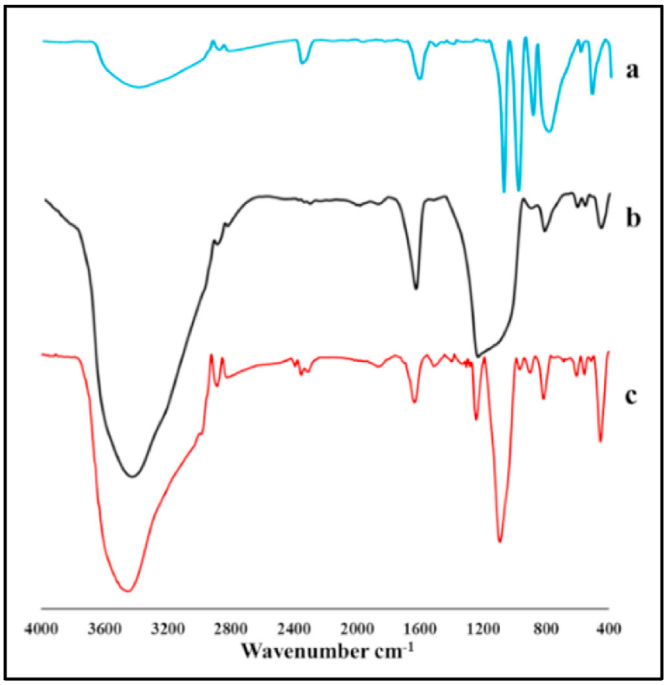

Fig. 5. FT-IR spectra of a) PW_{12}, b) MCM-22 & c) PW_{12}/MCM-22.

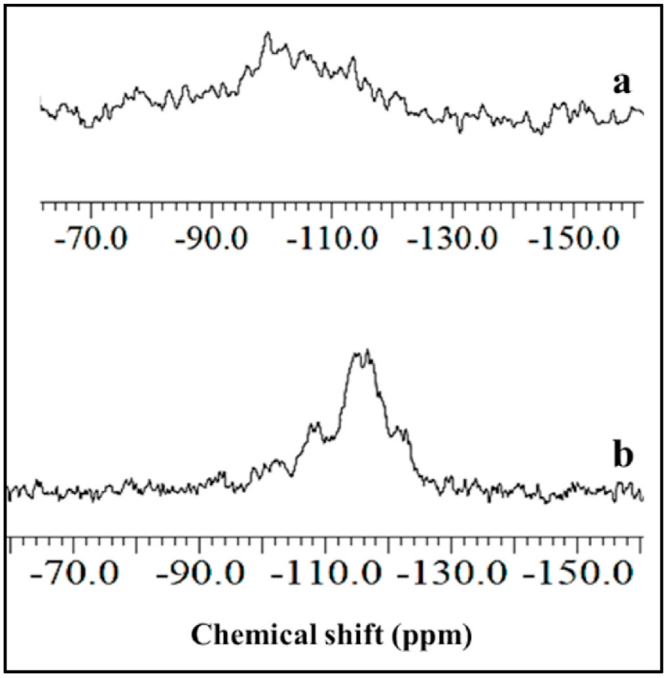

Fig. 6. ^{29}Si MAS-NMR of a) MCM-22 & b) PW_{12}/MCM-22.

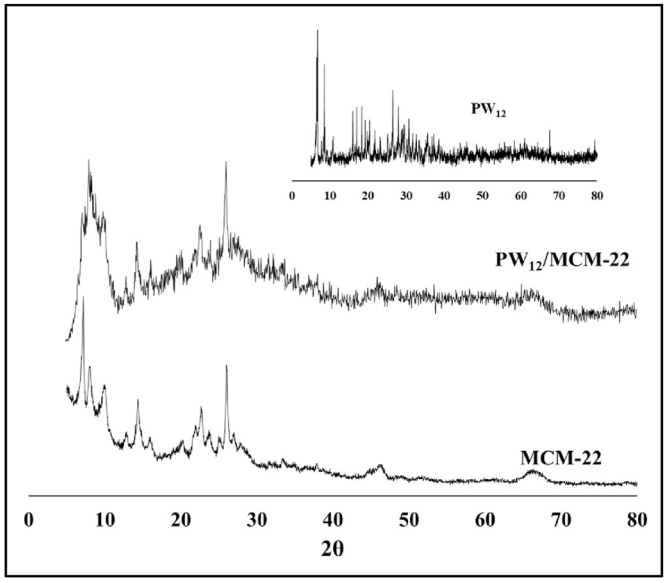

Fig. 7. XRD pattern for support and catalyst.

From SEM images of MCM-22 (Fig. 8a and b), the morphology shows an arrangement of lamellar particles which are formed by the interpenetrating network of thin platelets. After anchoring PW_{12}, Fig. 8c and d clearly shows the unchanged morphology of support and retain the lamellar structure. Likewise, fine and uniform dispersion of PW_{12} can be confirmed by the absence of aggregates formation.

TEM images of MCM-22 and PW_{12}/MCM-22 at different magnifications are presented in Fig. 9. MCM-22 (Fig. 9a, b, c) demonstrates the uniform channels with the high-resolution pore networks and evenly distributed growth of flaky crystals [36]. By anchoring PW_{12}, the translucent pore networks of MCM-22 seem to turn obscure which suggests the uniform dispersion and filling of PW_{12} inside the porous MCM-22 (Fig. 9d, e, f).

3.2. Catalytic performance

The catalyst, PW_{12}/MCM-22, was tested for levulinic acid esterification with 1-butanol (Scheme 1) by varying all reaction parameters (% loading of PW_{12}, stoichiometry of reactants, catalyst amount, reaction temperature and time) to optimize conditions for maximum selectivity of butyl levulinate.

Primarily, it is important to identify appropriate catalyst loading also from the viewpoint of catalytic activity. Experiments with different PW_{12} concentrations, 10–40% were carried out and it was found that the reaction proceeds forward as the amount of active catalytic acid sites increases with the % loading (Table 4). In 10% loading, 52% conversion with 92% selectivity of ester was obtained which hiked to 68% conversion and 99% ester selectivity in 30% loading. Further rise in the amount of PW_{12} from 30 to 40% does not

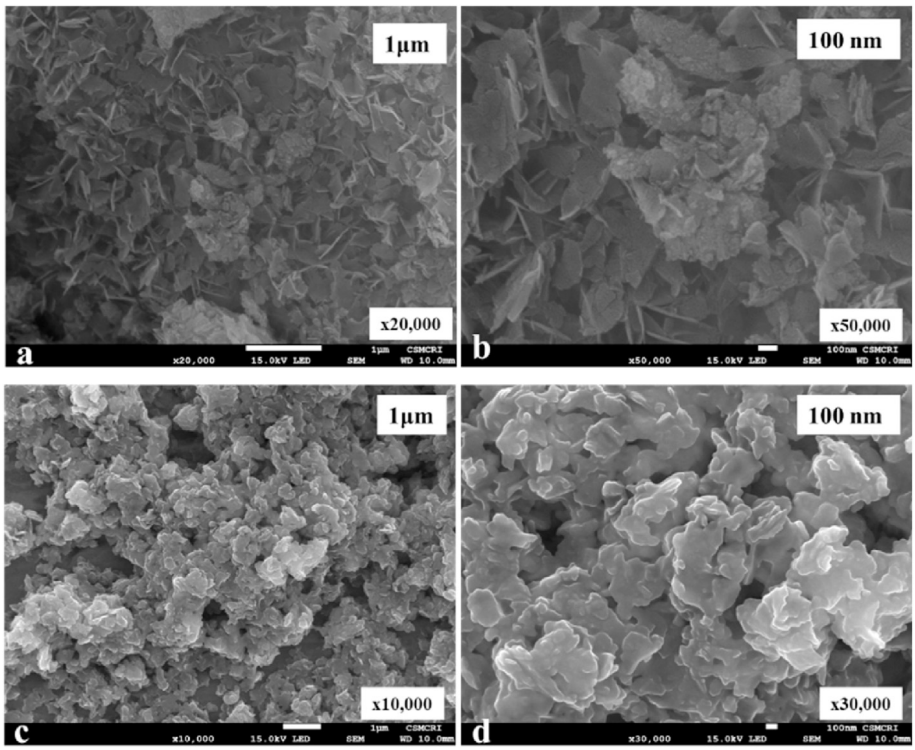

Fig. 8. SEM images a,b) MCM-22 & c,d) PW_{12}/MCM-22.

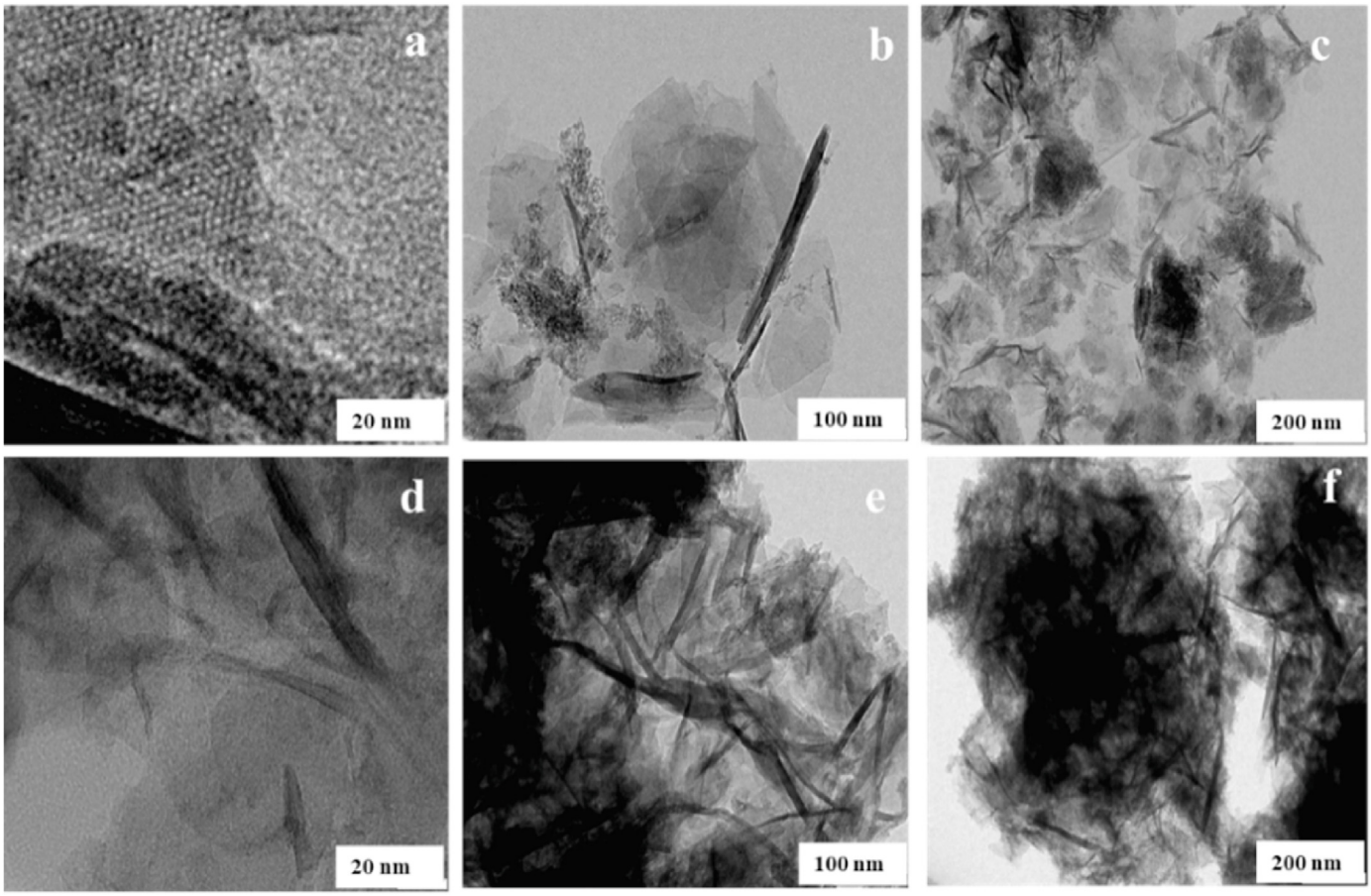

Fig. 9. TEM images a,b,c) MCM-22 & d,e,f) PW_{12}/MCM-22.

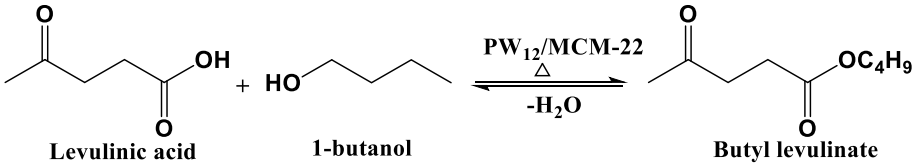

Scheme 1. Esterification of levulinic acid with 1-butanol.

Table 4
Effect of PW_{12} loading on levulinate ester synthesis.

Entry	% Loading (PW_{12})	% Conv[a]	% Sel[b]
1	10	52	92
2	20	55	92
3	30	68	99
4	40	70	98

Conditions: mole ratio: 1:2; catalyst amount: 1.86 wt%; temp: 90 °C; time: 8 h.
[a] % Conversion of levulinic acid.
[b] % selectivity of ester.

show any significant increase in activity, and almost similar % conversion, as well as ester selectivity, was obtained. This steady activity at higher concentrations may be attributed to the limitations of mass transfer and/or blocking of the sites due to viscous reaction mixture [10]. This unvarying behaviour can be correlated with the surface area and acidity measurements of 30 and 40% loaded MCM-22. Henceforth, the above experiments confirm that 30% loading of PW_{12} on MCM-22 is suitable for carrying out further catalytic reactions from the viewpoint of catalytic activity.

It is evident to understand and optimize the mole ratio of reactants to achieve utmost selectivity of the desired product and to limit the side reactions. Acid: alcohol mole ratio was varied from 1:1 to 1:3 and the results are plotted in Fig. 10a. Initially, conversion of levulinic acid increases from 1:1 to 1:2 mol ratio. As esterification reaction is a reversible reaction, a little excess of alcohol shifts the equilibrium to the forward direction and prevents reverse hydrolysis. Thus, in the 1:2 mol ratio, excess alcohol component increases the reaction rate relative to 1:1. However, when the rate increased to 1:3, the conversion of levulinic acid slightly decreases, which is probably due to the dilution of active reactant species. Thus, the 1:2 mol ratio was considered to be optimum. From the repeated catalytic runs, ±1.5–3% error was observed.

Experiments for screening of catalyst amount from 0.93 wt% (25 mg) to 2.79 wt% (75 mg) was performed keeping the other parameters constant (Fig. 10b). The conversion rate of acid increases from 56% to 68% using 0.93 wt% to 1.86 wt% (50 mg) of catalyst respectively. This follows the regular trend, as the amount increases to double, the availability of catalytic acid sites favours the rate of reaction, with no influence on the ester selectivity. Nonetheless, the amount beyond 1.86 wt% did not show any significant impact on the reaction rate, which may refer to the presence of additional catalytic sites than require. Therefore, 1.86 wt% of catalyst was found to be ideal and repeated runs showed ±1.2–2% statistical error.

The influence of reaction temperature has enormous importance in any process, especially for the endothermic reactions like levulinic acid esterification which shifts the equilibrium to a forward direction. For understanding its impact, experiments at 80, 90 and 100 °C were carried out and the results are plotted in Fig. 10c. At 80 °C, 55% conversion and 87% ester selectivity were obtained. Appreciably, increasing temperature to 90 and 100 °C gives 68 and 72% conversion with almost the same ester selectivity, respectively. As seen, an increase in the reaction temperature promotes the reaction rate as it increases the collisions between reactant molecules. Keeping in mind the industrial aspects, though a little bit of good conversion was observed for 100 °C, for this reaction 90 °C temperature was considered optimal as achieving higher temperature is also an energy-demanding process. An error of ±1.8–2% was observed from the repeated catalytic runs.

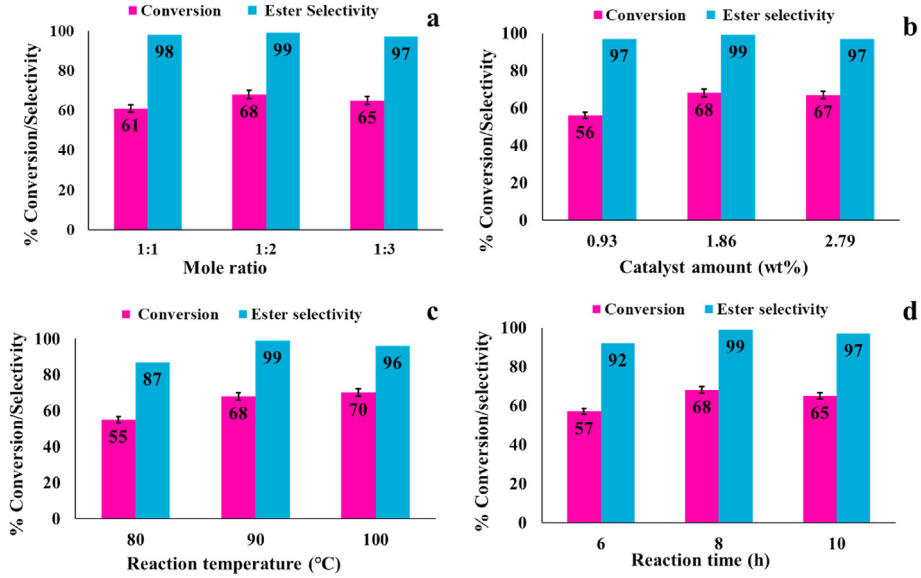

Fig. 10. (a) Effect of mole ratio. catalyst amount: 1.86 wt%; temperature: 90 °C; time: 8 h; (b) Effect of catalyst amount. mole ratio: 1:2; temperature 90 °C; time: 8 h; (c) Effect of temperature. mole ratio: 1:2; catalyst amount: 1.86 wt%; time: 8 h (d) Effect of time. mole ratio: 1:2; catalyst amount: 1.86 wt%; temperature: 90 °C.

Table 5
Control experiments for levulinic acid esterification.

Catalyst	% Conv[a]	% Sel[b]	TON/TOF h^{-1}
MCM-22[c]	24	100	NA
PW_{12}[d]	89	87	2227/278
PW_{12}/MCM-22[e]	68	99	1697/212

Conditions: mole ratio: 1:2; temp: 90 °C; time: 8 h; Catalyst amount.- c, d, e.
TOF = Moles of product/(Moles of catalyst x reaction time (h)). TON = Moles of product/Moles of catalyst.
[a] % Conversion of levulinic acid.
[b] Selectivity of ester.
[c] 38.46 mg.
[d] 11.54 mg (Active amount of PW_{12}).
[e] 50 mg (1.86 wt%).

Lastly, the effect of reaction time was checked by performing experiments for 6–10 h (Fig. 10d). Here also, the reaction proceeds forward from 57 to 68% conversion with 92–99% ester selectivity in 6–8 h respectively. However, beyond 8 h, the conversion slightly declines which may be due to the reverse hydrolysis of ester in the presence of water molecules generated during the reaction as a by-product. Thus, 8 h was considered an appropriate reaction time. Repeated runs for reaction time showed ±1.1–1.7% statistical error.

The optimized reaction parameters are; mole ratio (acid: alcohol) = 1:2; catalyst amount = 1.86 wt%, temperature = 90 °C; time = 8 h and maximum conversion of 68% with 99% ester selectivity was achieved with excellent TOF of 212 h^{-1}.

3.3. Control experiments

To study the role of each species of catalyst, control experiments using support alone as well as PW_{12} were carried out and the results are shown in Table 5. In MCM-22, the reaction proceeds to give only 24% conversion with 100% ester selectivity. While in the case of PW_{12}, homogeneous catalyst, 89% conversion was obtained with 87% selectivity of ester. The decrease in the selectivity of the ester may be attributed to the highly acidic nature of PW_{12} which also promotes other side reactions [32]. When the reaction was performed with catalyst (PW_{12}/MCM-22) lower conversion (68%) as compared to PW_{12} was obtained but here it is interesting to note that the selectivity of ester increased to 99%. This suggests that the higher acidity of PW_{12} plays a significant role in promoting the reaction in a forward direction while the selective formation of the ester may be attributed to the unique pore system of MCM-22 which favours the desired esterification pathway and may also prevent the mass transfer problems that are common in the said transformation [10]. Thus, an efficient heterogeneous catalyst comprising of active PW_{12} and MCM-22 works spectacularly in synergy for the synthesis of butyl levulinate.

3.4. Leaching & recycling studies

To check the sustainability of the synthesized heterogeneous catalyst, the leaching of PW_{12} species from MCM-22 was checked by following the procedure mentioned in our previous article [40]. When treated with ascorbic acid the supernatant liquid obtained from PW_{12}/MCM-22 (catalyst) shows an absence of heteropoly blue colour indicating no leaching or escaping of PW_{12} species from the support. A similar experiment was also performed with the reaction mass obtained after the reaction completion. Additionally, recycling studies for the catalyst were also performed. After the first run, the reaction mixture was simply centrifuged to separate the catalyst. The collected catalyst was washed with methanol, followed by water, dried at 100 °C and used for the next catalytic run. The catalyst shows appreciable activity up to six runs giving

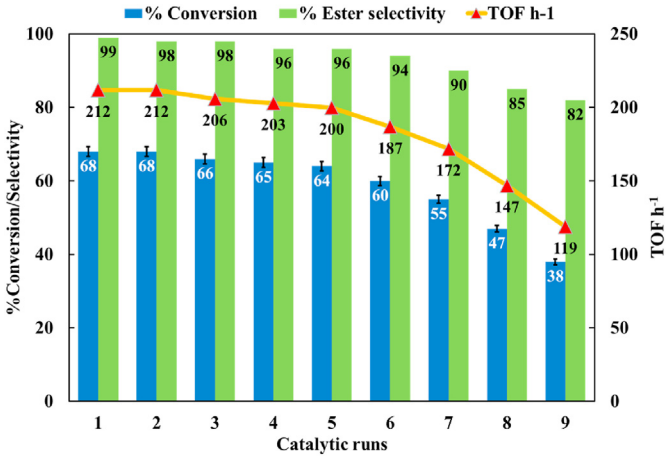

Fig. 11. Recycling experiments.

almost same conversion as well as ester selectivity (Fig. 11). However, after that a decline in the conversion as well as selectivity of ester was observed, indicating the reusability of catalyst up to six runs. However, one can also reuse the catalyst up to 9 cycles depending on chemist's choice. These duplicate results also confirm the sustainable character of catalyst and as there occurs no leaching of active species, the catalyst is considered truly heterogeneous.

3.5. Characterization of recycled catalyst

The stability and durability of the recycled catalyst were characterized by performing potentiometric titrations, FT-IR and BET surface area analysis. By potentiometric titration, the total acidic sites in recycled catalyst were found to be 4.9 mEqui g^{-1} which are almost equivalent to that of the fresh one (5.1 mEqui g^{-1}), confirming the intact acidic property after the reaction. From the EDX analysis, 0.23 wt % of P and 16.90 wt% W was observed for the reused catalyst which is in good agreement with that of the fresh catalyst (P = 0.24 wt%, W = 17.68 wt%). In the FT-IR spectra (Fig. 12a), retainment of all the bands in recycled catalyst suggests the unaltered structure as well as chemical integrity. The recycled catalyst shows similar N_2 adsorption-desorption isotherms, indicating the unaffected pore structure (Fig. 12b). A slight decrease in surface area of recycled catalyst (242.2 m^2/g) relative to the fresh one (258 m^2/g) can be justified as some of the reactant or solvent molecules may have been adsorbed or trapped after the treatment to catalyst. These observations also confirm that even after the catalytic cycle, the interaction between the support and PW_{12} does not weaken and proves the sustainable nature of the catalyst.

3.6. Scope of other alcohols and bioplatform acids

The study of different substrates holds enormous importance to developing an industrial process. Versatile performance for PW_{12}/MCM-22 was explored for esterification of levulinic acid with some alcohols and some of the bioplatform acids (Tables 6 and 7). Esters of levulinic acid with a variety of carbon chains (unbranched and branched) were synthesized and the results are presented in Table 6. Esterification with C3 to C8 chain alcohols gives their respective esters an excellent yield of almost >60%. It is observed from the literature that all the primary alcohols up to C4 chain length converts easily into their respective levulinate esters [10,41,42]. As the chain length increases or branching occurs, the rate of ester formation decreases due to the steric hindrance. At the same time, it is in interesting to note down that the conversion

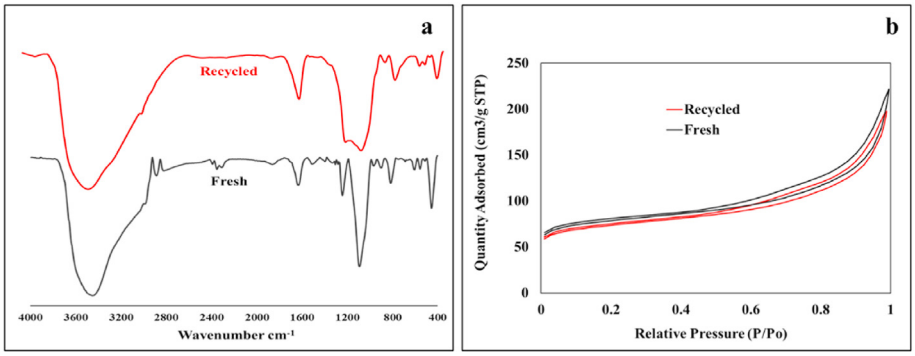

Fig. 12. (a) FT-IR spectra (b) N_2 adsorption-desorption isotherms (fresh and regenerated catalyst).

increase for C5–C7 alcohols even though the stearic hindrance, was present this may be due to the contribution from electronic factors which promote the stabilization of formed carbocation intermediates, responsible for the ester formation. Herein, PW_{12}/MCM-22 depicts remarkable catalytic activity for all the alcohols (primary and secondary) with chain length up to C8. Importantly, most of these levulinates esters owns outstanding fuel-blending properties and other commercial applications.

For all the acids except fumaric acid, the catalyst shows substantial conversion (61–91%) to their respective esters (Table 7). In the case of fumaric acid, the reason behind the lower rate of reaction can be attributed to the structural limitations due to the trans geometry [43]. All the esters obtained from these acids find ample industrial applications.

3.7. Comparison study with other reported catalysts and novelty of catalyst

Several catalytic systems have been developed for the most sustainable and modest pathway of synthesizing levulinate esters via acid catalysed esterification of levulinic acid. In this direction, for the present catalyst, the reaction conditions are compared selectively with the other PW_{12} based reported ones (Table 8). It is also highlighted that in the comparison study we have considered the catalytic systems having an equivalent mole ratio of the reactants as ours, as it is one of the significant and crucial parameters which governs the rate of reaction. Zhou et al. [29] described that the ammonium and silver co-doped phosphotungstic acid acts as an efficient catalyst for levulinic acid esterification, yielding 99 and 92% ester with TOF of 33 and 31 h^{-1}, respectively at 120 °C in 2 h (Entry 1 & 2). Pizzio et al. [32] carried out the synthesis of butyl levulinate using TPA/SiO_2 composite coatings over Fe_2O_4@SiO_2 and obtained 100% yield with TOF of 15 h^{-1} at 80 °C in 5 h (Entry 3). As compared to these systems, the present catalyst (PW_{12}/MCM-22) (Entry 4) exhibits superior catalytic activity (68% ester yield) in mild reaction conditions (90 °C, 8 h) with an outstanding TOF of 212 h^{-1}. However, compared to other systems the conversion (68%) in the present system is relatively lower which may be due to the usage of less amount of catalyst (0.04 mol %) and lower temperature. Further, it is also noteworthy that only 0.04 mol % of the catalyst is utilized, to carry out the successful synthesis of butyl levulinate, which is almost 35 times less than that of the amount of the reported catalysts. As for the industrial applications, TOF is an important factor, the present catalyst is far better than that of the reported ones. Thus, PW_{12}/MCM-22 proves to be highly efficient as a heterogeneous catalyst and provides a promising and sustainable catalytic system.

Table 6
Esterification of levulinic acid with different alcohols.

Sr. No	Alcohols	% Conv[a]/Sel[b]
1		75/100
3	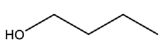	68/99
4	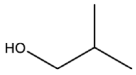	65/97
5	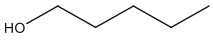	70/96
6	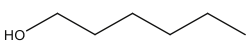	77/96
7	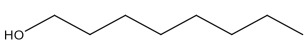	78/97

Conditions. mole ratio: 1:2; catalyst amount: 1.86 wt%; temp: 90 °C; time: 8 h.
[a] % Conversion of levulinic acid.
[b] % Selectivity of respective esters.

Table 7
Esterification of bio-derived acids with 1-butanol over PW_{12}/MCM-22.

Sr. No	Substrates (Acids)	% Conv[a]	% Sel[b]	
			Monoester	Diester
1	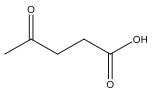	68	99	-
2	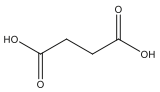	91	51	49
3	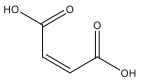	61	97	03
4	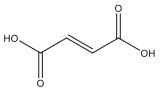	30	100	–

Conditions. mole ratio: 1:2; catalyst amount: 1.86 wt%; temp: 90 °C; time: 8 h.
[a] % Conversion of levulinic acid.
[b] % selectivity of respective esters.

3.8. Plausible mechanism for levulinate esterification

The plausible reaction mechanism for solid acid (Bronsted acid) catalysed levulinic acid esterification is shown in Fig. 13. The protons present in the Keggin structure of PW_{12} activate the carbonyl carbon of carboxylic acid group, forming an electrophilic

Table 8
Esterification of levulinic acid with 1-butanol over supported/modified PW_{12}.

Entry	Modified/Supported 12-tungstophosphoric acid	Mole ratio/Mol % of catalyst/Temp °C/Time h	% Ester yield	TOF	Ref
1	$((NH_4)_{0.5}Ag_{0.5}H_2PW)$ (1.5%)	1:2/1.5/120/2	99	33 h^{-1}	[29]
2	(Ag_1H_2PW) (1.5%)	1:2/1.5/120/2	92	31 h^{-1}	
3	$(Fe_3O_4@SiO_2@SiO_2/TPA_{400N2})$ (1.38 mol %)	1:2/1.38/80/5	100	15 h^{-1}	[32]
4	PW_{12}/MCM-22 (0.04 mol %)	1:2/0.04/90/8	68	212 h^{-1}	Present work

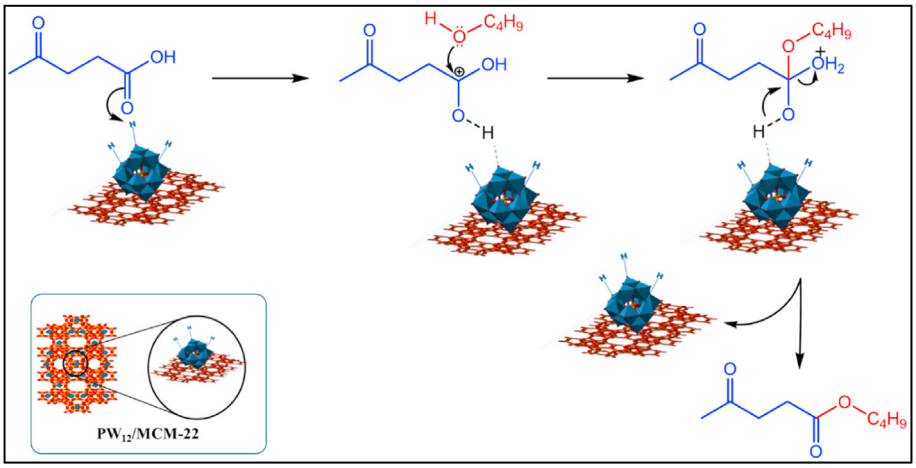

Fig. 13. Plausible mechanism for acid catalysed esterification of levulinic acid.

intermediate. Simultaneously, the hydroxyl group of alcohol attacks the electrophilic centre and forms an oxonium intermediate. This intermediate is stabilized by the negative charge generated on deprotonated PW_{12}. The intermediate then losses a proton back to the active site and by eliminating water, forms desired ester. In the overall process, the unique pore structure of MCM-22 has two roles to play. Firstly, it directs the reactant molecules to active catalytic sites by preventing the mass transfer limitations and secondly, it stabilizes the deprotonated keggin structure. Thus, the overall picture suggests that PW_{12}/MCM-22 generates a perfect synergy to carry out the esterification of levulinic acid.

4. Conclusion

To conclude, this paper presents a novel catalytic pathway for the production of transportation fuel components, butyl levulinate using a green and eco-friendly catalyst, PW_{12} anchored to MCM-22. The catalyst was successfully synthesized and characterized using various techniques. BET surface area analysis, SEM and TEM verify the effective filling of PW_{12} inside the zeolitic pores of MCM-22, whereas, the solid-state ^{29}Si MAS NMR confirms the interaction between them. Pyridine adsorbed FT-IR indicates the presence of both Bronsted and Lewis acid sites. The catalyst exhibits promising activity (68% conversion and 99% ester selectivity) for the synthesis of butyl levulinate under optimized conditions. The probable mechanism suggests that the higher acidic sites present in PW_{12} catalyse the esterification reaction while the support MCM-22 plays a significant role in obtaining the highest selectivity of the desired ester and also it limits the mass transfer problems. The recycling study depicts the true heterogeneous nature of the catalyst. The catalyst also proved to impart the best catalytic system as compared to that of the other similar reported catalysts while the substrate scope offers a versatile aura of the industrial applications for synthesizing the top fuel-blending esters. It represents a novel strategic and promising way of converting a model bioplatform intermediates to valuable products. Furthermore, considering the future aspects, this catalytic system may be employed for the conversion of direct biomass feedstock to fuel components which ultimately will turn the process cost-effective and benign.

Funding

This research did not receive any specific grant from funding agencies in the public, commercial, or not-for-profit sectors.

Data availability

Supplementary information is available.

CRediT authorship contribution statement

Dhruvi Pithadia: Methodology, Validation, Formal analysis, Investigation, Writing – original draft. **Anjali Patel:** Conceptualization, Validation, Writing – review & editing, Visualization, Supervision. **Vijay Hatiya:** Methodology, Investigation.

Declaration of competing interest

The authors declare that they have no known competing financial interests or personal relationships that could have appeared to influence the work reported in this paper.

Acknowledgements

We are thankful to the Department of Chemistry, The Maharaja Sayajirao University of Baroda for BET surface area analysis.

Appendix A. Supplementary data

Supplementary data to this article can be found online at https://doi.org/10.1016/j.renene.2022.01.106.

References

[1] J.C. Serrano-Ruiz, R. Luque, A. Sepúlveda-Escribano, Transformations of biomass-derived platform molecules: from high added-value chemicals to fuels via aqueous-phase processing, Chem. Soc. Rev. 40 (2011) 5266–5281, https://doi.org/10.1039/c1cs15131b.

[2] J.S. Luterbacher, D. Martin Alonso, J.A. Dumesic, Targeted chemical upgrading of lignocellulosic biomass to platform molecules, Green Chem. 16 (2014) 4816–4838, https://doi.org/10.1039/C4GC01160K.

[3] J. Han, S.M. Sen, D.M. Alonso, J.A. Dumesic, C.T. Maravelias, A strategy for the simultaneous catalytic conversion of hemicellulose and cellulose from lignocellulosic biomass to liquid transportation fuels, Green Chem. 16 (2014) 653–661, https://doi.org/10.1039/C3GC41511B.

[4] N. Ahmad, N. Ahmad, U. Ahmed, Process design and techno-economic evaluation for the production of platform chemical for hydrocarbon fuels from lignocellulosic biomass using biomass-derived γ-valerolactone, Renew. Energy 161 (2020) 750–755, https://doi.org/10.1016/j.renene.2020.07.028.

[5] V. Krishnan, J.D. McCalley, The role of bio-renewables in national energy and transportation systems portfolio planning for low carbon economy, Renew. Energy 91 (2016) 207–223, https://doi.org/10.1016/j.renene.2016.01.052.

[6] H. Jahangiri, J. Santos, A. Hornung, M. Ouadi, in: K.K. Pant, S.K. Gupta, E. Ahmad (Eds.), Thermochemical Conversion of Biomass and Upgrading of Bio-Products to Produce Fuels and Chemicals BT - Catalysis for Clean Energy and Environmental Sustainability: Biomass Conversion and Green Chemistry - Volume 1, Springer International Publishing, Cham, 2021, pp. 1–47, https://doi.org/10.1007/978-3-030-65017-9_1.

[7] J. Zhong, J. Pérez-Ramírez, N. Yan, Biomass valorisation over polyoxometalate-based catalysts, Green Chem. 23 (2021) 18–36, https://doi.org/10.1039/D0GC03190A.

[8] N.S. Bhat, S.S. Mal, S. Dutta, Recent advances in the preparation of levulinic esters from biomass-derived furanic and levulinic chemical platforms using heteropoly acid (HPA) catalysts, Mol. Catal. 505 (2021) 111484, https://doi.org/10.1016/j.mcat.2021.111484.

[9] A.F. Peixoto, M.M.A. Soliman, T. v Pinto, S.M. Silva, P. Costa, E.C.B.A. Alegria, C. Freire, Highly active organosulfonic aryl-silica nanoparticles as efficient catalysts for biomass derived biodiesel and fuel additives, Biomass Bioenergy 145 (2021) 105936, https://doi.org/10.1016/j.biombioe.2020.105936.

[10] K.C. Badgujar, V.C. Badgujar, B.M. Bhanage, A review on catalytic synthesis of energy rich fuel additive levulinate compounds from biomass derived levulinic acid, Fuel Process. Technol. 197 (2020) 106213, https://doi.org/10.1016/j.fuproc.2019.106213.

[11] F.G. Cirujano, A. Corma, F.X. Llabrés i Xamena, Conversion of levulinic acid into chemicals: synthesis of biomass derived levulinate esters over Zr-containing MOFs, Chem. Eng. Sci. 124 (2015) 52–60, https://doi.org/10.1016/j.ces.2014.09.047.

[12] A. Patel, D. Morawala, H. Lankapati, B. Shah, K. Maheria, Ti-ATMP catalyzed esterification of levulinic acid to synthesize butyl ester, Mater. Today Proc. (2021), https://doi.org/10.1016/j.matpr.2021.01.347.

[13] F. Yang, J. Tang, Catalytic upgrading of renewable levulinic acid to levulinate esters using perchloric acid decorated nanoporous silica gels, ChemistrySelect 4 (2019) 1403–1409, https://doi.org/10.1002/slct.201803608.

[14] N.A.S. Ramli, N.I. Hisham, N.A.S. Amin, Esterification of levulinic acid to levulinate esters in the presence of sulfated silica catalyst, Sains Malays. 47 (2018) 1131–1138, https://doi.org/10.17576/jsm-2018-4706-08.

[15] M.P. Pachamuthu, V. v Srinivasan, R. Karvembu, R. Luque, Preparation of mesoporous stannosilicates SnTUD-1 and catalytic activity in levulinic acid esterification, Microporous Mesoporous Mater. 287 (2019) 159–166, https://doi.org/10.1016/j.micromeso.2019.05.061.

[16] Z. Miao, Z. Li, J. Zhao, W. Si, J. Zhou, S. Zhuo, MoO3 supported on ordered mesoporous zirconium oxophosphate: an efficient and reusability solid acid catalyst for alkylation and esterification, Mol. Catal. 444 (2018) 10–21, https://doi.org/10.1016/j.mcat.2017.10.028.

[17] A. Najafi Chermahini, M. Nazeri, Esterification of the levulinic acid with n-butyl and isobutyl alcohols over aluminum-containing MCM-41, Fuel Process. Technol. 167 (2017) 442–450, https://doi.org/10.1016/j.fuproc.2017.07.034.

[18] L. Zhou, Y. He, L. Ma, Y. Jiang, Z. Huang, L. Yin, J. Gao, Conversion of levulinic acid into alkyl levulinates: using lipase immobilized on meso-molding three-dimensional macroporous organosilica as catalyst, Bioresour. Technol. 247 (2018) 568–575, https://doi.org/10.1016/j.biortech.2017.08.134.

[19] E. Altuntepe, V.N. Emel'yanenko, M. Forster-Rotgers, G. Sadowski, S.P. Verevkin, C. Held, Thermodynamics of enzyme-catalyzed esterifications: II. Levulinic acid esterification with short-chain alcohols, Appl. Microbiol. Biotechnol. 101 (2017) 7509–7521, https://doi.org/10.1007/s00253-017-8481-4.

[20] S. Zhou, D. Jiang, X. Liu, Y. Chen, D. Yin, Titanate nanotubes-bonded organosulfonic acid as solid acid catalyst for synthesis of butyl levulinate, RSC Adv. 8 (2018) 3657–3662, https://doi.org/10.1039/C7RA12994G.

[21] F.-F. Mao, W. Zhao, D.-J. Tao, X. Liu, Highly efficient conversion of renewable levulinic acid to n-butyl levulinate catalyzed by sulfonated magnetic titanium dioxide nanotubes, Catal. Lett. 150 (2020) 2709–2715, https://doi.org/10.1007/s10562-020-03177-0.

[22] J. Yang, G. Li, L. Zhang, S. Zhang, Efficient production of N-butyl levulinate fuel additive from levulinic acid using amorphous carbon enriched with oxygenated groups, Catalysts 8 (2018), https://doi.org/10.3390/catal8010014.

[23] A. v Nakhate, G.D. Yadav, Synthesis and characterization of sulfonated carbon-based graphene oxide monolith by solvothermal carbonization for esterification and unsymmetrical ether formation, ACS Sustain. Chem. Eng. 4 (2016) 1963–1973, https://doi.org/10.1021/acssuschemeng.5b01205.

[24] K.C. Maheria, J. Kozinski, A. Dalai, Esterification of levulinic acid to n-butyl levulinate over various acidic zeolites, Catal. Lett. 143 (2013) 1220–1225, https://doi.org/10.1007/s10562-013-1041-3.

[25] K.Y. Nandiwale, V. v Bokade, Esterification of renewable levulinic acid to n-butyl levulinate over modified H-ZSM-5, Chem. Eng. Technol. 38 (2015) 246–252, https://doi.org/10.1002/ceat.201400326.

[26] W. Zhao, H. Ding, J. Zhu, X. Liu, Q. Xu, D. Yin, Esterification of levulinic acid into n-butyl levulinate catalyzed by sulfonic acid-functionalized lignin-montmorillonite complex, J. Bioresour. Bioproduct 5 (2020) 291–299, https://doi.org/10.1016/j.jobab.2020.10.008.

[27] M.A. Tejero, E. Ramírez, C. Fité, J. Tejero, F. Cunill, Esterification of levulinic acid with butanol over ion exchange resins, Appl. Catal. Gen. 517 (2016) 56–66, https://doi.org/10.1016/j.apcata.2016.02.032.

[28] Y. Chen, X. Zhang, M. Dong, Y. Wu, G. Zheng, J. Huang, X. Guan, X. Zheng, MCM-41 immobilized 12-silicotungstic acid mesoporous materials: structural and catalytic properties for esterification of levulinic acid and oleic acid, J. Taiwan Inst. Chem. Eng. 61 (2016) 147–155, https://doi.org/10.1016/j.jtice.2015.12.005.

[29] X. Zhou, Z.X. Li, C. Zhang, X.P. Gao, Y.Z. Dai, G.Y. Wang, Efficient conversion of renewable levulinic acid to n-butyl levulinate catalyzed by ammonium and silver co-doped phosphotungstic acid, J. Mol. Catal. Chem. 417 (2016) 71–75, https://doi.org/10.1016/j.molcata.2016.03.006.

[30] K. Manikandan, K.K. Cheralathan, Heteropoly acid supported on silicalite−1 possesing intracrystalline nanovoids prepared using biomass – an efficient and recyclable catalyst for esterification of levulinic acid, Appl. Catal. Gen. 547 (2017) 237–247, https://doi.org/10.1016/j.apcata.2017.09.007.

[31] Q. Luan, L. Liu, S. Gong, J. Lu, X. Wang, D. Lv, Clean and efficient conversion of renewable levulinic acid to levulinate esters catalyzed by an organic-salt of H4SiW12O40, Process Saf. Environ. Protect. 117 (2018) 341–349, https://doi.org/10.1016/j.psep.2018.05.015.

[32] A.M. Escobar, M.N. Blanco, J.J. Martínez, J.A. Cubillos, G.P. Romanelli, L.R. Pizzio, Biomass derivative valorization using nano core-shell magnetic materials based on keggin-heteropolyacids: levulinic acid esterification kinetic study with N-butanol, J. Nanomater. (2019) 5710708, https://doi.org/10.1155/2019/5710708, 2019.

[33] P. Ferreira, I.M. Fonseca, A.M. Ramos, J. Vital, J.E. Castanheiro, Valorisation of glycerol by condensation with acetone over silica-included heteropolyacids, Appl. Catal. B Environ. 98 (2010) 94–99, https://doi.org/10.1016/j.apcatb.2010.05.018.

[34] M. Thommes, K. Kaneko, A. v Neimark, J.P. Olivier, F. Rodriguez-Reinoso, J. Rouquerol, K.S.W. Sing, Physisorption of gases, with special reference to the evaluation of surface area and pore size distribution (IUPAC Technical Report), Pure Appl. Chem. 87 (2015) 1051–1069, https://doi.org/10.1515/pac-2014-1117.

[35] V.A. Ostroumova, A.L. Maksimov, MWW-type zeolites: MCM-22, MCM-36, MCM-49, and MCM-56 (A review), Petrol. Chem. 59 (2019) 788–801, https://doi.org/10.1134/S0965544119080140.

[36] Y. Cheng, X.Y. Su, M. Lu, Preparation and characterization of MCM-22 zeolite by varying-temperature hydrothermal synthesis, Adv. Mater. Res. 197–198 (2011) 1587–1590. https://doi.org/10.4028/www.scientific.net/AMR.197-198.1587.

[37] D. Pithadia, V. Hegde, V.P. Brahmkhatri, A. Patel, New catalyst comprising Silicotungstic acid and MCM-22 for degradation of some organic dyes, Environ. Sci. Pollut. Control Ser. 28 (2021) 10633–10641, https://doi.org/10.1007/s11356-020-11340-8.

[38] E. Xing, Y. Shi, W. Xie, F. Zhang, X. Mu, X. Shu, Synthesis, characterization and application of MCM-22 zeolites via a conventional HMI route and temperature-controlled phase transfer hydrothermal synthesis, RSC Adv. 5 (2015) 8514–8522, https://doi.org/10.1039/C4RA11434E.

[39] A. Patel, S. Singh, Novel dilacunary phosphotungstate supported onto zirconia: synthesis, characterization and versatile catalytic activity, J. Taiwan Inst. Chem. Eng. 64 (2016) 306–313, https://doi.org/10.1016/j.jtice.2016.04.019.

[40] A. Patel, D. Pithadia, Low temperature synthesis of bio-fuel additives via valorisation of glycerol with benzaldehyde as well as furfural over a novel sustainable catalyst, 12-tungstosilicic acid anchored to ordered cubic nanoporous MCM-48, Appl. Catal. Gen. 602 (2020) 117729, https://doi.org/10.1016/j.apcata.2020.117729.

[41] S.S. Enumula, V.R.B. Gurram, R.R. Chada, D.R. Burri, S.R.R. Kamaraju, Clean synthesis of alkyl levulinates from levulinic acid over one pot synthesized WO3-SBA-16 catalyst, J. Mol. Catal. Chem. 426 (2017) 30–38, https://doi.org/10.1016/j.molcata.2016.10.032.

[42] K.Y. Nandiwale, V. v Bokade, Environmentally benign catalytic process for esterification of renewable levulinic acid to various alkyl levulinates biodiesel, Environ. Prog. Sustain. Energy 34 (2015) 795–801, https://doi.org/10.1002/ep.12042.

[43] T.-C. Huang, J. Wan, L.-H. Tsai, Kinetic studies on the esterification of acid and alcohol in the presence of dowex 50W and of sulfuric acid, J. Chin. Chem. Soc. 14 (1967) 72–86, https://doi.org/10.1002/jccs.196700010.